

Title	Au/ステップ状TiO ₂ (320)接合界面のSHGによる研究
Author(s)	Haque, Md. Ehasanul
Citation	
Issue Date	2018-03
Type	Thesis or Dissertation
Text version	ETD
URL	http://hdl.handle.net/10119/15334
Rights	
Description	Supervisor:水谷 五郎, マテリアルサイエンス研究科, 博士

Optical second harmonic generation of the Au/stepped TiO₂ (320) interface

MD. EHASANUL HAQUE

Japan Advanced Institute of Science and Technology

Doctoral Dissertation

**Optical second harmonic generation of the
Au/stepped TiO₂ (320) interface**

MD. EHASANUL HAQUE

Supervisor: Professor Dr. Goro Mizutani

**School of Materials science
Japan Advanced Institute of Science and Technology**

March 2018

Acknowledgement

In the name of Allah S.W.T., I would like to precise my acknowledgement to my respective supervisor, friends and family whom has been supporting me consistently and giving me inspiration during my research work in Japan.

First of all, I would like to express my most gratitude to my respected supervisor, Professor Dr. Goro Mizutani, for his constant support and valuable guidance inside and outside of my research. His encouragement and mental support always helps me to continue my research work smoothly. I am pleased and consider myself privileged to be a researcher of his research group and to get a chance to work with him. Without his efforts, this project would have never been finished.

I would like to give my gratitude to Assistant Professor of Mizutani lab, Dr. Khuat Thi Thu Hien for giving me consistent support for doing my research. Her encouragement and support helps me to conduct my research work properly and have learnt many theoretical phenomena. She taught me how to be a self-reliant and efficiently independent researcher. She always support me to complete my homework through valuable and knowledgeable discussion and suggested me to maintain a good routine for getting good output from the research. She inspired me a lot to do better in my research.

I also want to give my special thanks to Professor Harvey Nicholas Rutt from the School of Electronics and Computer Science, University of Southampton, U.K for teaching



Acknowledgement

me many basic lessons about nonlinear optics and share many important information about my research work that helps me to conduct my research work in a proper way. I would like to express my warm thanks to my minor research supervisor Professor Yuzuru Takamura for giving me enormous supports during my Ph.D. sub thesis project.

I want to thank my internal committee members, Professor Masahiko Tomitori, Professor Yuzuru Takamura and Associate Professor Yoshifumi Oshima from School of Materials Science, JAIST. I would like to give my special thanks to Professor Emeritus Dr. Masatoshi Tanaka, Yokohama National University as an external committee member.

I would like to extend my thanks to all the past and present group members of my lab during my Ph.D. life.

Finally, I would like to express my heartiest gratitude to my beloved wife Munaly Akter and my 11.5 months old cutest princess Manha Haque Eshal, for their love, patience and mental support during my hard PhD life in JAIST, Nomi, Ishikawa, Japan.

JAIST, March 2018

Md. Ehasanul Haque



Abstract

In the catalytic field, the Au/TiO₂ plays an important role due to an extraordinary high activity for low-temperature catalytic combustion, partial oxidation of hydrocarbons, hydrogenation of unsaturated hydrocarbons, and reduction of nitrogen oxides and so on. Studying the electronic states of the Au/TiO₂ interface is vital to explore the catalytic mechanism. Many researchers already studied the electronic structure of the Au/TiO₂ (110) interface by several microscopic or optical technique such as scanning tunnelling microscope (STM), transmission electron microscope (TEM), UV-Vis spectroscopy, and so on . However, the observation of the electronic states of the Au/TiO₂ interface and stepped and flat TiO₂ surface by second harmonic generation (SHG) method is very limited. For this reason, I intended to observe the electronic states of the Au/stepped TiO₂ interface using SHG method. SHG is a well-established surface-specific probe of centrosymmetric media. In the dipole approximation, SHG is forbidden in the bulk of a medium having inversion symmetry, while it is allowed at the surface where inversion symmetry is broken. Because of the symmetry selection property, the SHG method can be one of the ideal methods to measure the contribution of the step structure, while other surface tools such as XPS, TEM, STM, UV-Vis spectroscopy and microscopy technique cannot do because the number of steps are normally lower than the terrace atoms. In this research, stepped bare TiO₂ (320) single crystal surface was used as a substrate and Au thin film with the thickness of 2 nm was deposited on the surface in a UHV chamber at a pressure of 2×10^{-7} Torr. This Au/TiO₂ (320) interface may act as an active sites for showing the catalytic behaviour. As it is well known, surface defects such as steps and kinks play an important role in generating active sites for catalytic reactions, so it is vital to study the structure and the electronic states of such surface defects. Thus, it would be very informative to analyse the SHG response from the interface of TiO₂ stepped



surface decorated by Au. Au/TiO₂ steps should generate an SHG signal due to broken symmetry at the interface.

The SHG response from the Au/TiO₂ (320) interface and bare TiO₂ (320) surface was investigated with the incident photon energies of 1.17 eV and 2.33 eV generated by using a pulsed Nd³⁺:YAG laser. The isotropic response was found from both samples at the incident photon energy of 1.17 eV. In contrast, we observed the anisotropic response from both Au /TiO₂ (320) and bare TiO₂ (320) at the incident photon energy of 2.33 eV. From the Au/TiO₂ (320) sample, an anisotropic structure was observed to the $[\bar{2}30]$ direction for Pin/Pout polarization combination. Here, the Pin denotes the input polarization mode of the incident light and Pout corresponds to the output polarization mode of the SHG light. From the experimental data, I theoretically decomposed the nonlinear susceptibility elements ($\chi_{ijk}^{(2)}$). Here, i, j and k denote the axis direction of the sample coordinate. I found that there were two groups of the nonlinear susceptibility elements corresponding to step and terrace contribution. More precisely, I have calculated SHG intensity patterns for Au/TiO₂ (320) and bare TiO₂ (320) based on the terrace and step contributions fitted to the experimental results with photon excitation energies of 2.33 eV. The anisotropic responses were observed due to the contributions of both the step and terrace groups of nonlinear susceptibility elements. From the calculated results of the step and terrace groups of $\chi_{ijk}^{(2)}$ elements, it was found that the step contribution of the Au/TiO₂ (320) is different from that of the bare TiO₂ (320) sample for the Pin/Pout polarization combination. In order to discuss the possible reasons for this difference, I considered the four possible mechanism candidates as an origin of the signal enhancement from the Au/TiO₂ (320) interface. This four candidates are (a) Enhancement of the incident electric field by surface defects (b) Electronic resonance of Au/TiO₂ interface step (c) Surface plasmon effect on SHG enhancement (d) Fresnel factor effect on SHG

enhancement.

I found that Au deposited TiO₂ (320) surface contains island structure by the observation of AFM and SEM with EDX and these islands might act as “hot spot” and make the SHG intensity stronger. However, this effect should have an isotropic nature with respect to the rotation of the sample around its normal because these islands are randomly distributed. The effect would be similar if I consider the enhancement occurring due to the random steps on the surface. This is not the case when I see the SHG pattern for Pin/Pout polarization combination. So, this candidate should be eliminated.

An electronic resonance may occur at the step region of the Au/TiO₂ interface and it is the most possible candidate for the enhancement of the SHG signal considering this case. In this study I observed the enhanced SHG signal correlated with the existence of the Au/TiO₂ (320) interface steps. Hence this interface step electronic state is a credible candidate of the origin of the enhanced signal.

In the case of a thin gold film deposited on pre-patterned TiO₂ substrate, local field enhancement may result from the surface plasmon resonance (SPR). I measured the linear optical reflectivity in order to confirm whether there is any influence of surface plasmon resonance and Fresnel factor for the enhancement of the anisotropic SHG signal obtained from the Au/TiO₂ (320) interface. From the reflectivity data of the Au/TiO₂ (320) interface, it was observed that, the reflectivity for P- and S- polarized light are almost the same at the azimuthal angle, $\varphi = 0^\circ$ and 180° . This result indicates that the linear optical process at frequency ω occurs almost in the same way at $\varphi = 0^\circ$ and 180° and it means that even if the SPR occurred, there is no effect on the enhanced SHG signal due to the different response from the $\varphi = 0^\circ$ and 180° . This discussion is also true for the Fresnel factors.



Therefore, there is no influence of Fresnel factors on the enhancement of SHG signal.

From the above discussion of four candidates, it seems that electronic resonance at the Au/TiO₂ (320) interface step is feasibly responsible for the enhancement of the SHG. The other three mechanism candidates can be eliminated due to their less feasibility.

Keywords: Second harmonic generation (SHG); Catalyst; Au/TiO₂ (320) interface; Electronic states; Anisotropy; Nonlinear susceptibility elements; Step contribution.

Acknowledgement	I-II
Abstract	III-VI
Table of contents	VII-IX
Dedication	X
Chapter 1: Introduction and Research Motivation	1-27
1.1 Background	2-5
1.1.1 Literature of catalytic activities of Au/TiO ₂ interface.....	6-12
1.1.2 Literature on SHG response from Au/TiO ₂ interface and flat or stepped TiO ₂ surface.....	13-22
1.2 Objectives of research	23
1.3 Outline of the thesis	23-24
References	25-27
Chapter 2: Theoretical Background	28-62
2.1 Maxwell's equations	29-30
2.2 Nonlinear Optics	31
2.2.1 Theoretical background of nonlinear optics	31-34
2.2.2 Nonlinear polarization induced in noncentrosymmetric media.....	35-37
2.3 Second harmonic generation (SHG)	37-47
2.4 Nonlinear susceptibility: classical anharmonic oscillator model	47-52

2.5 Basic theory of scanning electron microscope (SEM)	52-55
2.6 Basic theory of atomic force microscope (AFM)	55-57
2.7 Basic theory of surface plasmon resonance (SPR)	58-60
References	61-62
Chapter 3: Experimental Procedure	63-77
3.1 Sample Preparation	64
3.1.1 Sample Cleaning by HF etching	64
3.1.2 Annealing of TiO ₂ (320) substrate	65-67
3.1.3 Au deposition on TiO ₂ (320) substrate in a UHV chamber	67-71
3.2 Optical Setup	72
3.2.1 Linear optical experimental setup	72-73
3.2.2 Nonlinear optical system for azimuthal angle dependent SHG experiment.....	73-74
3.2.3 Advantage of SHG spectroscopic measurement	75-76
References.....	77
Chapter 4: Results and Discussion	78-109
4.1 Morphological study of Au/TiO ₂ (320) interface by AFM and SEM with EDX...	79-85
4.2 SHG intensity measurement as a function of azimuthal and polarization	86
4.2.1 Experimental results	86-91
4.2.2 Theoretical investigation of the origin of rotational anisotropic response	92-107

4.2 Summary of this chapter.....108

References.....109

Chapter 5: General Conclusion110-113

Appendix (I) 114-116

Appendix (II).....117-133

Appendix (III).....134-140

Appendix (IV).....141-145

Appendix (V).....146-150

Appendix (VI).....151-153

*This Research Work is
Dedicated to
My Beloved parents,
Wife and
One-Year-Old Cutest Daughter*

Chapter 1: Introduction and Research Motivation

1.1 Background

1.1.1 Literature of catalytic activities of Au/TiO₂ interface

1.1.2 Literature on SHG response from Au/TiO₂ interface and flat or stepped TiO₂ surface

1.2 Objectives of this research

1.3 Outline of the thesis

References

Introduction and research motivation

1.1 Background

Akira Fujishima first discovered that the titanium dioxide has photocatalytic properties in 1967 and its surface exhibits tremendous photocatalytic activity is known as Honda-Fujishima effect [1]. Titanium dioxide can show the catalytic behavior both in thin film and in nanoparticle form [8]. There are mainly three crystal forms of TiO_2 : rutile, anatase, and brookite. They are polymorph of each other. That means these three forms can be changed to each other at particular temperature although it depends on the morphology and amount of impurity present in the structure [2]. The anatase can be transformed in to rutile at 550-1000°C and brookite can be transformed into rutile form at about 500-600°C [2,3]. The most common form of TiO_2 is rutile. It is also very stable and chemically inert. The UV and visible light can excite rutile [4,5]. However, anatase can excite only by UV light and has ability to transform to rutile form at high temperature. Under the excitation of light both rutile and anatase can act as a photocatalyst through generating the radical species and thus activated the surface [6]. Both of them have crystal structure of tetragonal ditetragonal dipyramidal although the space group lattice is different, whereas brookite has orthorhombic crystal structure and is not excited by UV light irradiation [4,7]. However, it can be converted into rutile or anatase form by heating. The crystal structure and the crystal form are shown by the following Figs. 1.1.1 and 1.1.2.

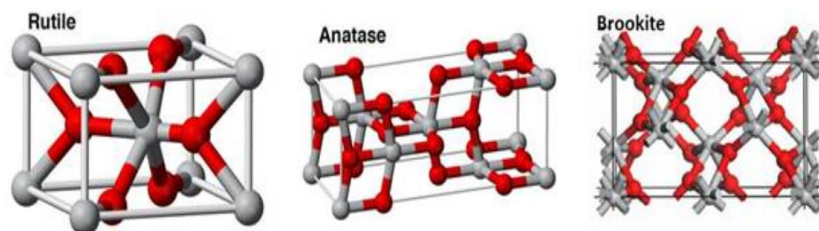


Figure. 1.1.1. Crystal Structure of rutile, anatase, and brookite titanium dioxide [4,7].

In these above structures, the grey and red balls correspond to the titanium atoms and oxygen atoms, respectively.



Figure. 1.1.2. Crystal images of rutile, anatase, and brookite titanium dioxide [8].

The rutile type TiO_2 has been used successfully as a potential catalyst to hydrolyze the water molecule into hydrogen and oxygen for the first time in 1970 [5].

The gold is also one of the widely used catalyst although at first it seemed that gold does not have any catalytic activities due to its chemical inertness [9]. It works as a catalyst for oxidative dehydrogenation, isomerization of hydrocarbons and so on [9]. When gold forms alloy with other metals such as palladium and platinum, it also exhibits good catalytic activities. The alloy between gold and other metals acts as a catalyst for the selective oxidation process [9]. Now-a-days the gold nanoparticles are extensively used as a catalyst either in the form of colloids or as a form of junction with supported metal oxides. Indeed, the surface area and the catalytic activity can be greatly enhanced as the size of the gold nanoparticle decreases as shown in Fig. 1.1.3 [10].

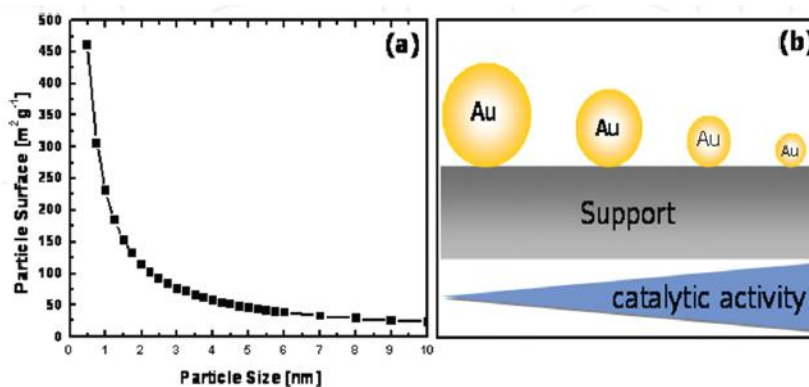


Figure. 1.1.3. Relation between the size of gold nanoparticles with the (a) surface area of Au nanoparticles and (b) catalytic activity [10].

The performance of bimetallic catalyst depends on many factors for different reactions. The factors that can have significant influence on catalytic behavior is represented by the following Fig. 1.1.4.

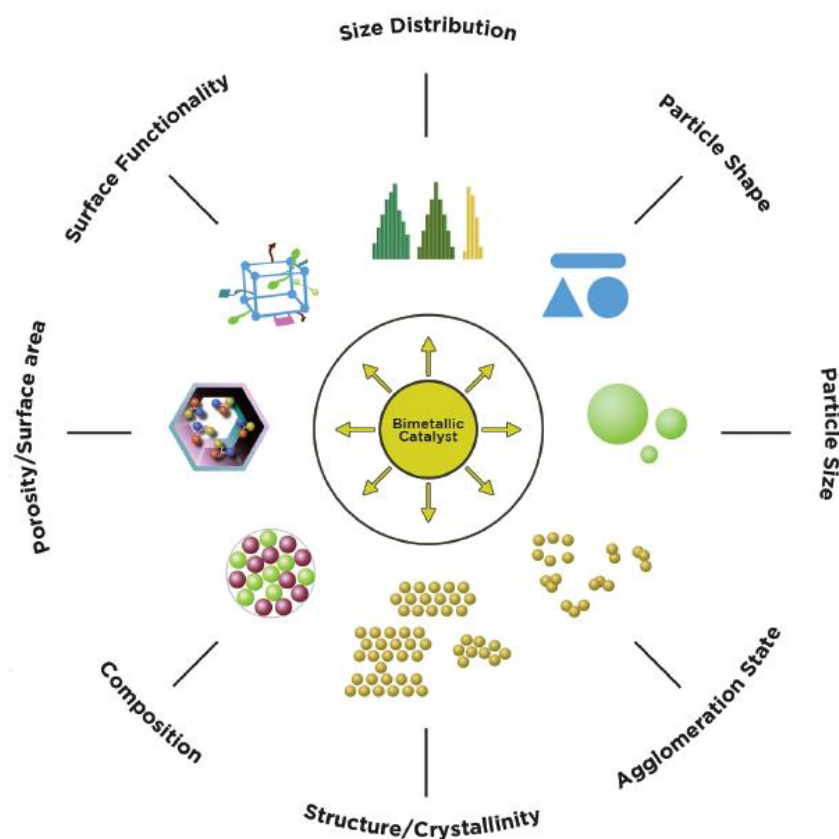


Figure. 1.1.4. The influencing factors on the catalytic activity of bimetallic catalyst in different reactions.

The metal oxide support is one of the important factor for the catalytic performances. The catalytic activity of AuNPs depends on the supported metal oxide. Miedziak et al. observed that the variation catalytic performances of AuNPs for the oxidation of benzyl alcohol to benzaldehyde depends on different metal oxide supports [11]. They yielded that among the five types of metal supports, the TiO_2 supported AuNPs showed the best catalytic performance compared to the others as shown in Fig. 1.1.5. Here, “X” indicates the conversion from benzyle alcohol to benzaldehyde, “Y” denotes the actual yield of the

benzaldehyde as the desired product from the reaction and “S” indicates the selectivity of the host chemical that may help to achieve desired amount of main product after the chemical reaction occurred.

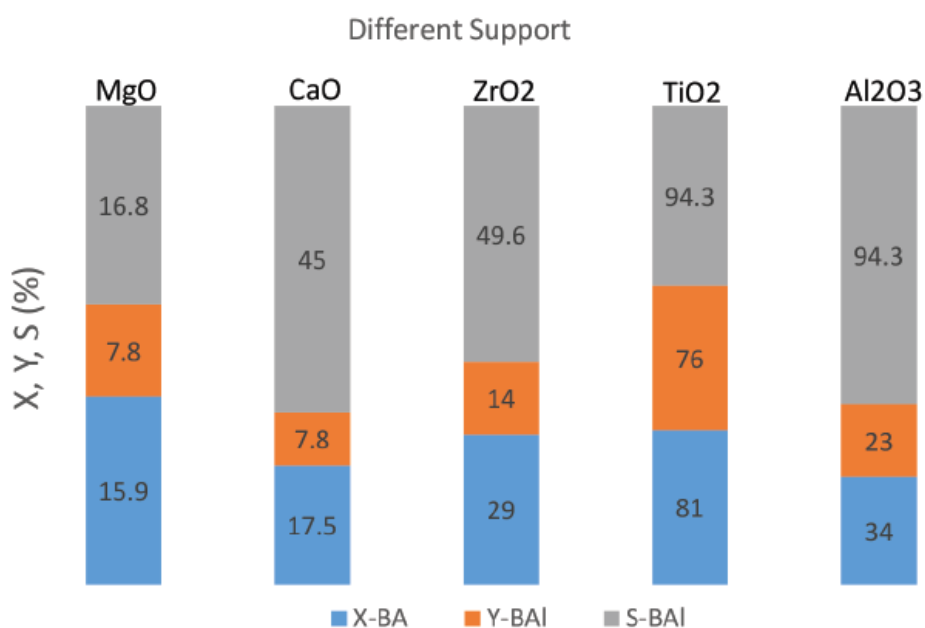


Figure 1.1.5. Influence of support on oxidation of benzyl alcohol to benzaldehyde over 1% Au/M catalysts (M = MgO, CaO, ZrO₂, TiO₂, Al₂O₃). Reaction conditions: 30 mL BA, 0.15 g catalyst, 140°C, 5 bar O₂, 4 h (X = conversion; Y = yield; S = selectivity).

Not only for this above mentioned chemical reaction but also for many chemical reactions TiO₂ supported Au film or nanoparticles exhibit tremendous catalytic performance. For This reason, I was interested in studying the electronic states of the Au/TiO₂ interface to understand the mechanism of the catalytic behavior.

1.1.1. Literature of catalytic activities of Au/TiO₂ interface

The Au/TiO₂ interface is a well-known catalyst for many chemical reactions, especially for the oxidation of CO gas at room temperature [12-14]. Gold and titanium dioxide can exhibit catalytic activity when they exist separately. However, the combination of Au and the TiO₂ substrate can work as a tremendous catalyst especially for the oxidation of carbon monoxide [14]. Z. Duan *et al.* studied the electronic structure of Au/TiO₂ interface and activation of oxygen atom on the interface through the adsorption and dissociation of oxygen molecule on the interface. This activated oxygen atom plays a vital role for the oxidation of carbon monoxide on the activated interface [13]. The activation sites of oxygen atom on the Au/TiO₂ interface for the oxidation reaction of carbon monoxide to carbon dioxide is shown by the following Fig. 1.1.1.1 [13].

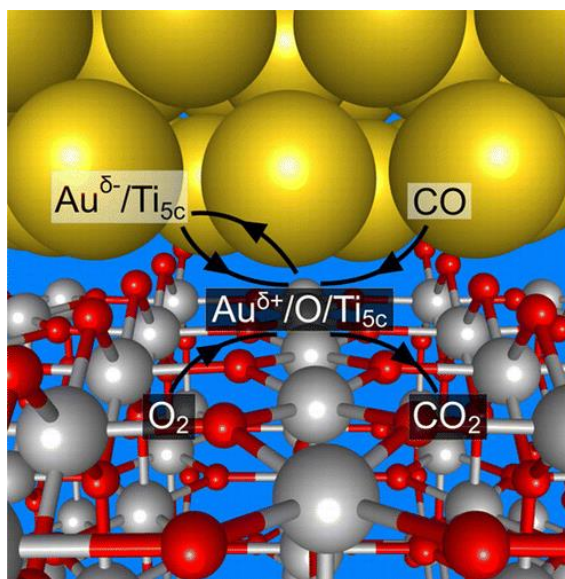


Figure. 1.1.1.1. Activation sites of oxygen atom on the Au/TiO₂ interface for the oxidation of CO [13].

The catalytic activity of Au/TiO₂ interface for the oxidation of CO has been observed in terms of particle size of Au [14,15]. M. Valden *et al.* found that the catalytic performance depends on the size of Au nanoparticle. Around 3.5 nm Au nanoparticle shows

the best catalytic activity for the oxidation of carbon monoxide to carbon dioxide when they are supported by the TiO₂ substrate [15]. Here, turn over frequency (TOF) can be expressed as the reaction rate ((Product molecules) × (surface sites)⁻¹ × s⁻¹) for the conversion of CO to CO₂ [15]. Fig. 1.1.1.2 represents the catalytic activity for the oxidation of CO to CO₂ as a function of average Au cluster diameter.

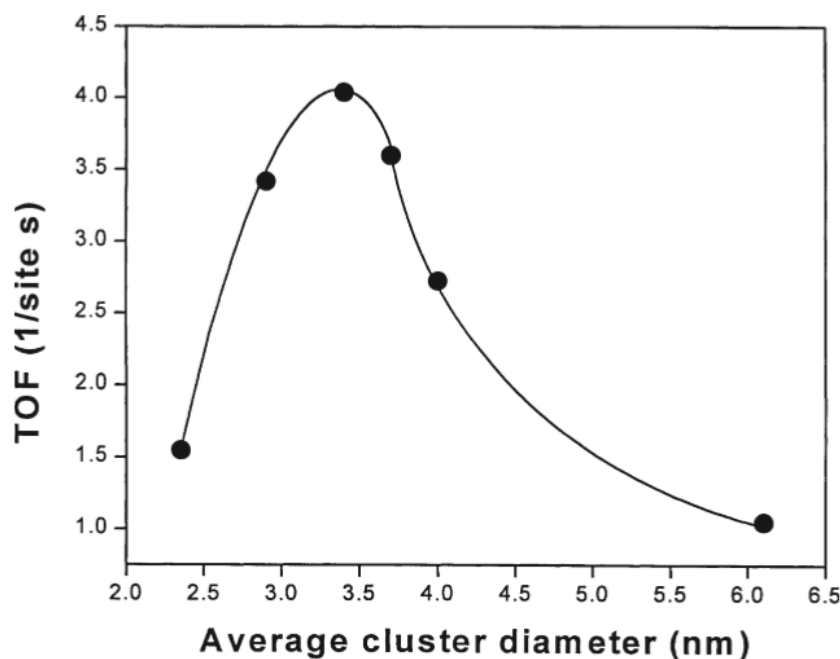


Figure 1.1.1.2. Catalytic activity for the oxidation of CO to CO₂ as a function of average Au cluster diameter.

Haruta *et al.* found that, when Au/TiO₂ has large peripheral part of a joining interface, it shows high catalytic activity [16]. Tsubota *et al.* studied the catalytic activity of mechanically mixed Au colloids and TiO₂ powder for the oxidation of CO and it shows poor catalytic activity. A tight junction interface was formed between Au colloids and TiO₂ powder by calcination at temperature of 673 K and dramatically enhanced the catalytic performance [17]. This result indicates that the effect of the peripheral part of a joining interface exhibit better catalytic activity. X. Z. Li *et al.* investigated the performance of photocatalytic activity of Au or Au³⁺ doped TiO₂ powder photocatalysts for the

photooxidation of methyl blue. They observed the photooxidation efficiency of photocatalyst for photodegradation of methyl blue by a number of spectroscopic method through irradiation of visible light [18]. Their results demonstrated that the photooxidation efficiency of methyl blue using Au/Au³⁺ doped TiO₂ powder is much higher than that of conventionally used TiO₂ powder [18]. These new types of photocatalyst have the ability to hinder the electron-hole recombination and extend the absorption spectrum to the visible region and also can enlarge the surface area for the photocatalytic activities [18]. I. M. Arabatzis *et al.* observed the photocatalytic activity of Au/TiO₂ composite film for azo-dye methyl orange photodegradation [19]. They improved the photocatalytic activity by the surface deposition of Au particles on TiO₂ through the observation of gold valence state, structure and morphological change at the interface of Au and TiO₂ by irradiating the UV light [19]. These modified photocatalyst have higher efficiency over conventional TiO₂ catalyst for the photodegradation of methyl orange type azo-dye materials [19]. A. S. Castillo *et al.* observed the photocatalytic activity for the degradation of organic pollutant of anisotropic plasmonic nanoparticles containing hot spots in Au/TiO₂ nanostructures [20]. They observed the influence of different Au anisotropic architecture on the performance of catalytic activity due to their different plasmonic excitation by the application of electromagnetic field. Among the three architecture of AuNPs, AuNSTs containing nanocomposite exhibits highest catalytic performance due the creation of intense local field at the spikes of this nanostructures [20]. These local fields create hot spot for the plasmon resonance due to the enhancement of incident electric field and can show tremendous catalytic activity for the organic pollutant degradation [20]. However, the role of Au/TiO₂ interface as a catalyst for many chemical reactions and the corresponding electronic phenomena taking place at the active sites are not yet clear enough [21].

Indeed, the catalytic activity should depend on the surface morphology such as oxygen vacancies, step structure and crystal imperfections and electronic states of the Au/TiO₂ interface [22]. So far, many researchers studied the electronic states of the Au/TiO₂ interface by using various techniques to explore the mechanism of the catalytic properties. X. Lai *et al.* studied the electronic structure of Au/TiO₂ interface as a function of different Au particle size by STM method. They found that the bandgap of the Au/TiO₂ (110) interface is related to the particle size of Au and the catalytic activity for the oxidation of CO is also closely related to the particle size [23]. Fig. 1.1.1.3 shows that the bandgap is nonzero at lower cluster diameter. When the Au cluster diameter is larger than 4 nm, then the electronic structure is fully metallic due to the lack of bandgap. However, it becomes non-metallic while the cluster diameter is less than 2 nm and the band gap become $\geq 1V$. Therefore, the bandgap is closely related to the Au cluster diameter as well as the electronic states of the Au/TiO₂ (110) interface [23].

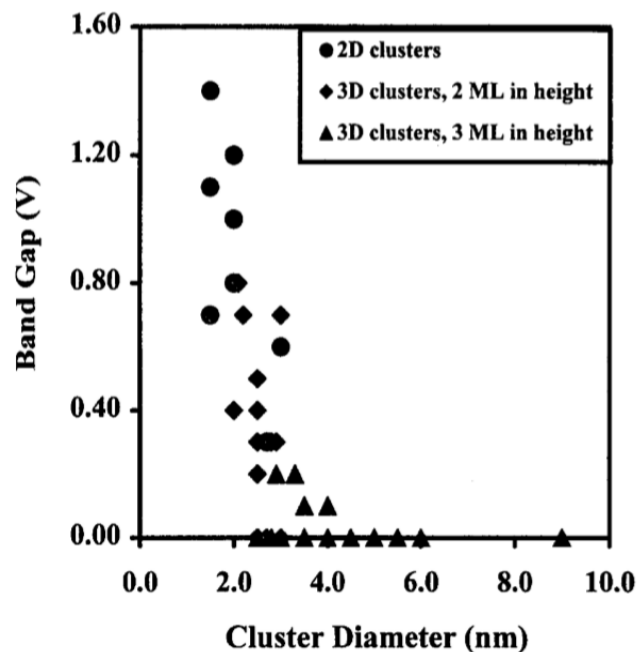


Figure 1.1.1.3. Relation between the cluster diameter and bandgap of Au/TiO₂ (110) interface.

Tanaka *et al.* observed local distribution of interstitial titanium ions in Au/TiO₂ by using aberration corrected transmission electron microscope. They showed the perspective view from the [110] direction of the bulk TiO₂ (110) structure and defined the *IV*-site shown in Fig. 1.1.1.4. Here, Ti-only columns contain only Ti-ions, Ti and O are arranged alternately in the Ti-O columns and in case of O-O columns, oxygen ions form a zigzag chain. The defined *IV*-site is in the center of the oxygen octahedrons where there is a probability to occupy the interstitial Ti ion [24].

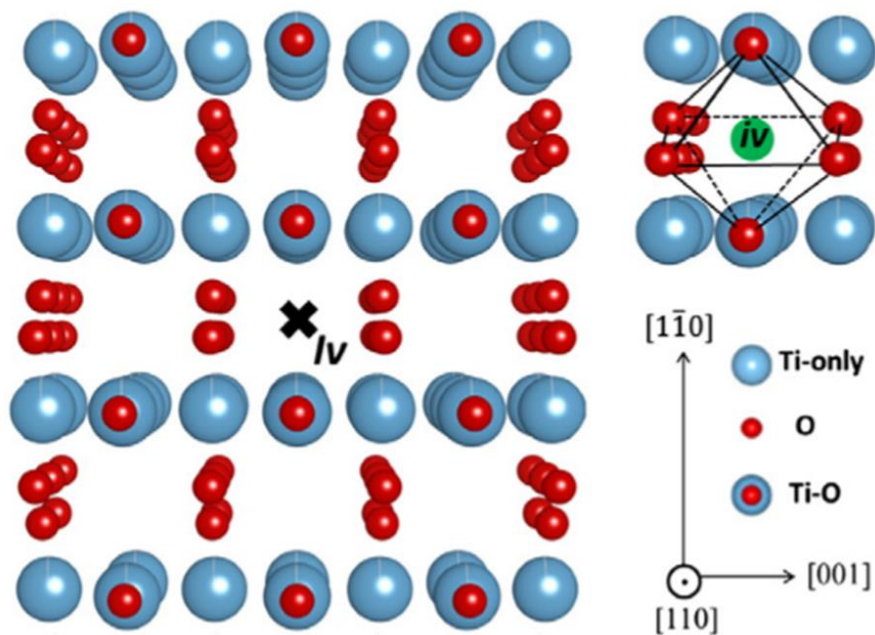


Figure 1.1.1.4. Perspective view of bulk TiO₂ from the [110] direction. Blue and red spheres illustrate Ti and O ions, respectively. Three kinds of atomic columns, viz. “Ti-only”, “Ti-O”, and “O-O” form the bulk TiO₂ unit cell. Cross (X) indicates the location of *IV*-column. Location of “*IV*-site” (green) at the center of the oxygen octahedron [24].

They observed the TEM images in Fig. 1.1.1.5 (a) and (b) taken at defocus of +5.5 nm and -5.5 nm, respectively, corresponding to the Fig. 1.1.1.4. All the atomic columns including Ti-only, Ti-O and O-O were bright at the defocus of +5.5 nm but at the defocus of

-5.5 nm, they are dark. Fig. 1.1.1.5 (c) and (d) are the simulated image of TiO_2 at defocus of +5.5 nm and -5.5 nm, respectively. According to the model structure, there were no interstitial Ti-ions at the defined *IV*-site which in the center of the oxygen octahedrons. So this simulated result agreed with the experimental TEM image result. They concluded that if there is any interstitial Ti-ion, the *IV*-site should be brighter enough in the TEM image.

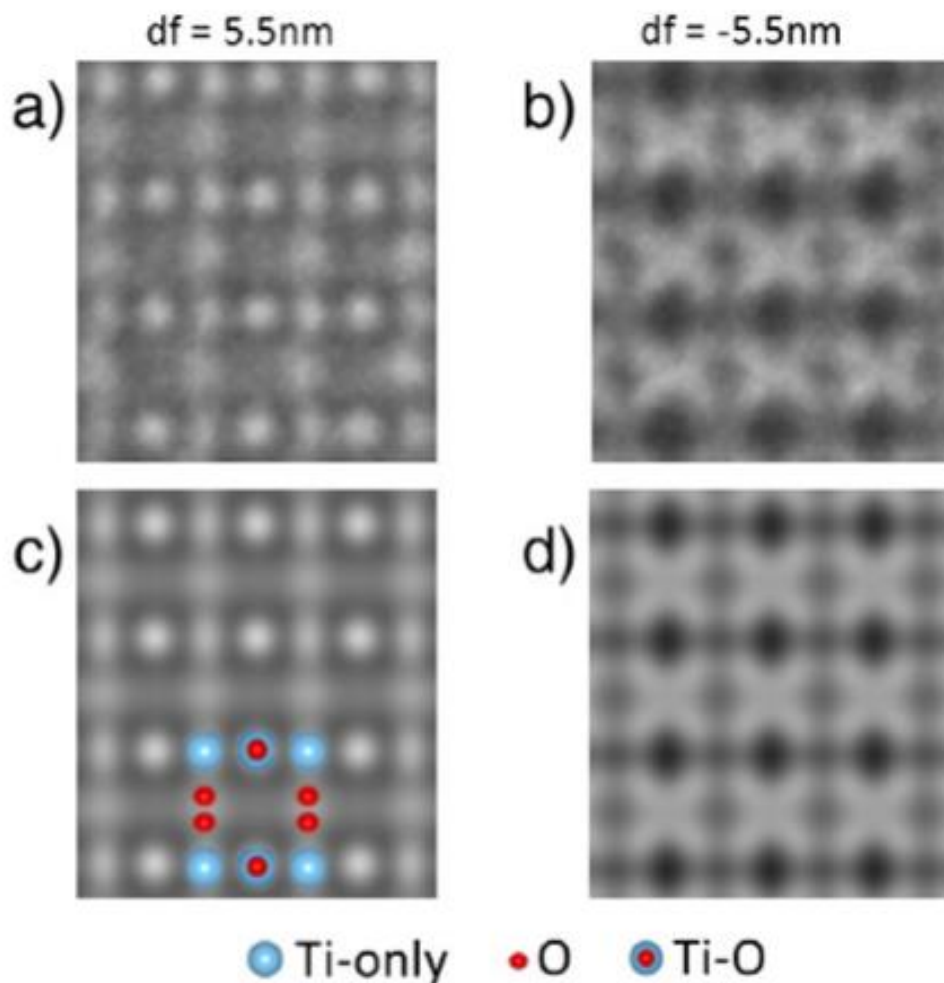


Figure 1.1.1.5. (a)–(b) Observed TEM images of defect-free TiO_2 viewed along the [110] direction: Defocus is (a) +5.5 nm (over focus) and (b) -5.5 nm (under focus). (c)–(d) Simulated TEM images of TiO_2 : Defocus is (c) +5.5 nm and (d) -5.5 nm. Specimen thickness is 3.9 nm. TiO_2 specimen and simulated model has no interstitial Ti ions at *IV*-site [24].

They suggested that the interstitial Ti ion is deficient in the peripheral region of Au nanoparticle whereas they existed at the perimeter/interface of Au/TiO₂ [24]. The following schematic diagram shows the local distribution of interstitial Ti ions in TiO₂ substrate and Au/TiO₂ perimeter/interface [24].

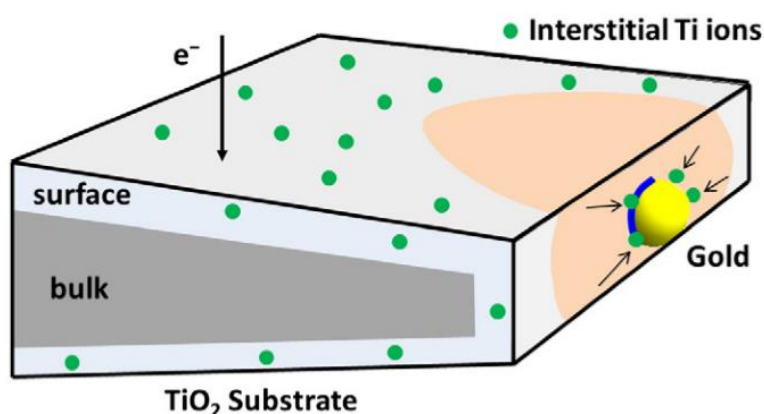


Figure 1.1.1.6. Schematic model representing a local distribution of interstitial Ti ions in TiO₂ substrate and Au/TiO₂ perimeter/interface after TEM observation. Green dot denotes the interstitial Ti ions. Light blue region illustrates a TiO₂ surface layer. Interstitial Ti ions are deficient in a peripheral region (orange area) of the Au particle, and localized at the Au/TiO₂ perimeter/interface. Blue curve indicates the perimeter of the Au/TiO₂ interface [24].

Yao *et al.* measured the broad absorption peak at the visible region from the particle size-dependent Au/TiO₂ catalyst by using UV-vis reflectance spectra. They concluded that the observed peak was due to the localized surface plasmon resonance of Au nanoparticle [14]. Strong absorption peak was observed due to the excitation of plasmon of Au nanoparticle from the Au/TiO₂ interface reported by other researchers [25-28]. These studies are related to the catalytic activity of Au/TiO₂ interface as a function of nanoparticle size distribution. Therefore, the Au/TiO₂ (320) interface act as a well-established catalyst for many chemical reactions. So, it emphasized to study the electronic states of this catalyst to understand mechanism of the catalytic behaviour.

1.1.2 Literature on SHG response from Au/TiO₂ interface and flat or stepped TiO₂ surface

The precise measurement of atomic scale electronic state from Au/TiO₂ interface using specific surface and interface probe such as second harmonic generation (SHG) is desirable to understand the catalytic mechanism properly. SHG is one of the prominent candidate to detect this signal due to its high surface and interface sensitivity. SHG is forbidden in the bulk of medium with inversion symmetry within the electric dipole approximation [29]. It has submonolayer sensitivity to the surface and interface of centrosymmetric media because it is only allowed in a broken symmetric structure [29]. Another attractive feature of SHG is that it is non-invasive and contactless and it can be applied to “in situ” and in “real-time” experiments with a good time resolution [30]. We can deduce information such as electronic structure and molecular orientation from the precise determination of the nonlinear susceptibility tensor [31]. We can extract the electronic level information from the interface of Au/TiO₂.

However, the number of studies of the electronic states from the stepped Au/TiO₂ interface by SHG is very limited. Only a single report was found regarding the observation of the SHG signal from Au/TiO₂ interface. Quelin *et al.* measured SHG intensity as a function of incident angle and input/output polarization from the thin Au/TiO₂ cermet films. Cermet films are the combination of the ceramic and metallic materials. The Au particles are randomly distributed in the TiO₂ matrix to form a cermet film. They detected enhanced SHG signal due to the local field enhancement by the surface plasmon excitation on gold clusters [32]. In fact, they studied the electromagnetic mode on Au clusters embedded in TiO₂ and were not interested in atomic scale electronic states at the interface between the two materials

[32]. More specifically Fig. 1.1.2.1 shows the SHG intensity vs polarization angle of 2ω beam plot. They observed the highest SHG intensity for the polarization angle of SHG beam $\theta = 0^\circ$ and the intensity is reduced for $\theta = +45^\circ$ and -45° but it approaches to zero at $\theta = 90^\circ$ [32]. However, they did not analyse the susceptibility tensor to clarify the electronic states between the Au particles and TiO_2 matrix interface.

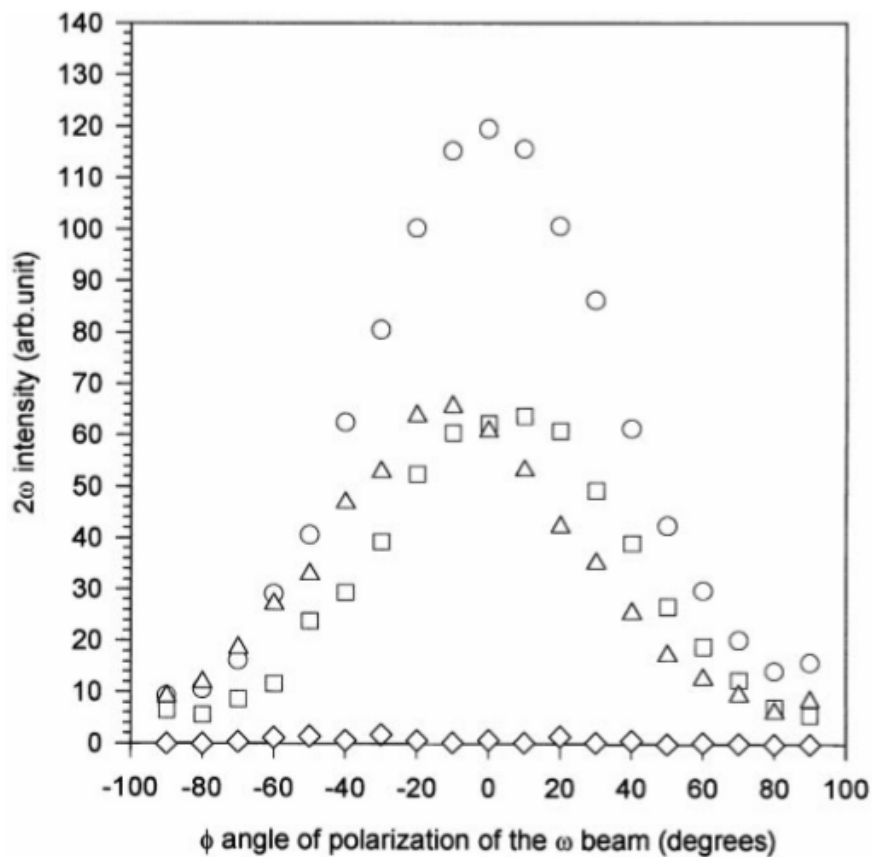


Fig. 1.1.2.1. Dependence of the SH intensity for 37% volume fraction of gold sample versus ω beam polarization (ϕ) for four values of the 2ω beam polarization: \circ for $\theta = 0^\circ$, \square for $\theta = -45^\circ$, \triangle for $\theta = +45^\circ$, \diamond for $\theta = 90^\circ$.

For this reason, I intended to observe the atomic level electronic states of the stepped Au/ TiO_2 interface using SHG method. This research work was one of the great motivation for me to analyse the independent non-vanishing nonlinear susceptibility tensor

precisely in order to understand the atomic level electronic state of the stepped Au/TiO₂ interface properly.

In fact, many researchers observed the SHG response from the flat and stepped bare TiO₂ surface to understand the electronic states of the surface. Kobayashi *et al.* observed SHG response from TiO₂ (110) as a function of the polarization and azimuthal angle. They determined surface $\chi_{sijk}^{(2)}$ elements and compared the theoretical patterns with that obtained from the experiment. They concluded that the SHG signal originated from surface electric dipole [33]. Omote *et al.* studied the SHG spectra as a function of the photon energy from the TiO₂ (110) and (001) surface. In order to study the surface electronic structure, they conducted phenomenological analysis to separate the contribution from various nonlinear susceptibility elements, and the dominant contribution was observed from the surface $\chi_{sijk}^{(2)}$ elements [34]. They noticed that the dominant nonlinear susceptibility element was $\chi_{s113}^{(2)}$ for both TiO₂ surfaces. They detected small contribution of the bulk quadrupoles. They performed an *ab initio* calculation by using the FLAPW method within the local density approximation and found that Ti-O-Ti-O- chains including the bridging oxygen atoms on the surface act as the main origin of the SHG signal generation from the TiO₂ (110) surface [34].

Takahashi *et al.* detected contribution of steps by comparing the SHG spectra from three kinds of stepped surfaces, TiO₂ (15 15 4), (13 9 0) and (671) with that from a flat (110) surface. They observed large SHG intensity from the step surfaces compared to the flat (110) surface that is shown by the following Fig. 1.1.2.2 [22]. In Fig. 1.1.2.2, The SHG intensity patterns of TiO₂ (15 15 4) and (671) were very similar for the Pin-Sout polarization combination. It might be due to the same electronic states. The patterns were different for the Sin-Sout polarization combination. More asymmetric shape was observed for the TiO₂ (671) compared to the TiO₂ (15 15 4) for the Sin-Sout polarization combination. The reason might

be the existence of the lower symmetry of TiO₂ (671) sample [22]. However, The SHG intensity of the TiO₂ (13 9 0) surface was very different from that of the (15 15 4) and (671) surfaces for both Pin-Sout and Sin-Sout polarization combinations due to the different miscut angle. On the other hand, the SHG intensity of TiO₂ (110) was very low for both Pin-Sout and Sin-Sout polarization combinations and it was at the noise level [22]. They could successfully separate the step contribution of surface $\chi_{sijk}^{(2)}$ elements from stepped surfaces of TiO₂ (15 15 4), (13 9 0) and (671), respectively, because the symmetry was broken at the periodic steps within the surface plane [22].

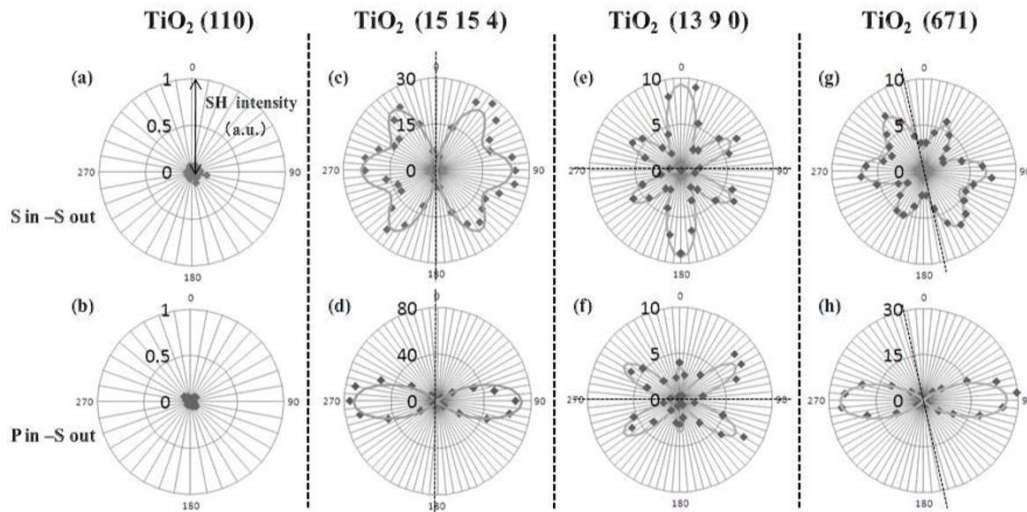


Figure 1.1.2.2. SHG intensity patterns as a function of the sample rotation angle for the polarization combinations Sin-Sout and Pin-Sout. Dots represent experimental data, and curves represent phenomenologically fitted curves. Incident angle and photon energy were 2^o and 2.33 eV, respectively. The dashed lines represent the sample rotation angles with SH electric field E(2 ω) parallel to the step edges.

In another report [35], they observed strong SHG/SFG responses from the stepped TiO₂ (17 18 1) and (15 13 0) surfaces compared to the flat (011) and (110) in order to understand the electronic states of terraces and steps. The resonances in the SHG and SFG

spectra for each sample suggested that they were due to the valence-conduction interband electronic transitions at the steps. More specifically the local density of states at the step of the vicinal surfaces was distributed right above the valence band maximum (VBM) and right below the conduction band minimum (CBM) [35].

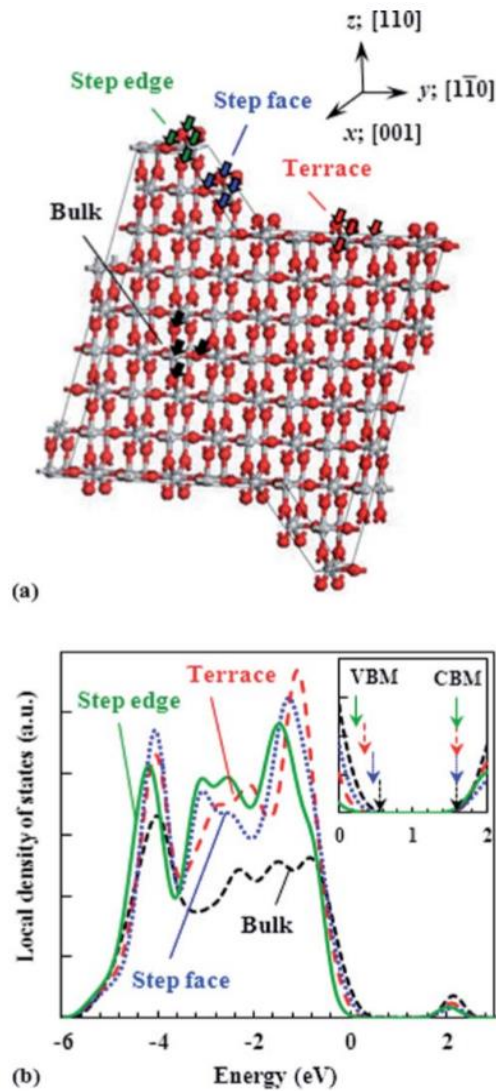


Figure 1.1.2.3. (a) A rutile TiO₂ slab model for the density functional theory (DFT) calculation of the local density of states (LDOS). The surface of the slab model consists of a (110) terrace and a double-layer step parallel to [0 0 1] with a (100) step face. (b) Calculated LDOS for bulk, a terrace, a step face, and a step edge. For each structure, the LDOS at the four atoms indicated by the arrows in (a) is summed up to yield the total LDOS at the

structure. The inset in (b) is the magnified scale of the LDOS near the band-gap region. The arrows in the inset indicate VBM and CBM for each structure. Here, zero corresponds to the energy of the Fermi energy.

Fig. 1.1.2.3 (a) showed the slab model drawn based on the AFM observation for (15 13 0) surface. This surface consists of multilayer step bunches and (110) surface having long terrace with a terrace width of about 20-25 nm towards the [1-10] direction [35]. However, since the size of the model system was limited, they assumed that the surface was composed of a bilayer step with a (100) step face, and a (110) terrace with a terrace width of four unit cells (2.6nm) along [1-10] direction. Thickness of the slab was nine layers. The local density of states (LDOS) was calculated for bulk, a terrace, a step face and a step edge as shown in Fig. 1.1.2.3 (b). According to this figure, it was clear that the LDOS at the VBM varies for the step and terrace significantly but it was very similar around the CBM and had almost the same energy. This energy shift for VBM might be due to the surface relaxation. However, the red shift for LDOS were significant for the step edge, step face and the terrace [35]. The band-gap energy for the top edges of the step bunches // [001] is larger than that for their hillsides and the (110) terraces. Therefore, it is concluded that the LDOS around the VBM for the top edges of the step bunches // [001] undergoes a red shift from the corresponding DOS for the bulk more significantly than that for their hillside and the (110) terraces does [35].

The red shift of the LDOS around the VBM for the top edges of the step bunches can give high oxidation power to free holes at these sites, as free holes extract electrons from adsorbed molecules more strongly with the increase in their potential energy (redox potential). However, they could not clearly state that whether these free holes really contribute to

methylene blue photodegradation reactions or not. They could not explain clearly the origin of the high reactivity of the step bunches, especially the ones // [001], as well as that of the (011) face in terms of trap states or LDOS near the band-gap regions. They finally conclude that they should not consider only the static surface electronic properties but also dynamic properties at TiO₂ surfaces after UV excitation [35].

S. Nakamura *et al.* observed electronic states from the anatase TiO₂ (101) surface in order to elucidate the mechanism of catalytic reaction on the surface. They found that the optical nonlinearity mainly originated from the surface rather than bulk [36]. H. Sano *et al.* theoretically calculated the SHG response on TiO₂ (110) face by using self-consistent full potential linearized augmented plane-wave (FLAPW) method [37]. Their theoretical calculation well agreed with the experimental findings. The results exhibited that the strong SHG response originated from the zigzag chains of TiO₂ (110) face consisting of bridging oxygen and neighbouring sixfold coordinated titanium atoms at two photon energy of 4eV [37]. H. Takahashi *et al.* observed the electronic states of stepped TiO₂ (15 15 4) by SHG method as a function of photon energy. They successfully separated the step and terrace contribution of the stepped TiO₂ (15 15 4) and compared the results with the TiO₂ (110) face. The step and terrace contribution from both the samples were very different indeed due to their different electronic structure [38]. The SHG spectra for the TiO₂ (15 15 4) and TiO₂ (110) surfaces is shown by the following Fig. 1.1.2.4.

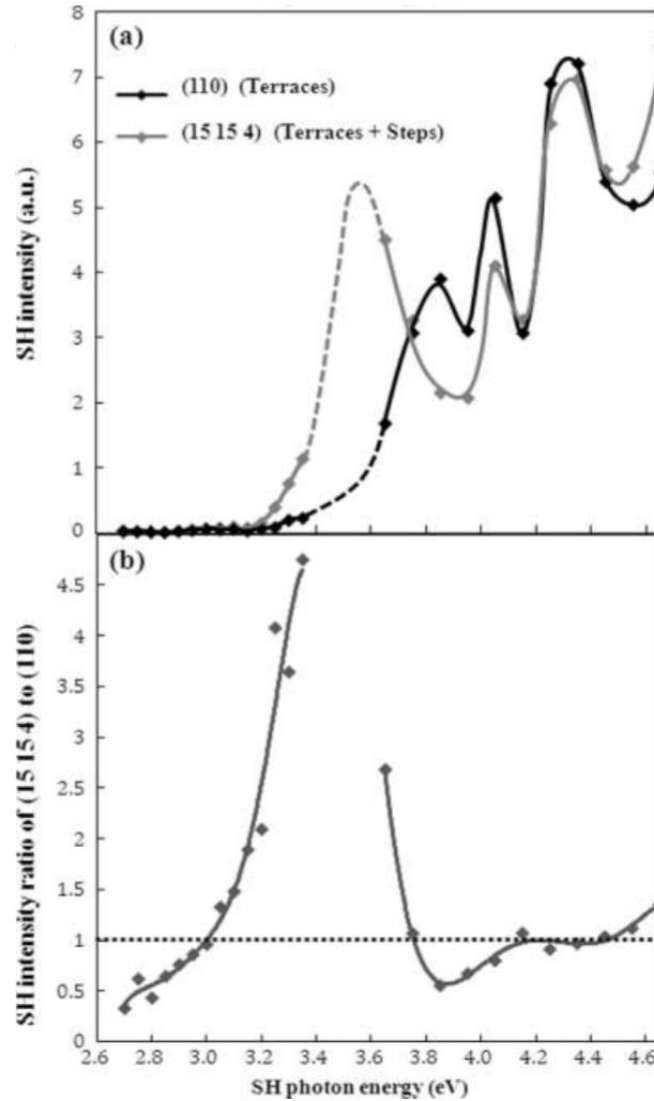


Figure 1.1.2.4. (a) SHG spectra for the TiO_2 (110) and (15 15 4) surfaces with the incident angle of 45° . The polarization combination was Pin-Pout. The incident azimuth was such that $k_{\parallel} \parallel [0\ 0\ 1]$. (b) The ratio of SHG intensity for the TiO_2 (15 15 4) surface to that for the (110) surface. The curves are guidelines.

Fig. 1.1.2.4 (a) shows the SHG spectra of the TiO_2 (110) and (15 15 4) surfaces as a function of photon energy for Pin-Pout polarization combination. The obtained spectra for these two surfaces were different due to their different electronic states. More specifically the spectrum of TiO_2 (15 15 4) was different due to its step contribution. In Fig. 1.1.2.4 (b),

the curve corresponds to the SHG intensity ratio of the TiO_2 (15 15 4) and TiO_2 (110) surfaces. This intensity ratio was more than unity. Therefore, the deviation of this SHG intensity ratio was due to the contribution of the step surface. The electronic states of the step surface was different from the electronic states of terrace surface. So, the SHG intensity was very strong at photon energy 3.6 eV due to the step contribution.

My motivation came from the above listed research works. Many researches have been conducted on the SHG measurement from the flat or stepped TiO_2 surfaces and analyzed their electronic states particularly the electronic states of the steps and terraces. However, they did not observe the SHG response from the interface between the Au and flat or stepped TiO_2 surface. They also did not investigate the electronic states of the Au/ TiO_2 interface. For this reason, I intended to investigate the SHG signal of the stepped Au/ TiO_2 (320) interface and study the electronic states of the interface by separating their step and terrace contributions. I choose (320) face because this face contains atomic steps in [1-10] direction and from the literature it is known that the step structure acts as active sites for the catalytic reactions [35]. So, from the catalytic point of view, the electronic state study of this crystallographic index is important in order to explore the catalytic mechanism. For these reason, I intended to use (320) crystallographic index.

As it is well known, surface defects such as steps and kinks play an important role in generating active sites for catalytic reactions, so it is vital to study the structure and the electronic states of such surface defects in order to understand their catalytic performances. Thus, it would be very informative if we analyse the SHG response from the interface of TiO_2 atomic stepped surface decorated by Au. In this research, a rutile type TiO_2 (320) single

crystal surface with the step height of 0.3 nm will be used as a substrate. The SHG method can be one of the ideal methods to measure step contribution of this atomic scale step structure by using the symmetry selection property, while other surface tools are not very sensitive because the number of steps are normally lower than the terrace atoms. Because the other tools are not so sensitive like SHG to the symmetry structure, it is difficult to separate the step and terrace contribution precisely. Therefore, only SHG can pick up step contribution for oriented steps and using the advantages of its symmetry selection property. So far as we know, there has been no previous observation of SHG from the stepped Au/TiO₂ interface.

In this work, I attempted to detect optical second harmonic generation signal from steps on the TiO₂ surface decorated by a Au film of 2 nm thickness and tried to separate the terrace and step contributions. On the TiO₂ (320) surface plane there is a structural asymmetry in the $[\bar{2}30]$ direction and this should induce SHG. I measured azimuthal angle and polarization dependent SHG intensity patterns at photon energies 1.17 eV and 2.33 eV for Au/TiO₂ (320) and TiO₂ (320) samples. I calculated the second order nonlinear optical susceptibility elements from the experimental results and separated the step and terrace contributions from both the samples. This analysis provides an important step for the future SHG spectroscopy of the electronic states of the Au/TiO₂ (320) interface as a function of the photon energy and the spectrum will be closely related to the catalytic activity of this interface.

1.2 Objective of this research

The following points summarize the main objectives of my research:

- (a) I will fabricate the 2nm Au film on the stepped TiO₂ (320) surface and characterized it.
- (b) Then I will measure the anisotropic SHG response from the Au/TiO₂ (320) interface.
- (c) One of the most interesting objective of this research is to separate the step and terrace contribution of the Au/TiO₂ (320) interface to understand the electronic states precisely.

1.3 Outline of the thesis

This thesis consists of six chapters and are organized as follows:

Chapter 1 describes the general introduction and research motivation. In this chapter, I list literature of the catalytic properties of TiO₂ and Au separately and Au/TiO₂ interface. The SHG response on the Au/TiO₂ interface and flat and stepped TiO₂ are discussed precisely. I also discuss the reason for studying the electronic states of Au/TiO₂ (320) interface by using SHG method. This chapter also includes the objectives of this present research and outline of this research work as well.

Chapter 2 explains the theoretical background related to the nonlinear optics, principle of nonlinear optical media. Here I discuss the principle of SHG, brief explanation of nonlinear susceptibility elements, theory of surface plasmon resonance (SPR), theory of scanning electron microscope and atomic force microscope.

Chapter 3 shows the experimental procedure. Here, I describe the sample preparation including sample cleaning by HF etching, annealing of TiO₂ (320) and Au deposition on stepped TiO₂ (320) surface in a UHV chamber. I also discuss the optical setup for the SHG and linear experiment and mention the advantages of SHG spectroscopic measurement.

Chapter 4 deals with the main experimental results and discussion of this research work. I discuss the anisotropic SHG response and the origin of the anisotropic behavior. I also elaborately explain the separation of the step and terrace contribution of the nonlinear susceptibility elements originates from step and terrace of Au/TiO₂ interface and morphology by using SEM and AFM. I also discuss the linear optical reflectivity and transmission spectra obtained from the Au/TiO₂ interface.

Chapter 5 describes the general conclusion based on the obtained main results from this research work.

I also included all the lists of my publications and conference proceedings and the participation in the national and international conferences in the appendix sections. I added some appendixes related to this research work.

References

- [1] Discovery and applications of photocatalysis — Creating a comfortable future by making use of light energy; Japan Nanonet Bulletin Issue 44, 12 May 2005.
- [2] Hanaor, Dorian A. H.; Sorrell, Charles C. "Review of the anatase to rutile phase transformation". *Journal of Materials Science*. 46, 4, 855–874, 2011.
- [3] J. G. Li and T. Ishigaki, *Acta Materialia*, 52, 17, 5143-5150, 2004.
- [4] R. Austin and S.-f. Lim, "The Sackler Colloquium on Pormoses and Perils in Nanotechnology for Medicine," *PNAS*, vol. 105, no. 45, pp. 17217-17221, 2008.
- [5] K. Hashimoto, H. Irie and A. Fujishima, "TiO₂ Photocatalysis: A Historical Overview and Future Prospects," *Japanese Journal of Applied Physics*, vol. 44, no. 12, pp. 8269-8285, 2005.
- [6] K. Prasad, D. V. Pinjari, A. B. Pandit and S. T. Mhaske, *Ultrasonics Sonochemistry*, 17, 2, 409-415, 2010.
- [7] S. Woodley and C. Catlow, "Structure prediction of titania phases: Implementation of Darwinian versus Lamarckian concepts in an Evolutionary Algorithm," *Computational Materials Science*, vol. 45, no. 1, pp. 84-95, 2009.
- [8] Wikipedia, "Titanium Dioxide," Wikipedia, 11 April 2012. [Online]. Available: http://en.wikipedia.org/wiki/Titanium_dioxide. [Accessed 16 April 2012].
- [9] G. C. Bond, The catalytic properties of gold, *Gold Bulletin*, Vol. 5, Issue 1, pp 11-13, 1972.
- [10] A. Alshammahi and V. N. Kalevaru, Supported gold nanoparticles as promising catalysts, <http://dx.doi.org/10.5772/64394>, 2016.
- [11] Hermans LA, Interaction of Nickel ions with silica Geus JW. *Stud. Surf. Sci. Catal.* Oxford, UK; 4, 113, 1979.

- [12] P. Miedziak, M. Sankar, N. Dimitratos, J. A. Lopez-Sanchez, A. F. Carley, D. W. Knight, S. T. Taylor, C. J. Kiely, G. J. Hutchings, Oxidation of benzyl alcohol using supported gold palladium nanoparticles. *Catal. Today*. 163(1), 47–54, 2011.
- [13] Z. Duan and G. Henkelman, *ACS Catal.* 5, 1589-1595, (2015).
- [14] Q. Yao, C. Wang, H. Wang, H. Yan, and J. Lu, *J. Phys. Chem. C* 120, 9174-9183, (2016).
- [15] M. Valden, S. Pak, X. Lai, and D. W. Goodman, *Catal. Lett.* 56, 7-10, (1998).
- [16] M. Haruta, S. Tsubota, T. Kobayshi, H. Kageyama, M. J. Ganet, and B. Delmon, *J. Catal.* 144, 175, (1993).
- [17] S. Tsubota, T. Nakamura, K. Tanaka, and M. Haruta, *Catal. Lett.* 56, 131, (1998).
- [18] X. Z. Li and F. B. Li, *Environ. Sci. Technol.*, 35, 2381-2387, 2001.
- [19] I. M. Arabatzis, T. Stergiopoulos, D. Andreeva, S. Kitova, S. G. Neophytides and P. Falaras, *Journal of Catalysis*, 220, 127-135, 2003.
- [20] A. S. Castillo, M. C. Hermo, B. R. Gonzalez, M. P. Lorenzo, Z. Wang, X. T. Kong, A. O. Govorov and M. A. C. Duarte; *J. Phys. Chem. C*. 120, 11690-11699, 2016.
- [21] T. Minato, H. Kato, M. Kawai; *Surface Science*. Vol. 27, No. 6, 319-325, 2006.
- [22] H. Takahashi, R. Watanabe, and G. Mizutani, *e-J. Surf. Sci. Nanotech.* 8, 84-88, (2010).
- [23] X. Lai, T. P. St. Clair, M. Valden, and D. W. Goodman, *Surface Science* 59, 25-52, (1998).
- [24] T. Tanaka, A. Sumiya, H. Sawada, Y. Kondo, and K. Takayanagi, *Surface Science* 619, 39-43, (2014).
- [25] A. Aiboushev, A. Astafiev, O. M. Sarkisov, and V. A. Nadochenko, *Journal of Physics* 291, 012040, (2011).
- [26] Z. K. Zhou, M. Li, X. R. Su, Y. Y. Zhai, H. Song, J. B. Han, and Z. H. Hao, *Phys. Stat. Sol. (a)* 205, 345-349, (2008).

- [27] C. Zhang, Y. Liu, G. You, B. Li, J. Shi, and S. Qian, *Physica B* 357, 334-339, (2005).
- [28] M. Kyoung and M. Lee, *Bull. Korean Chem. Soc.* 21, 1, (2000).
- [29] L. Marrucci, D. Paparo, G. Cerrone, C. de Lisio, E. Santamato, S. Solimeno, S. Ardizzone, and P. Quagliotto, *Optics and Lasers in Engineering* 37, 601-610, (2002).
- [30] J. J. H. Gielis, P. M. Gevers, I. M. P. Aarts, M. C. M. Van de Sanden, and W. M. M. Kessels, *J. Vac. Technol. A* 26, 6, (2008).
- [31] S. Cattaneo, E. Vuorimaa, H. Lemmetyinen, and M. Kauranen, *J. Chem. Phys.* 120, 19, (2004).
- [32] X. Quelin, J. Sakars, A. Bourdon, and P. Gadenne, *Physica B* 279, 102-104, (2000).
- [33] E. Kobayashi, T. Wagasugi, G. Mizutani, and S. Ushioda, *Surface Science* 402-404, 537-541, (1998).
- [34] M. Omote, H. Kitaoka, E. Kobayashi, O. Suzuki, K. Aratake, H. Sano, G. Mizutani, W. Wolf, and R. Podlucky, *Journal of Physics: Condensed Matter.* 17, 8, S175-S200, (2005).
- [35] H. Takahashi, R. Watanabe, Y. Miyauchi and G. Mizutani, *J. Chem. Phys.* 134, 154704, (2011).
- [36] S. Nakamura, K. Matsuda, T. Wakasugi, E. Kobayashi, G. Mizutani, S. Ushioda, T. Sekiya and S. Kurita, *Journal of Luminescence*, 87-89, 862-864, 2000.
- [37] H. Sano, G. Mizutani, W. Wolf and R. Podlucky, *Phys. Rev. B.*, 70, 125411, 2004.
- [38] H. Takahashi, R. Watanabe and G. Mizutani, *Surf. Interface Anal.* 42, 1659-1662, 2010.

Chapter 2: Theoretical Background

2.1 Maxwell's equations

2.2 Nonlinear Optics

2.2.1 Theoretical background of nonlinear optics

2.2.2 Nonlinear polarization induced in non-

centrosymmetric media

2.3 Second harmonic generation (SHG)

2.4 Nonlinear susceptibility: classical anharmonic oscillator model

2.5 Basic theory of scanning electron microscope (SEM)

2.6 Basic theory of atomic force microscope (AFM)

2.7 Basic theory of surface plasmon resonance (SPR)

References

Theoretical background

In this chapter, I will discuss about the theoretical part related to this research and about the nonlinear susceptibility elements along with their symmetric consideration. Further, I will discuss about the brief theory of some microscopic observation.

2.1 Maxwell's equations

I would like to discuss briefly about the Maxwell's equations those simply represents the little matter interaction. These equations are very important for describing the electromagnetic theory. The four important Maxwell's equations are given below,

$$\nabla \times \tilde{E} = - \frac{\partial \tilde{B}}{\partial t} \quad (1)$$

$$\nabla \times \tilde{H} = \frac{\partial \tilde{D}}{\partial t} + \tilde{j} \quad (2)$$

$$\nabla \cdot \tilde{D} = \tilde{\rho} \quad (3)$$

$$\nabla \cdot \tilde{B} = 0 \quad (4)$$

Here, \tilde{E} and \tilde{B} are the electric field and magnetic induction, respectively. \tilde{D} and \tilde{H} are the dielectric vector and magnetic field, respectively. $\tilde{\rho}$ and \tilde{j} are the electric charge density and current density, respectively.

The magnetic induction \tilde{B} and the magnetic field \tilde{H} is related according to the following equation,

$$\tilde{B} = \mu_0 \tilde{H} \quad (5)$$

The dielectric vector can be defined as

$$\tilde{D} = \varepsilon_0 \tilde{E} + \tilde{P} \quad (6)$$

Here, ε_0 is the electric permittivity of the free space and \tilde{P} is the polarization induced by the electric field.

The relation between the induced polarization and electric field is almost linear when the value of electric field is very small. The linear polarization equation can be written as follows,

$$\tilde{P} = \varepsilon_0 \chi \tilde{E} \quad (7)$$

Putting the value of \tilde{P} in to the equation (6)

$$\tilde{D} = \varepsilon_0 \tilde{E} + \tilde{P} = \varepsilon_0 \tilde{E} + \varepsilon_0 \chi \tilde{E} = (1 + \chi) \varepsilon_0 \tilde{E} = \varepsilon \varepsilon_0 \tilde{E} \quad (8)$$

Where, χ is the linear susceptibility and it is related to the index of refraction [1].

$$\chi = n^2 - 1$$

χ acts as a tensor and shows different values with different polarization of light and different symmetry system. In case of large values of electric field, the relation between the polarization and the electric field also changes and it becomes nonlinear. The nonlinear polarization equation can be written as a series of expansion,

$$\tilde{P} = \varepsilon_0 \chi^{(1)} \tilde{E} + \varepsilon_0 \chi^{(2)} \tilde{E} \tilde{E} + \varepsilon_0 \chi^{(3)} \tilde{E} \tilde{E} \tilde{E} + \dots \quad (9)$$

From the equation (9), it is clear that the polarization have a significant role in the nonlinear optical phenomena and $\chi^{(2)}$ is the second order optical nonlinear susceptibility elements.

2.2 Nonlinear Optics

Nonlinear optics (NLO) is the study of nonlinear interaction between the light and matter. More precisely, the nonlinearity observed due to the nonlinear responses of a material with the interaction of electric field of light and the source of light should be very intense. The only source of intense light is laser [2]. After the discovery of laser by Theodore Harold Maiman in 1960, the reevaluation occurred in the field of nonlinear optics by the invention of different types of exciting phenomena namely second harmonic generation (SHG), sum frequency generation (SFG), difference frequency generation (DFG), optical parametric oscillation (OPO), third harmonic generation (THG) [2-3].

2.2.1 Theoretical background of nonlinear optics

In order to understand the interaction between light wave and nonlinear medium properly, it is important to calculate the electromagnetic wave equation for nonlinear medium by using the Maxwell's equations discussed in the part 2.1.

For the calculation of electromagnetic wave equations, we consider curl on the both side of equation (1) and we have,

$$\nabla \times \nabla \times \tilde{\mathbf{E}} = \nabla \times \left(-\frac{\partial \tilde{\mathbf{B}}}{\partial t} \right) \Rightarrow \nabla \times \nabla \times \tilde{\mathbf{E}} = -\frac{\partial}{\partial t} (\nabla \times \tilde{\mathbf{B}}) \quad (10)$$

Substituting the value of equation (5) into equation (10), we have,

$$\nabla \times \nabla \times \tilde{\mathbf{E}} = -\mu_0 \frac{\partial}{\partial t} (\nabla \times \tilde{\mathbf{H}}) \quad (11)$$

Now putting the value of equation (2) in to equation (11), We got,

$$\nabla \times \nabla \times \tilde{\mathbf{E}} = -\mu_0 \frac{\partial}{\partial t} \left(\frac{\partial \tilde{\mathbf{D}}}{\partial t} + \tilde{\mathbf{J}} \right) \Rightarrow \nabla \times \nabla \times \tilde{\mathbf{E}} = -\mu_0 \frac{\partial^2 \tilde{\mathbf{D}}}{\partial t^2} - \mu_0 \frac{\partial \tilde{\mathbf{J}}}{\partial t} \quad (12)$$

We consider the electric current density is $\tilde{\mathbf{J}} = 0$, then we have,

$$\begin{aligned} \nabla \times \nabla \times \tilde{\mathbf{E}} &= -\mu_0 \frac{\partial^2 \tilde{\mathbf{D}}}{\partial t^2} \\ \nabla \times \nabla \times \tilde{\mathbf{E}} + \mu_0 \frac{\partial^2 \tilde{\mathbf{D}}}{\partial t^2} &= 0 \end{aligned} \quad (13)$$

Now from equation (6), replacing the value $\tilde{\mathbf{D}} = \epsilon_0 \tilde{\mathbf{E}} + \tilde{\mathbf{P}}$ into equation (13), we can write,

$$\begin{aligned} \nabla \times \nabla \times \tilde{\mathbf{E}} + \mu_0 \frac{\partial^2}{\partial t^2} (\epsilon_0 \tilde{\mathbf{E}} + \tilde{\mathbf{P}}) &= 0 \\ \nabla \times \nabla \times \tilde{\mathbf{E}} + \frac{1}{c^2} \frac{\partial^2}{\partial t^2} \tilde{\mathbf{E}} &= -\frac{1}{\epsilon_0 c^2} \frac{\partial^2 \tilde{\mathbf{P}}}{\partial t^2} \end{aligned} \quad (14)$$

In the field of nonlinear optics, equation (14) is generally known as the Maxwell's source-term equation or nonlinear wave equation. Under the appropriate boundary conditions, it can be written as,

$$\nabla \times \nabla \times \tilde{\mathbf{E}} = \nabla(\nabla \cdot \tilde{\mathbf{E}}) - \nabla^2 \tilde{\mathbf{E}} \quad (15)$$

We can write, $\nabla \cdot \tilde{\mathbf{E}} = 0$, when $\nabla \cdot \tilde{\mathbf{D}} = 0$ for the anisotropic media, The equation (15) becomes,

$$\nabla \times \nabla \times \tilde{\mathbf{E}} = -\nabla^2 \tilde{\mathbf{E}} \quad (16)$$

Using equation (14) and (16) we have,

$$-\nabla^2 \tilde{\mathbf{E}} + \frac{1}{c^2} \frac{\partial^2}{\partial t^2} \tilde{\mathbf{E}} = -\frac{1}{\epsilon_0 c^2} \frac{\partial^2 \tilde{\mathbf{P}}}{\partial t^2} \quad (17)$$

In equation (17), the \tilde{P} is denoted by the induced polarization by the electric field application linearly and nonlinearly and the polarization can be divided into linear and nonlinear part according to the equation (18).

$$\tilde{P} = \tilde{P}^{(1)} + \tilde{P}^{NL} \quad (18)$$

The dielectric vector can also be separated into linear and nonlinear parts,

$$\tilde{D} = \tilde{E} + 4\pi\tilde{P}^{(1)} + 4\pi\tilde{P}^{NL} \quad (19)$$

$$\tilde{D} = \tilde{D}^{(1)} + P^{NL} \quad (20)$$

The linear equation of dielectric vector can be written as,

$$\tilde{D}^{(1)} = \epsilon_0\tilde{E} + \tilde{P}^{(1)} \quad (21)$$

By using the equation (21) and (14) can be expressed as,

$$-\nabla^2\tilde{E} + \frac{1}{\epsilon_0 c^2} \frac{\partial^2 \tilde{D}^{(1)}}{\partial t^2} = -\frac{1}{\epsilon_0 c^2} \frac{\partial^2 \tilde{P}^{NL}}{\partial t^2} \quad (22)$$

Equation (22) is also known as the wave equation for the nondispersive and lossless medium. A new relation among the linear dielectric vector, electric field and linear dielectric tensor for isotropic material can be expressed by the following formula,

$$\tilde{D}^{(1)} = \epsilon_0 \epsilon^{(1)} \cdot \tilde{E} \quad (23)$$

For the isotropic and nondispersive materials, the dielectric tensor $\epsilon^{(1)}$ is scalar in quantity. So, the equation (22) becomes

$$-\nabla^2\tilde{E} + \frac{\epsilon^{(1)}}{c^2} \frac{\partial^2 \tilde{E}}{\partial t^2} = -\frac{1}{\epsilon_0 c^2} \frac{\partial^2 \tilde{P}^{NL}}{\partial t^2} \quad (24)$$

The equation (24) is generally known as inhomogeneous wave equation and the right hand side of this equation can be expressed as nonlinear source term of a medium.

Each frequency components of a particular field can be separated in a dispersive medium. The sum of the different frequency components can be expressed by the linear dielectric vector, electric field and nonlinear polarization. The equations for the different frequency components can written as,

$$\tilde{E}(r, t) = \sum_n \tilde{E}_n(r, t) \quad \text{with} \quad \tilde{E}(r, t) = E_n(r) e^{-i\omega_n t} \quad (25)$$

$$\tilde{D}^{(1)}(r, t) = \sum_n \tilde{D}_n^{(1)} D_n^{(1)}(r, t) \quad \text{with} \quad \tilde{D}_n^{(1)}(r, t) = D_n^{(1)}(r) e^{-i\omega_n t} = \epsilon^{(1)}(\omega_n) \cdot \tilde{E}_n(r, t) \quad (26)$$

$$\tilde{P}^{NL}(r, t) = \sum_n \tilde{P}_n^{NL}(r, t) \quad \text{with} \quad \tilde{P}_n^{NL}(r, t) = P_n^{NL}(r) e^{-i\omega_n t} \quad (27)$$

By introducing equation (25) and (26) into the equation (22), we can deduce a wave equation which is equivalent to the equation (24) and that is valid for each frequency components of the field. Then the equation (24) can be written as,

$$-\nabla^2 \tilde{E}_n + \frac{\epsilon^{(1)}(\omega_n)}{c^2} \frac{\partial^2 \tilde{E}_n}{\partial t^2} = - \frac{1}{\epsilon_0 c^2} \frac{\partial^2 \tilde{P}_n^{NL}}{\partial t^2} \quad (28)$$

The equation (28) is the key equation in the field of nonlinear optics and helps to determine the origin of the optical nonlinearity.

2.2.2 Nonlinear polarization induced in noncentrosymmetric media

The second-order nonlinear optical process is only allowed from the surface or interface where the symmetry is broken or having no inversion symmetry. On the contrary, it is forbidden in the bulk of medium consisting inversion symmetry [4]. However, the third-order nonlinear optical process is allowed in both media having inversion and no inversion symmetry [3]. In order to understand precisely, we will now discuss about the occurrences of optical nonlinearity.

In case of linear medium, the polarization is induced by the applied electric field linearly where the electric field strength is small. The equation can be expressed as,

$$\tilde{P}(t) = \epsilon_0 \chi^{(1)} \tilde{E}(t) \quad (29)$$

Here, $\chi^{(1)}$ is the linear optical susceptibility and ϵ_0 is known as electric permittivity of vacuum.

In case of nonlinear medium, the polarization is induced by the applied electric field nonlinearly where the electric field strength is significantly large. This relation can be written as the following equation expressed as a power series,

$$\tilde{P}(t) = \epsilon_0 [\chi^{(1)} \tilde{E}(t) + \chi^{(2)} \tilde{E}^{(2)}(t) + \chi^{(3)} \tilde{E}^{(3)}(t) + \dots] \quad (30)$$

$$\equiv \tilde{P}^{(1)}(t) + \tilde{P}^{(2)}(t) + \tilde{P}^{(3)}(t) + \dots \quad (31)$$

$$P^{NL}(t) = \tilde{P}^{(2)}(t) + \tilde{P}^{(3)}(t) + \dots \quad (32)$$

Where, $\chi^{(2)}$ and $\chi^{(3)}$ are denoted as the second and the third order nonlinear optical susceptibilities. In addition $\tilde{P}^{(2)}(t)$ and $\tilde{P}^{(3)}(t)$ can be expressed as the second-order and

third-order nonlinear polarization, respectively. When an electric field is applied to a nonlinear medium, we can write the following expression,

$$\tilde{\mathbf{E}}(t) = E \cos \omega t \quad (33)$$

In case of centrosymmetric medium, the sign of the polarization will be changed obviously along with changing the sign of applied electric field to that medium. So the following equation for second-order nonlinear polarization can be written as,

$$-\tilde{\mathbf{P}}^{(2)}(t) = \epsilon_0 \chi^{(2)} [-\tilde{\mathbf{E}}(t)]^2 = \epsilon_0 \chi^{(2)} \tilde{\mathbf{E}}^{(2)}(t) \quad (33)$$

For centrosymmetric medium, the following expression is valid.

$$\tilde{\mathbf{P}}^{(2)}(t) = -\tilde{\mathbf{P}}^{(2)}(t) \quad (34)$$

The equation (34) will be satisfied only when there is no nonvanishing nonlinear susceptibility elements and therefore the induced polarization will be equal to zero. So, in case of centrosymmetric medium, the second-order nonlinearity is forbidden according to the dipole approximation rule. Fig. 2.2.2.1 shows a graphical representation for clarifying the linear and nonlinear response with respect to the applied electric field. Fig. 2.2.2.1 (a) exhibits the waveform of electric field, (b) expresses the linear optical response with respect to the applied electric field as shown in (a). The curves (c) and (d) show the nonlinear optical responses in the centrosymmetric and noncentrosymmetric medium, respectively.

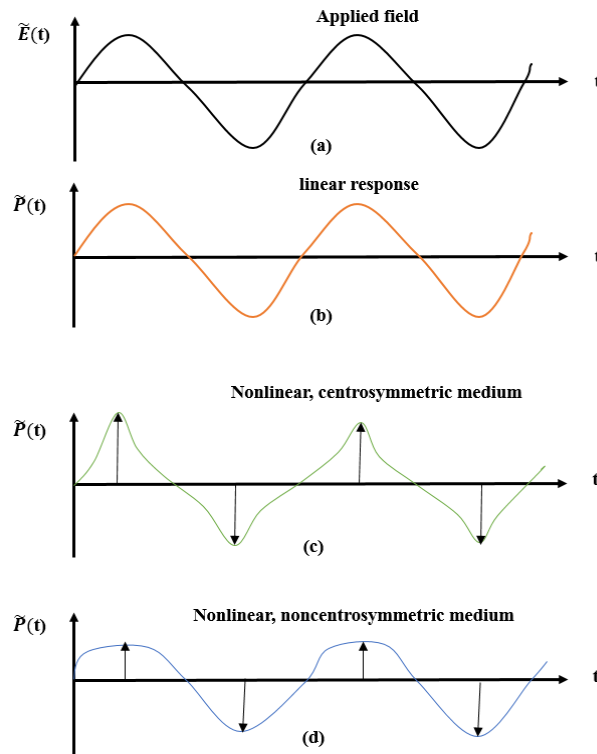


Figure 2.2.2.1. The graphical presentations for linear and nonlinear polarizations with respect to the applied electric field in various media [3].

In addition, the response of applied electric field is different for centrosymmetric and noncentrosymmetric media. From Fig. 2.2.2.1 (c) and (d), it is clearly seen that the electric field response considering both upward and downward directions are same for centrosymmetric media and it is quite different for noncentrosymmetric media where the symmetry is broken.

2.3 Second harmonic generation (SHG)

Second harmonic generation (SHG) involved with the conversion of the two photons of same frequency ω into a single photon of frequency 2ω and half the wavelength of the incident probe [5]. SHG is forbidden in the bulk of medium with inversion symmetry within the electric dipole approximation [6]. It has submonolayer sensitivity to the surface and interface of

centrosymmetric media because it is only allowed in broken symmetric structure [6]. Other attractive feature of SHG is that it is non-invasive and contactless and it can be applied to “in situ” and in “real-time” experiments with a good time resolution [7].

The basic principle of SHG technique is expressed by the following Fig.2.3.1

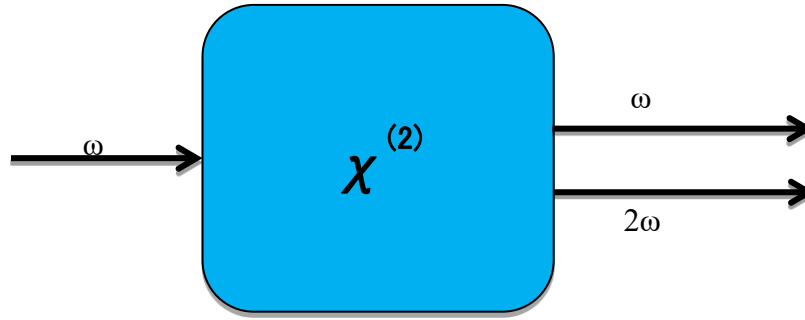


Fig.2.3.1: Basic principle of SHG technique

The equation of electric field can be written as,

$$\tilde{E}(t) = E e^{-i\omega t} + E^* e^{i\omega t} \quad (35)$$

At non-centrosymmetric medium, the induced polarization by the applied electric field equation can be expressed as,

$$\begin{aligned} \tilde{P}^{(2)}(t) &= \epsilon_0 \chi^{(2)} \tilde{E}^2(t) \\ &= \epsilon_0 \chi^{(2)} [E e^{-i\omega t} + E^* e^{i\omega t}]^2 \\ &= \epsilon_0 \chi^{(2)} [E^2 e^{-i2\omega t} + 2EE^* + E^{*2} e^{i2\omega t}] \\ &= \epsilon_0 \chi^{(2)} [E^2 e^{-i2\omega t} + E^{*2} e^{i2\omega t} + 2EE^*] \end{aligned}$$

$$= 2\epsilon_o\chi^{(2)}EE^* + \epsilon_o\chi^{(2)}[E^2e^{-i2\omega t} + E^{*2}e^{i2\omega t}]$$

$$\tilde{P}^{(2)}(t) = 2\epsilon_o\chi^{(2)}EE^* + [\epsilon_o\chi^{(2)}E^2e^{-i2\omega t} + C.C] \quad (36)$$

The first term on the right hand side of equation (36) have contribution to the nonlinear polarization at zero frequency and the second term provides contribution at 2ω frequency.

Second harmonic generation (SHG) involved with the conversion of the two photons of same frequency ω into a single photon of frequency 2ω and half the wavelength of the incident probe [5]. The energy level diagram and the SHG intensity curve as a function of photon energy are shown in Fig. 2.3.2 (a) and (b). In general, the electronic resonance occurred only when the energy of two photon excitation is large enough to lift an electron from its ground state to the excited state and relaxation occurs when returning to the ground state by dissipating its gained energy. The SHG intensity can be enhanced significantly due to the occurrence of electronic resonance.

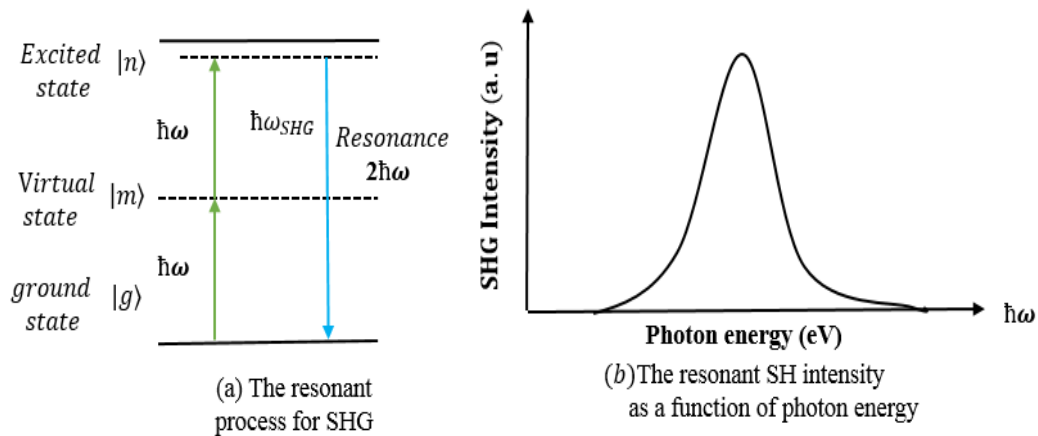


Fig.2.3.2: (a) The energy diagram of SHG technique (b) SHG intensity curve in terms of photon energy

According to the dipole approximation rule,

$$\vec{E}(t) = \vec{E}(\omega) \cos(\omega t) \quad (37)$$

$$\vec{P}_i^{NL}(2\omega) = \sum_{j,k} \overleftrightarrow{\chi}_{ijk}^{(2)}(2\omega: \omega, \omega) : \vec{E}_j(\omega) \vec{E}_k(\omega) \quad (38)$$

When the symmetry of a medium is broken, the nonlinear polarization can be induced by the applied electric field. The SHG intensity is proportional to the squared nonlinear polarization and can be expressed by the following equation,

$$\vec{I}^{(2\omega)} \propto |\vec{P}_i^{NL}(2\omega)|^2 \quad (39)$$

From equation (38) and (39), we can write,

$$\vec{I}^{(2\omega)} = |\overleftrightarrow{\chi}_{ijk}^{(2)}|^2 (I^{(\omega)})^2 \quad (40)$$

The equation (40) indicates that the relation between the intensity of incident and SHG lights are quadratic. $\overleftrightarrow{\chi}_{ijk}^{(2)}$ is the third-rank tensor and known as surface second-order optical nonlinear susceptibility. It consists of 27 elements. The i, is the components of SHG and j and k are the incident field's component. The 27 $\overleftrightarrow{\chi}_{ijk}^{(2)}$ elements can be written as a matrix form shown in the following equation,

$$\chi_{ijk}^{(2)} = \begin{pmatrix} \chi_{xxx}^{(2)} & \chi_{xxy}^{(2)} & \chi_{xxz}^{(2)} & \chi_{xyx}^{(2)} & \chi_{xyy}^{(2)} & \chi_{xyz}^{(2)} & \chi_{xzx}^{(2)} & \chi_{xzy}^{(2)} & \chi_{xzz}^{(2)} \\ \chi_{yxx}^{(2)} & \chi_{yxy}^{(2)} & \chi_{yxz}^{(2)} & \chi_{yyx}^{(2)} & \chi_{yyy}^{(2)} & \chi_{yyz}^{(2)} & \chi_{yzx}^{(2)} & \chi_{yzy}^{(2)} & \chi_{yzz}^{(2)} \\ \chi_{zxx}^{(2)} & \chi_{zxy}^{(2)} & \chi_{zxz}^{(2)} & \chi_{zyx}^{(2)} & \chi_{zyy}^{(2)} & \chi_{zyz}^{(2)} & \chi_{zzx}^{(2)} & \chi_{zzy}^{(2)} & \chi_{zzz}^{(2)} \end{pmatrix} \quad (41)$$

The equations of nonlinear polarization for xyz components converted from index ijk can be written as follows, where the symmetry is not considered.

$$P_x^{NL}(2\omega) = \chi_{xxx}^{(2)} E_x E_x + \chi_{xxy}^{(2)} E_x E_y + \chi_{xxz}^{(2)} E_x E_z + \chi_{xyx}^{(2)} E_y E_x + \chi_{xyy}^{(2)} E_y E_y \\ + \chi_{xyz}^{(2)} E_y E_z + \chi_{xzx}^{(2)} E_z E_x + \chi_{xzy}^{(2)} E_z E_y + \chi_{xzz}^{(2)} E_z E_z \quad (42)$$

$$P_y^{NL}(2\omega) = \chi_{yxx}^{(2)} E_x E_x + \chi_{yxy}^{(2)} E_x E_y + \chi_{yxz}^{(2)} E_x E_z + \chi_{yyx}^{(2)} E_y E_x + \chi_{yyy}^{(2)} E_y E_y \\ + \chi_{yyz}^{(2)} E_y E_z + \chi_{yzx}^{(2)} E_z E_x + \chi_{yzy}^{(2)} E_z E_y + \chi_{yzz}^{(2)} E_z E_z \quad (43)$$

$$P_z^{NL}(2\omega) = \chi_{zxx}^{(2)} E_x E_x + \chi_{zxy}^{(2)} E_x E_y + \chi_{zxx}^{(2)} E_x E_z + \chi_{zyx}^{(2)} E_y E_x + \chi_{zyy}^{(2)} E_y E_y \\ + \chi_{zyz}^{(2)} E_y E_z + \chi_{zzx}^{(2)} E_z E_x + \chi_{zzx}^{(2)} E_z E_y + \chi_{zzz}^{(2)} E_z E_z \quad (44)$$

For the $C_{\infty v}$ symmetry, the inversion operation can be conducted with respect to the C axis rotation, which occurred 180° along z-axis.

$$(P_x^{(2)}, P_y^{(2)}, P_z^{(2)}) \Rightarrow (-P_x^{(2)}, -P_y^{(2)}, P_z^{(2)}), \quad \text{and}$$

$$(E_x, E_y, E_z) \Rightarrow (-E_x, -E_y, E_z)$$

Now we can write the equations of x, y and z-components for the optical second order nonlinear polarizations are in the following,

$$-P_x^{NL}(2\omega) = \chi_{xxx}^{(2)} E_x E_x + \chi_{xxy}^{(2)} E_x E_y - \chi_{xxz}^{(2)} E_x E_z + \chi_{xyx}^{(2)} E_y E_x + \chi_{xyy}^{(2)} E_y E_y \\ - \chi_{xyz}^{(2)} E_y E_z - \chi_{xzx}^{(2)} E_z E_x - \chi_{xzy}^{(2)} E_z E_y + \chi_{xzz}^{(2)} E_z E_z \quad (45)$$

$$-P_y^{NL}(2\omega) = \chi_{yxx}^{(2)} E_x E_x + \chi_{yxy}^{(2)} E_x E_y - \chi_{yxz}^{(2)} E_x E_z + \chi_{yyx}^{(2)} E_y E_x + \chi_{yyy}^{(2)} E_y E_y \\ - \chi_{yyz}^{(2)} E_y E_z - \chi_{yzx}^{(2)} E_z E_x - \chi_{yzy}^{(2)} E_z E_y + \chi_{yzz}^{(2)} E_z E_z \quad (46)$$

$$P_z^{NL}(2\omega) = \chi_{zxx}^{(2)} E_x E_x + \chi_{zxy}^{(2)} E_x E_y - \chi_{zxx}^{(2)} E_x E_z + \chi_{zyx}^{(2)} E_y E_x + \chi_{zyy}^{(2)} E_y E_y \\ - \chi_{zyz}^{(2)} E_y E_z - \chi_{zzx}^{(2)} E_z E_x - \chi_{zzx}^{(2)} E_z E_y + \chi_{zzz}^{(2)} E_z E_z \quad (47)$$

We can now express the components of second-order optical nonlinear polarization by the equations written below through the comparison of the equations (42), (43) and (44) with the equations (45), (46) and (47).

$$P_x^{NL}(2\omega) = \chi_{xxz}^{(2)} E_x E_z + \chi_{xyy}^{(2)} E_y E_z + \chi_{xzx}^{(2)} E_z E_x + \chi_{xzy}^{(2)} E_z E_y \quad (48)$$

$$P_y^{NL}(2\omega) = \chi_{yxx}^{(2)} E_x E_z + \chi_{yyy}^{(2)} E_y E_z + \chi_{yzz}^{(2)} E_z E_x + \chi_{yzy}^{(2)} E_z E_y \quad (49)$$

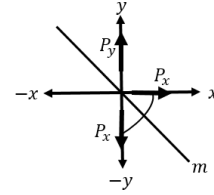
$$P_z^{NL}(2\omega) = \chi_{zxx}^{(2)} E_x E_z + \chi_{zyy}^{(2)} E_y E_z + \chi_{zzx}^{(2)} E_z E_x + \chi_{zzy}^{(2)} E_z E_y \quad (50)$$

Some nonlinear susceptibility elements can be eliminated from the above equations by conducting the inversion symmetry operation between the x, y plane and we can rewrite the following equations,

$$(1) (P_x^{(2)}, P_y^{(2)}, P_z^{(2)}) \Rightarrow (-P_x^{(2)}, P_y^{(2)}, P_z^{(2)}), \quad (E_x, E_y, E_z) \Rightarrow (-E_x, E_y, E_z),$$

$$(2) (P_x^{(2)}, P_y^{(2)}, P_z^{(2)}) \Rightarrow (P_x^{(2)}, -P_y^{(2)}, P_z^{(2)}), \quad (E_x, E_y, E_z) \Rightarrow (E_x, -E_y, E_z),$$

$$(3) (P_x^{(2)}, P_y^{(2)}, P_z^{(2)}) \Rightarrow (-P_y^{(2)}, P_x^{(2)}, P_z^{(2)}), \quad (E_x, E_y, E_z) \Rightarrow (-E_y, E_x, E_z)$$



$$P_x^{NL}(2\omega) = \chi_{xxx}^{(2)} E_x E_z + \chi_{xzx}^{(2)} E_z E_x \quad (51)$$

$$P_y^{NL}(2\omega) = \chi_{yyy}^{(2)} E_y E_z + \chi_{yzy}^{(2)} E_z E_y \quad (52)$$

$$P_z^{NL}(2\omega) = \chi_{zxx}^{(2)} E_x E_x + \chi_{zyy}^{(2)} E_y E_y + \chi_{zzz}^{(2)} E_z E_z \quad (53)$$

There are seven nonzero second order optical nonlinear susceptibility elements shown in the equations (51), (52) and (53). It is possible to exchange the j and k subscript by applying the permutation transformation according to the rules and regulation of Kleinman symmetry. Therefore, the susceptibility elements considering the $C_{\infty v}$ symmetry can be written as [3],

$$\chi_{zzz}^{(2)},$$

$$\chi_{zxx}^{(2)} = \chi_{zyy}^{(2)},$$

$$\chi_{xzx}^{(2)} = \chi_{xxz}^{(2)} = \chi_{yzy}^{(2)} = \chi_{yyz}^{(2)}$$

Actually, the $\overleftrightarrow{\chi}_{ijk}^{(2)}$ elements depend on many factors. Among the 27 $\overleftrightarrow{\chi}_{ijk}^{(2)}$ elements, the vanishing and nonvanishing $\overleftrightarrow{\chi}_{ijk}^{(2)}$ elements depend on symmetry, experimental conditions including polarization of light, incident angle, intensity of the incident and SHG beam. So the total 27 $\overleftrightarrow{\chi}_{ijk}^{(2)}$ elements can be written by the following matrix equations [3],

$$\begin{pmatrix} P_x^{NL}(2\omega) \\ P_y^{NL}(2\omega) \\ P_z^{NL}(2\omega) \end{pmatrix} = \epsilon_0 \begin{pmatrix} \chi_{xxx}^{(2)} & \chi_{xxy}^{(2)} & \chi_{xxz}^{(2)} & \chi_{xyx}^{(2)} & \chi_{xyy}^{(2)} & \chi_{xyz}^{(2)} & \chi_{xzx}^{(2)} & \chi_{xzy}^{(2)} & \chi_{xzz}^{(2)} \\ \chi_{yxx}^{(2)} & \chi_{yyx}^{(2)} & \chi_{yxy}^{(2)} & \chi_{yyx}^{(2)} & \chi_{yyy}^{(2)} & \chi_{yyz}^{(2)} & \chi_{yzz}^{(2)} & \chi_{yzy}^{(2)} & \chi_{yzz}^{(2)} \\ \chi_{zxx}^{(2)} & \chi_{zxy}^{(2)} & \chi_{zxx}^{(2)} & \chi_{zyx}^{(2)} & \chi_{zyy}^{(2)} & \chi_{zyz}^{(2)} & \chi_{zxx}^{(2)} & \chi_{zzy}^{(2)} & \chi_{zxx}^{(2)} \end{pmatrix} \begin{pmatrix} E_x E_x \\ E_x E_y \\ E_x E_z \\ E_x E_y \\ E_y E_y \\ E_y E_z \\ E_z E_x \\ E_y E_z \\ E_z E_z \end{pmatrix} \quad (54)$$

It is well known that, Au/TiO₂ (320) and bare TiO₂ (320) samples have C_s symmetry system. For centrosymmetric media, all the directions should be same and the value of $\chi_{ijk}^{(2)}$ for two opposing directions are identical [8].

$$\chi_{ijk}^{(2)} = \chi_{-i-j-k}^{(2)} \quad (55)$$

Furthermore, from the physical point of view as the coordinates are reversed, the physical phenomenon must also change the sign or,

$$\chi_{ijk}^{(2)} = \chi_{-i-j-k}^{(2)} = -\chi_{i-j-k}^{(2)} = \chi_{ij-k}^{(2)} = -\chi_{ijk}^{(2)} \quad (56)$$

The result shows that SHG is forbidden in the centrosymmetric medium. However, at the surface or interface, the broken symmetry exists and therefore SHG is active. In order to obtain the number of nonlinear susceptibility elements, one can examine the symmetry of the nanostructure material lying on the planar surfaces. TiO₂ (320) substrate contains C_s symmetry

system. In case of the Au/TiO₂ (320) and bare TiO₂ (320) samples, Fig. 2.3.3 shows the crystallographic direction along with the directions of the incident and SHG beam.

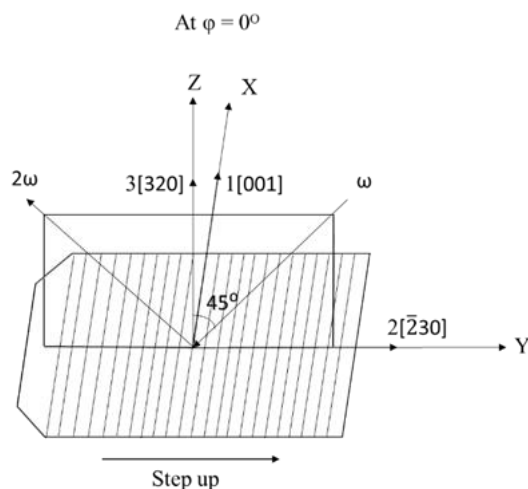


Figure 2.3.3. Schematic diagram of the stepped TiO₂ (320) substrate with the incidence plane. Here the coordinate symbols are (X,Y,Z)=Laboratory Coordinates and (1,2,3)≡Sample Coordinate. The sample coordinates are indicated by 1[001], 2[$\bar{2}$ 30] and 3[320] directions. The azimuthal angle ϕ is the angle between X and the axis 1. The angle ϕ equals to zero when X and the axis 1 are on the same direction as illustrated above. The mirror plane of the surface structure is the 2-3 plane. In a more specific way, direction 2 is parallel to surface that lies in the mirror plane of TiO₂ and perpendicular to step edge where the symmetry is broken and direction 3 is perpendicular to the surface of the stepped TiO₂ sample. At $\phi = 0^\circ$, direction 2 corresponds to the step up direction and it is same direction with laboratory coordinate Y.

Here 1, 2, and 3 represent the [001], [$\bar{2}$ 30], and [320] directions on the stepped TiO₂ (320) surface, respectively, and their axes are fixed to the sample as shown in Fig. 2.3.3. The mirror plane of the surface structure is the 2-3 plane. In the directions 2 and 3 there are broken symmetries

caused by the surface steps and the terrace surface, respectively. With C_s symmetry, we have “2≠-2” and “3≠-3” but “1=-1”. We can apply the equation (56) to assign the number of nonlinear susceptibility elements. The result is shown in table 2.3.1.

Table 2.3.1. Assignment of the number of $\chi_{ijk}^{(2)}$ element in the case of C_s symmetry.		
$\chi_{ijk}^{(2)}$	Apply to equation (56)	Contribution
$\chi_{222}^{(2)}$	no effect	Yes
$\chi_{221}^{(2)}$	$\chi_{221}^{(2)} = \chi_{22-1}^{(2)} = -\chi_{221}^{(2)}$	No
$\chi_{223}^{(2)}$	no effect	Yes
$\chi_{212}^{(2)}$	$\chi_{212}^{(2)} = \chi_{2-12}^{(2)} = -\chi_{212}^{(2)}$	No
$\chi_{211}^{(2)}$	$\chi_{211}^{(2)} = \chi_{2-1-1}^{(2)} = \chi_{211}^{(2)}$	Yes
$\chi_{213}^{(2)}$	$\chi_{213}^{(2)} = \chi_{2-13}^{(2)} = -\chi_{213}^{(2)}$	No
$\chi_{232}^{(2)}$	no effect	Yes
$\chi_{231}^{(2)}$	$\chi_{231}^{(2)} = \chi_{23-1}^{(2)} = -\chi_{231}^{(2)}$	No
$\chi_{233}^{(2)}$	no effect	Yes
$\chi_{122}^{(2)}$	$\chi_{122}^{(2)} = \chi_{-122}^{(2)} = -\chi_{122}^{(2)}$	No
$\chi_{121}^{(2)}$	$\chi_{121}^{(2)} = \chi_{-12-1}^{(2)} = \chi_{121}^{(2)}$	Yes
$\chi_{123}^{(2)}$	$\chi_{123}^{(2)} = \chi_{-123}^{(2)} = -\chi_{123}^{(2)}$	No
$\chi_{112}^{(2)}$	$\chi_{112}^{(2)} = \chi_{-1-12}^{(2)} = \chi_{112}^{(2)}$	Yes

$\chi_{111}^{(2)}$	$\chi_{111}^{(2)} = \chi_{-1-1-1}^{(2)} = -\chi_{111}^{(2)}$	No
$\chi_{113}^{(2)}$	$\chi_{113}^{(2)} = \chi_{-1-13}^{(2)} = \chi_{113}^{(2)}$	Yes
$\chi_{132}^{(2)}$	$\chi_{132}^{(2)} = \chi_{-132}^{(2)} = -\chi_{132}^{(2)}$	No
$\chi_{131}^{(2)}$	$\chi_{131}^{(2)} = \chi_{-13-1}^{(2)} = \chi_{131}^{(2)}$	Yes
$\chi_{133}^{(2)}$	$\chi_{133}^{(2)} = \chi_{-133}^{(2)} = -\chi_{133}^{(2)}$	No
$\chi_{322}^{(2)}$	no effect	Yes
$\chi_{321}^{(2)}$	$\chi_{321}^{(2)} = \chi_{32-1}^{(2)} = -\chi_{321}^{(2)}$	No
$\chi_{323}^{(2)}$	no effect	Yes
$\chi_{312}^{(2)}$	$\chi_{312}^{(2)} = \chi_{3-12}^{(2)} = -\chi_{312}^{(2)}$	No
$\chi_{311}^{(2)}$	$\chi_{311}^{(2)} = \chi_{3-1-1}^{(2)} = \chi_{311}^{(2)}$	Yes
$\chi_{313}^{(2)}$	$\chi_{313}^{(2)} = \chi_{3-13}^{(2)} = -\chi_{313}^{(2)}$	No
$\chi_{332}^{(2)}$	no effect	Yes
$\chi_{331}^{(2)}$	$\chi_{331}^{(2)} = \chi_{33-1}^{(2)} = -\chi_{331}^{(2)}$	No
$\chi_{333}^{(2)}$	no effect	Yes

Thus I have ten independent nonlinear susceptibility elements, $\chi_{223}^{(2)} = \chi_{232}^{(2)}$, $\chi_{113}^{(2)} = \chi_{131}^{(2)}$, $\chi_{112}^{(2)} = \chi_{121}^{(2)}$, $\chi_{211}^{(2)}$, $\chi_{222}^{(2)}$, $\chi_{233}^{(2)}$, $\chi_{323}^{(2)} = \chi_{332}^{(2)}$, $\chi_{311}^{(2)}$, $\chi_{322}^{(2)}$, and $\chi_{333}^{(2)}$ in the case of C_s symmetry. Then I divide these ten independent nonlinear susceptibility elements into two groups considering their step and terrace contributions. Hence the nonlinear susceptibility elements $\chi_{121}^{(2)}$,

$\chi_{211}^{(2)}$, $\chi_{222}^{(2)}$, $\chi_{233}^{(2)}$, and $\chi_{323}^{(2)}$ with odd number of suffices 2 originate from the step contribution. The other five susceptibilities $\chi_{113}^{(2)}$, $\chi_{223}^{(2)}$, $\chi_{311}^{(2)}$, $\chi_{322}^{(2)}$, and $\chi_{333}^{(2)}$ with odd numbers of suffices 3 originate from the terrace contribution. Here the terrace contribution contains both that from the TiO₂ (110) terrace and that from the Au film surface. I will discuss the contribution from steps and terraces of the Au/TiO₂ (320) interface more precisely in the results and discussion chapter.

2.4. Nonlinear susceptibility: classical anharmonic oscillator model

It is well known that nonlinear optical susceptibility χ^2 is a complex tensor. In the noncentrosymmetric medium, there should be some nonzero optical second order nonlinear susceptibility elements. The motion of electron in the x coordinate can be expressed by the following differential equation,

$$m \frac{d^2x}{dt^2} + 2m\gamma \frac{dx}{dt} + m\omega_0^2x + ax^2 + bx^3 + \dots = -\lambda e\vec{E}(t) \quad (57)$$

Here, ω_0 = oscillation frequency of the electron,

m = electron mass,

γ =the damping factor, and

ax^2 and bx^3 are the nonlinear terms.

λ = expansion parameter that expresses the perturbation strength.

Fig. 2.4.1 showed the potential curves for dissimilar form of restoring force. Only of the vicinity of the origin may this potential take the form of an harmonic oscillator potential. The

anharmonicity of the problem is also present in the form of the restoring force. Despite the rudimentary aspect of the model shown in Fig. 2.4.1, one can observe that several important features have been incorporated [9]. The anharmonicity of the restoring force is present through a simple mathematical expression. Also the free system possesses a characteristic resonance frequency given by, $\omega_o = \sqrt{k/m}$. For small displacements where the system's anharmonicity can be neglected. However, in order to properly account for resonances, in particular to avoid singular points at resonances. A friction constant γ was introduced here for defining the friction force. This force may be viewed as the resultant of all the interactions between the electron under investigation and the other electron-nucleus systems lying in the neighbourhood [9].

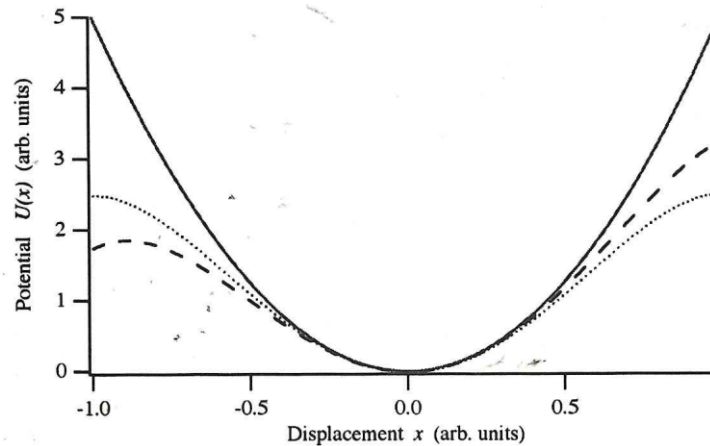


Fig.2.4.1 The potential curves for dissimilar form of restoring force. Solid, dotted and dashed lines define the linear (only k nonzero), nonlinear first order (k and b nonzero) and nonlinear second order (k , a and b nonzero) [9].

Now the equation (57) can be written as,

$$\frac{d^2x}{dt^2} + 2\gamma \frac{dx}{dt} + \omega_0^2 x + (a/m)x^2 + (b/m)x^3 + \dots = -\lambda e \vec{E}(t)/m \quad (58)$$

The equation of electric field, $E(t) = E^{(1)} = E^\omega \exp(-i\omega t)$ (59)

Assuming that, $x = x^{(1)} = x^\omega \exp(-i\omega t)$ (60)

The power series of expansion of λ can be written by the following equation,

$$\lambda \ddot{x}^{(1)} + \lambda^2 \ddot{x}^{(2)} + 2\gamma(\lambda \dot{x}^{(1)} + \lambda^2 \dot{x}^{(2)}) + \omega_0^2(\lambda x^{(1)} + \lambda^2 x^{(2)}) + a/m(\lambda x^{(1)} + \lambda^2 x^{(2)})^2 + b/m(\lambda x^{(1)} + \lambda^2 x^{(2)})^3 + \dots = -\lambda e \vec{E}(t)/m \quad (61)$$

Now considering the coefficient of λ in equation (61), we have,

$$\ddot{x}^{(1)} + 2\gamma \dot{x}^{(1)} + \omega_0^2 x^{(1)} = -e \vec{E}(t)/m \quad (62)$$

Now the following equation can be written by using the equations (59) and (60) for obtaining the first order of λ and solving that,

$$x^{(1)} = \frac{e}{m} \frac{E^{(1)}}{\omega_0^2 - \omega^2 - i2\gamma\omega} \quad (63)$$

Now considering the coefficient of λ^2 in equation (61), we have,

$$\ddot{x}^{(2)} + 2\gamma \dot{x}^{(2)} + \omega_0^2 x^{(2)} + a/m(x^{(1)})^2 = 0 \quad (64)$$

Let, $x^{(2)} = x^{2\omega} \exp(-i2\omega t)$ (65)

From the equations (63) and (64), I can write,

$$\chi^{(2)} = -\frac{ae^2 (E^\omega)^2 \exp(-i2\omega t)}{m^2 [\omega_0^2 - \omega^2 - i2\gamma\omega]^2} \frac{1}{[\omega_0^2 - 4\omega^2 - i4\gamma\omega]} \quad (66)$$

The following equation denotes the relation between the linear polarization, linear susceptibility and applied electric field,

$$\vec{P}^{(1)} = \epsilon_0 \chi^{(1)} \vec{E}(t) \quad (67)$$

Then linear polarization can be expressed as,

$$\vec{P}^{(1)} = -Nex^{(1)} \quad (68)$$

So, the equation for the linear susceptibility can be written as,

$$\chi^{(1)} = \frac{Ne^2}{\epsilon_0 m} \left(\frac{1}{\omega_0^2 - \omega^2 - i2\gamma\omega} \right) \quad (69)$$

The following equation is for the second order nonlinear polarization,

$$\vec{P}^{(2)} = \epsilon_0 \chi^{(2)} \vec{E}^2(t) \quad (70)$$

Thus, the second order optical nonlinear susceptibility can be written by the following equation,

$$\chi^{(2)} = \frac{Neae^2}{\epsilon_0 m^2} \frac{1}{[\omega_0^2 - \omega^2 - i2\gamma\omega]^2} \frac{1}{[\omega_0^2 - 4\omega^2 - i4\gamma\omega]} \quad (71)$$

Fig. 2.4.2 showed the linear optical susceptibility curves as a function of frequency. Here, Solid line denotes the dispersion function on real part and dashed line represents resonance

function on the imaginary part in the region of the resonance. Both curves were calculated from the following equation (72),

$$\varepsilon^\omega = 1 + \chi^1(\omega) = 1 + \frac{Ne^2}{\varepsilon_0 m [\omega_0^2 - \omega^2 - 2i\gamma\omega]} \quad (72)$$

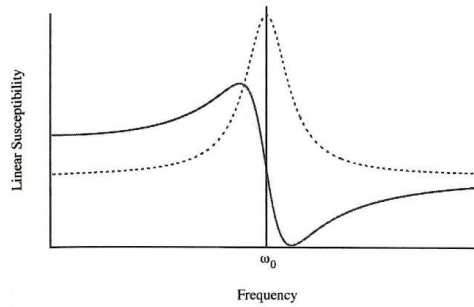


Fig.2.4.2. Linear optical dielectric constant in terms of frequency. Solid line denotes the dispersion function on real part and dashed line represents resonance function on the imaginary part [9].

Fig. 2.4.3 exhibited nonlinear optical susceptibility $\chi^2(2\omega; \omega, \omega)$ as a function of the fundamental frequency ω . Here, the solid and dashed lines were representing the real part and imaginary part of $\chi^2(2\omega; \omega, \omega)$ [9]. According to the equation (71), the observed nonlinear susceptibility scaled like the a coefficient having two resonance frequencies: one when the fundamental frequency equals the frequency ω_0 of the system and the other one when the harmonic frequency 2ω equals ω_0 , which is clearly shown in Fig. 2.5.3. By this model, it is possible to describe the main features of the nonlinear susceptibility of the medium [9].

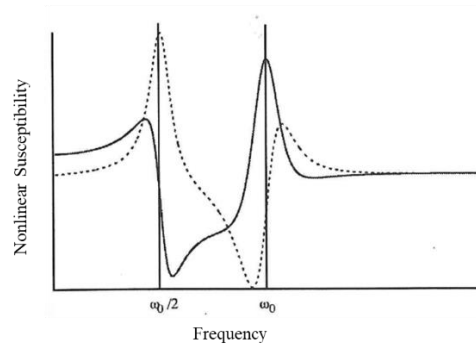


Fig.2.4.3 Nonlinear optical susceptibility in terms of fundamental frequency. Solid and dashed lines are expressing the real and the imaginary part of second order nonlinear susceptibility [9].

2.5 Basic theory of scanning electron microscope (SEM)

Scanning electron microscope is a modern tool to observe the surface image of a sample. It uses high energetic electron beam that strikes on the sample surface and many different types of signal may evolve which contains many information about the surface of the material. In SEM technology, among the other signals the secondary electron are detected mainly by a detector to produce a topographic image [10].

In the instrumental arrangement of SEM, the electron gun is used as a source of electron beam. This gun is usually made up of tungsten metal due to its high melting temperature, is excited thermionically to emit the high energetic electron beam. The electron beam with energy range 0.2 to 40 keV is directed through the condenser lens, objective lens, deflection coils and final lens aperture in order to strike the sample surface [10]. There is back scattering electron (BSE) and secondary electron (SE) detector to detect the signal created by the interaction between the material surface and the electron beam. The best resolution for the SEM is less than 1 nm. The SEM can be operated at both the cryogenic and elevated temperature [11]. It is possible to make the

magnification range from 10 to 500,000 times by the modern SEM machine. As the SEM is usually operated in the vacuum environment, it needs special sample preparation. The following schematic diagram is representing the SEM instrumental setup.

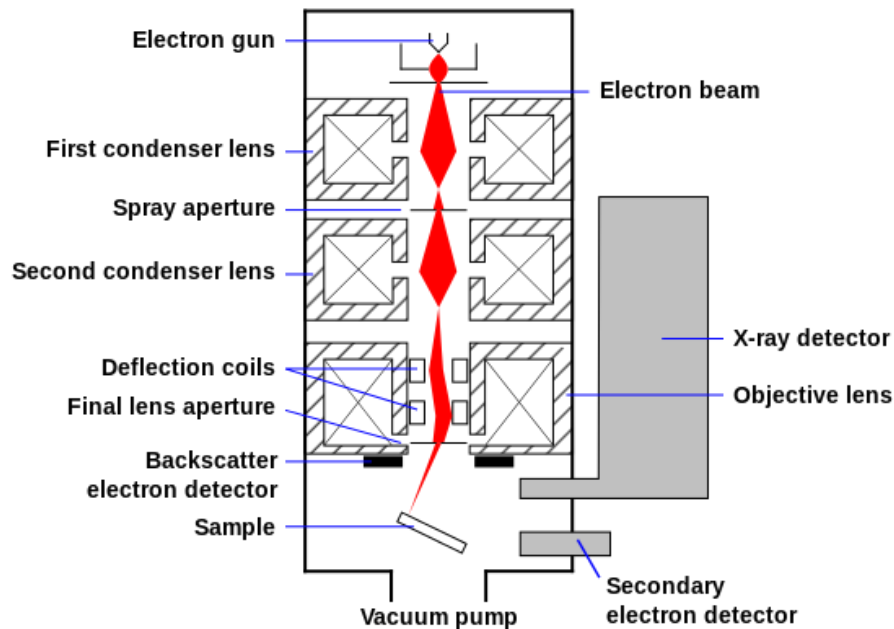


Figure 2.5.1. The schematic diagram for the SEM instrumental setup [10].

When a material surface is bombarded by the high energetic electron beam many types of signals are generated from the different part of the material surface including secondary electrons (SE), back-scattered electrons (BSE), X-rays, cathodoluminescence (CL), Auger electrons (AE) etc as Shown in Fig. 2.5.2. The interaction depth may vary from less than 100 nm to 5 μm . The secondary electrons are emitted from very close to the surface of a material. However, the emission of back scattering electrons are dependent on the atomic size of the material. The back scattering signals are stronger from the heavy material than that of the light material. The secondary and back scattering electrons are generated due to the inelastic and elastic interaction

between the material and the electron beam, respectively [10]. The mechanisms for the emission of secondary electrons, back scattering electrons and X-rays by the interaction between the electron beam and the surface of the material are illustrated by the following Fig. 2.5.3. The BSE and x-ray can provide the elemental and compositional information from the material surface. The SE are detected to create the SEM image that provides the morphological and topographical information of the material surface [10].

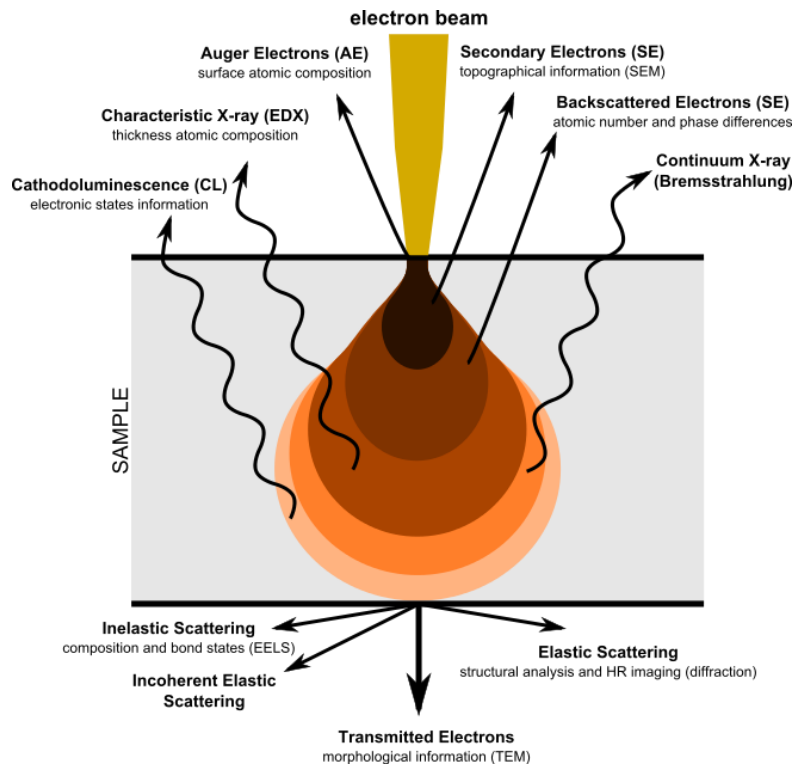


Figure 2.5.2. The different types of signal emitted from the different part of the interaction volume [10].

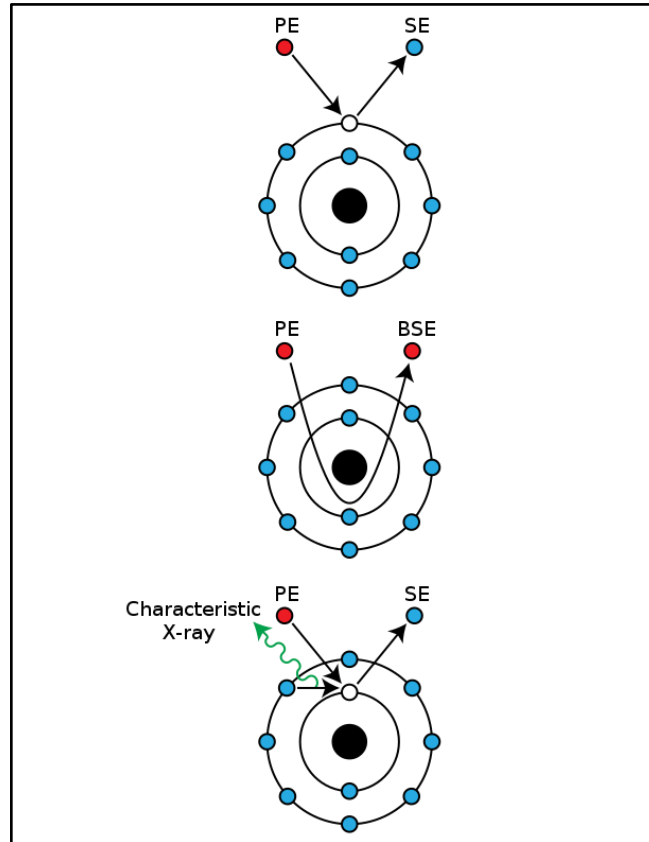


Figure 2.5.3. The mechanisms for the emission of secondary electrons, back scattering electrons and X-rays by the interaction between the electron beam and the surface of the material [10].

2.6 Basic theory of atomic force microscope (AFM)

Atomic Force Microscopy (AFM) is a scanning probe microscope ensuring the high resolution approximately fractions of nanometer and 1000 times better compared to the optical diffraction limit. The AFM acts as a blind person that is able to detect the information only by feeling or touching the objects [12].

Fig. 2.6.1 exhibit the basic instrumental setup for the AFM machine [13]. The different parts of the AFM are shown by the number included parentheses. In Fig. 2.6.1, the main part of

the AFM is a cantilever (1) attached by a support (2) and at one end of the support there is a piezoelectric elements (3) that helps to oscillate the cantilever. The other end of the cantilever contains a fixed sharp tip (4). The movement of the cantilever is recorded by a detector (5). During the experiment, a sample (6) is kept up on a sample holder/stage (8) and the rotation or movement of the sample as well as sample stage in x, y, z directions (0) with respect to the tip apex is controlled by a xyz drive (7). In this Fig. d is the distance between the tip and sample surface [13]. In most cases, the drives usually have an attachment with the sharp tip and sample holder.

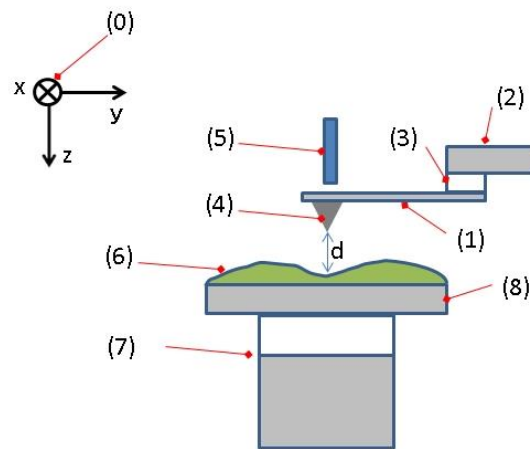


Figure 2.6.1. Instrumental previews of AFM setup (1) Cantilever, (2) Cantilever support, (3) Piezoelectric component that helps to oscillates the cantilever on the material surface, (4) Sharp tip attached at the end of the cantilever and act as the probe of AFM, (5) Detector that are able to record the movement of a cantilever, (6) Sample, (7): xyz drive that are used to move the sample and the sample stage in the (0) x, y, and z directions with respect to a tip apex and the sample stage [12].

The working principle of the AFM is easy and straightforward. It is comparable to the walking of blind man. Because the sharp tip of AFM go through the surface of the experimental

materials and the movement of the tip behaves according to the materials surface. More precisely a local force is developed between the tip and the sample surface [14]. The most attractive feature of the AFM is its sensitivity on the sample surface. It works by feeling and touching the sample surface without probing any kinds of light. The resolution of the AFM is far below the diffraction limit compared to the optical microscope because of the noninvolvement of application of any light in order to acquire the surface image of a material [14]. The main features of the AFM instrumental setup is illustrated by the following Fig. 2.6.2. The cantilever is usually made up of silicon or silicon nitride containing a sharp tip having radius of curvature of nanometer scale. AFM can be operated into different types of modes such as contact or static mode that create contact between the sample surface and the tip [14]. The other popular mode is dynamic or noncontact mode where there is no real contact between the tip and the sample surface. This method is also known as tapping mode. Only the cantilever is oscillated or vibrated near the surface of the material at a selected frequency. The AFM is able to provide the accurate topographic image of the surface of the sample with good resolution [14]. AFM can also produce the 3D image and can accurately measure the height or depth of the surface.

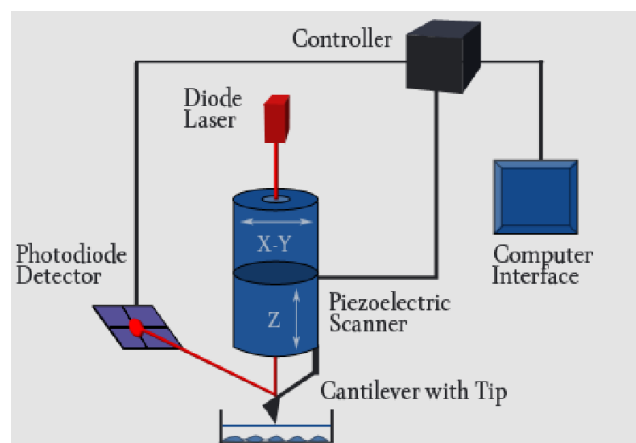


Figure 2.6.2. Schematic illustration of the main features of the AFM. A malleable cantilever containing a sharp tip at one end and they are connected to a piezoelectric xyz drive. The image is created through the photodetector and interface computer [14].

2.7 Basic theory of surface plasmon resonance (SPR)

The collective oscillations of the free electrons may occur in metal surface such as silver, gold or copper induced by the interacting electromagnetic field and they are known as surface plasmons [15]. Surface plasmons behave as a wave at the metal/dielectric interface. However, they are confined in the metallic nanostructure such as nanorods and nanoparticles are usually known as localized surface plasmon resonance (LSPR) [15]. The surface plasmons can play an important role to enhance the local electric field hugely. SPRs or LSPRs is the usually evaluated by considering the absorption properties of a particular metal/dielectric interface or the surface of metal nanoparticles, respectively [16].

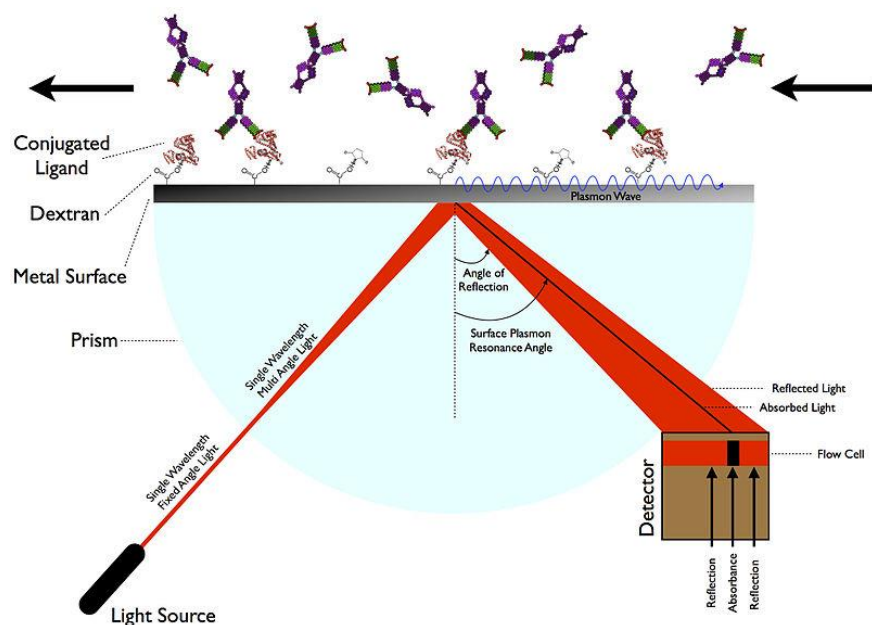


Figure 2.7.1. The basic principle of the generation of surface plasmon resonance (SPR) [16].

For achieving the surface plasmon resonance from a metal/dielectric interface or surface of the metal nanoparticle, it is necessary to excite the surface plasmon by applying the electromagnetic radiation usually in the visible or infrared range. Actually an electric field is created by the surface plasmons and when the external electric field is applied then an electronic oscillation occurs on the surface or interface due to the resonance [16]. This resonance occurs only when the frequency of that two fields are matched. The following dispersion relation governs surface plasmon resonance [16],

$$K(\omega) = \frac{\omega}{c} \sqrt{\frac{\epsilon_1 \epsilon_2 \mu_1 \mu_2}{\epsilon_1 \mu_1 + \epsilon_2 \mu_2}}$$

Here,

ϵ = relative permittivity of metal/glass interface

μ = relative permeability of metal/glass interface

The two types of well-established configurations such as Otto configuration and Kretschmann configuration [16] can describe how the surface plasmons are excited by the incident electric field of the light beam.

In Otto configuration, the incident light beam is irradiated on the wall of a glass prism and the total internal reflection of the light occurs inside the prism through the generation of a wave known as evanescent wave. Evanescent wave is known as an oscillating electric or magnetic field. However, the behavior of this wave is different from the electromagnetic wave such as propagation. This wave can not propagate as like as the electromagnetic wave but can concentrate the energy in the vicinity of the surface [17]. This evanescent wave is able to excite the surface

plasmons by interacting with the plasma waves generated on the surface of thin metal film usually gold or silver kept very near to the wall of the glass prism [16].

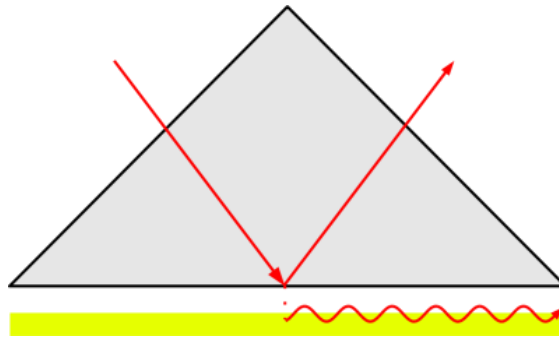


Figure 2.7.2. Otto configuration for the generation of surface plasmon resonance (SPR) [16].

The Kretschmann configuration is very popular and well known model for explaining the surface plasmon resonance. When a thin metal film is created on the glass surface and a light beam is irradiated on the wall of the glass surface an evanescent wave is generated. This evanescent wave can penetrate through the metal film and interact with the plasma waves on the surface of the film. By this way the surface plasmons can be excited at the interface region of metal/glass. In most practical applications, this Kretschmann configuration is extensively used [16].

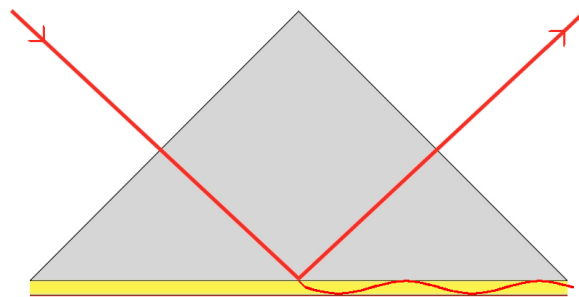


Figure 2.7.3. Kretschmann configuration for the generation of surface plasmon resonance (SPR) [16].

References

- [1] W. Cai and V. Shalaev, *Optical Metamaterials Fundamentals and Applications* (Springer), (2009).
- [2] Y. R. Shen, *the Principles of Nonlinear Optics*. (1984).
- [3] R. W. Boyd, *Nonlinear Optics, Third Edition*. (1992).
- [4]. Y.R. Shen, *Nature*, Vol. 337, 519-525, (1989).
- [5] R. M. Corn and D. A. Higgins, *Chem. Rev.*, 94, 107-125, (1994).
- [6] L. Marrucci, D. Paparo, G. Cerrone, C. de Lisio, E. Santamato, S. Solimeno, S. Ardizzone, and P. Quagliotto, *Optics and Lasers in Engineering* 37, 601-610, (2002).
- [7] J. J. H. Gielis, P. M. Gevers, I. M. P. Aarts, M. C. M. Van de Sanden, and W. M. M. Kessels, *J. Vac. Technol. A* 26, 6, (2008).
- [8] A. G. Lambert, P. B. Davies, and D. J. Neivandt, *Appl. Spectrosc. Rev.* 40, 103, (2005).
- [9] P. F. Brevet, *Surface Second Harmonic Generation*, Press polytechniques et universitaires romandes, (1996).
- [10] https://en.wikipedia.org/wiki/Scanning_electron_microscope
- [11] Debbie J Stokes, *Principles and Practice of Variable Pressure Environmental Scanning Electron Microscopy (VP-ESEM)*, John Wiley & Sons. ISBN 978-0470758748, (2008).
- [12] https://en.wikipedia.org/wiki/Atomic_force_microscopy.
- [13] Patent US4724318 - Atomic force microscope and method for imaging surfaces with atomic resolution.

[14] <https://medicine.tamhsc.edu/afm/principles.php>

[15] A. Lesuffleur, P. Gogol, P. Beauvillain, B. Guizal, D. Van Labeke, and P. Georges, J. Appl. Phys. 104, 124310, (2008).

[16] https://en.wikipedia.org/wiki/Surface_plasmon_resonance

[17] https://en.wikipedia.org/wiki/Evanescent_field

Chapter 3: Experimental Procedure

3.1 Sample Preparation

3.1.1 Sample Cleaning by HF etching

3.1.2 Annealing of TiO₂ (320) substrate

3.1.3 Au deposition on TiO₂ (320) substrate in a UHV chamber

3.2 Optical Setup

3.2.1 Linear optical experimental setup

3.2.2 Nonlinear optical system for azimuthal angle dependent

SHG experiment

3.2.3 Advantage of SHG spectroscopic measurement

References

Experimental Procedure

In this chapter I will discuss the sample preparation through the chemical and physical treatment of the TiO₂ (320) substrate and the Au deposition on the surface of the substrate by shadow deposition method in a vacuum chamber. I will also discuss the detail experimental setup for SHG and linear optical measurement of the Au/TiO₂ (320) interface.

3.1 Sample Preparation

A rutile type TiO₂ (320) single crystal cut off from a TiO₂ (110) wafer with 11.3° miscut angle toward the [1 $\bar{1}$ 0] direction and mirror-polished on one side with thickness of 0.5 mm, was purchased from K & R Creation Co., Ltd. Then we conducted the chemical and physical treatment to prepare the TiO₂ (320) substrate for the Au deposition.

3.1.1 Sample cleaning by HF etching

For HF etching, I prepared an aqueous solution of 5% hydrofluoric acid and 95% ultrapure water. The purity of the HF solution was 96% manufactured by Wako Company. For HF etching treatment, the TiO₂ (320) sample was first cleaned with ultrapure water for 1 minute, and then immersed in a 5% HF aqueous solution for 10 minutes with gentle rocking. After treatment, it was cleaned again with ultrapure water and dried the surface with N₂ gas blower. This etching treatment has been conducted in a Class 1000 clean room. The main purpose of the HF etching treatment is to remove the surface impurities such as oil, grease or some carbon species, which may attach on the surface during mechanical polishing or machining. After the etching treatment, the next step is

annealing of TiO_2 (320) surface which we are going to discuss in the next content as a part of the sample preparation.

3.1.2 Annealing of TiO_2 (320) substrate

Next we conducted the annealing of the TiO_2 (320) substrate in order to remove the oxygen vacancies. For annealing, we used an electric muffle furnace. First, we placed the TiO_2 (320) substrate in such a way so that the mirror-polished side facing upward on a boat made of alumina, and then we placed the boat into an alumina tube as shown in Figs. 3.1.2.1 (a) and (b). After that, the whole tube was inserted into an electric muffle furnace (FUW 210 PA manufactured by ADVANTEC Co., Ltd.) as shown in Fig. 3.1.2.1 (c). Finally, the air annealing was performed.

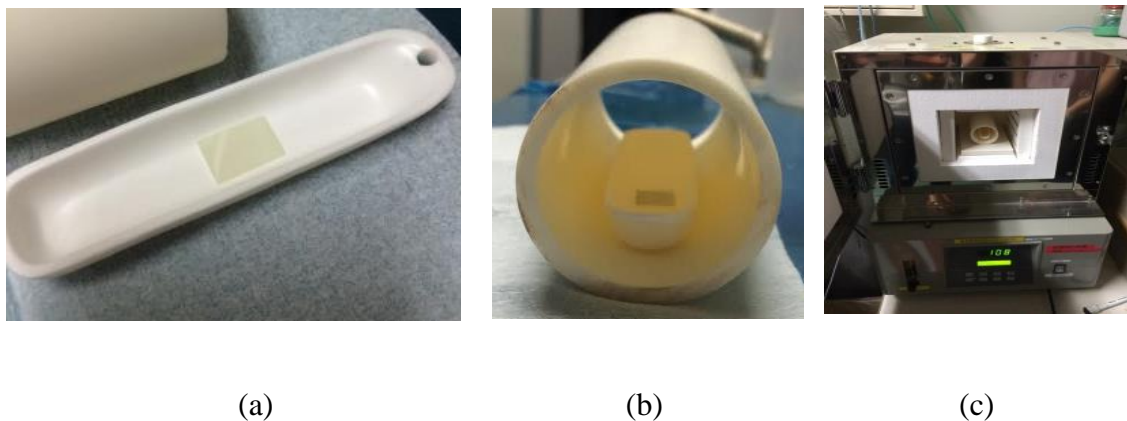


Figure 3.1.2.1 Alumina boat consisting of the TiO_2 (320) sample (a), alumina tube for carrying the boat with the sample (b), and an electric muffle furnace containing the alumina tube along with the TiO_2 (320) sample (c).

In order to anneal the TiO_2 (320) substrate, a specific pattern was followed as shown in Fig. 3.1.2.2. This pattern was pre-settled as a program before starting the operation of the electric furnace. The maximum temperature range of this electric muffle furnace is 850°C . I choose 800°C

as maximum temperature considering the safety for our annealing operation. The annealing operation was divided in to five segments. First, the temperature was allowed to increase up to 300°C in 3 hours, then up to 800°C in the next 20 hours. After that, the sample was kept at 800°C for 2 hours and then allowed to cool down to 300°C in next 20 hours. Finally, the temperature fall down to the room temperature in 3 hours. The annealing operation time was settled 48 hours in total.

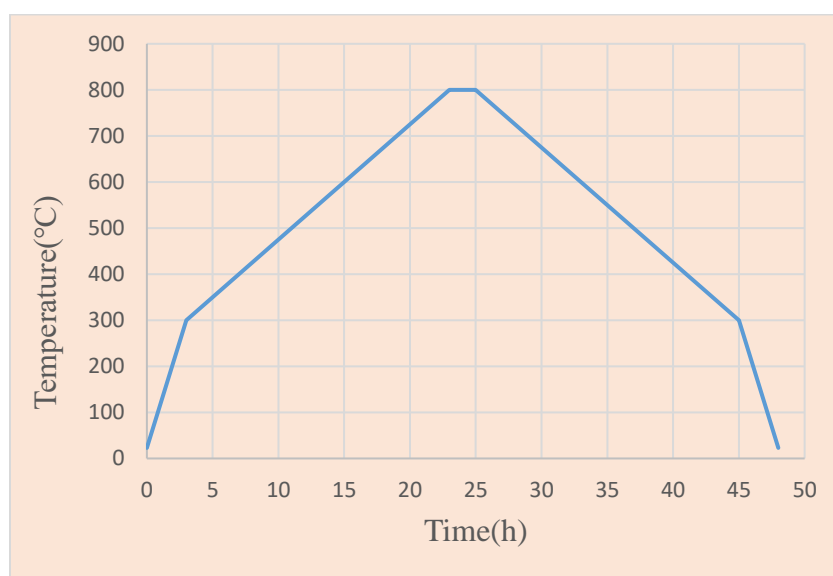


Figure 3.1.2.2. The annealing pattern of TiO₂ (320) substrate in air. The maximum time and temperature of the annealing operation was settled 48 hours and 800°C, respectively.

The main purpose of the annealing operation was to remove the bulk oxygen vacancies from the TiO₂ (320) substrate and to make more regulated surface of the substrate. Takahashi studied the surface structure of an annealed and without annealed samples after HF etching by the AFM measurement [1]. The periodic step structure with step bunching was observed from the annealed sample, whereas no periodic steps or step bunching appeared from the sample without annealing. A flat surface structure was observed from the sample that is not annealed and this

flatness was created due to polishing with diamond abrasive grains and mechanochemical treatment [1]. For this reason, annealing is a very important process in order to obtain a more regulated surface structure. I conducted air annealing although there was an opportunity to do annealing in presence of oxygen or nitrogen gas. However, the previous researchers of our group observed that there is no significant difference between the air annealing and other gas annealing such as oxygen considering the properties of annealed surface. This is because the air contains a huge amount of oxygen gas.

3.1.3 Au deposition on the TiO₂ (320) substrate in a vacuum chamber

In order to deposit the Au film on the TiO₂ (320) substrate in a vacuum chamber, I must clean the sample before inserting it into the UHV chamber. I cleaned the sample in an ultrasonic bath by using ultrapure water, acetone and ethanol and again by ultrapure water consecutively for 10 minutes of each chemical treatment. Then for the Au deposition on the TiO₂ (320) substrate I continued to follow the steps discussed below.

Install the sample on the sample holder

For Au deposition, I introduced the sample on a sample holder and attached it by a spacer with two screw as shown in Fig. 3.1.3.1.



Figure 3.1.3.1. Introduce the TiO₂ (320) sample on a sample holder.

Then the sample holder along with the sample was inserted into the vacuum chamber manually by opening the 152 CF flange. Figs. 3.1.3.2 and 3.1.3.3 shows the 152 CF flange that was manually opened to insert the sample holder into the chamber.



Figure 3.1.3.2. The 152 CF flange that was manually opened to insert the sample holder into the UHV chamber



Figure 3.1.3.3. The sample holder position inside the UHV chamber.

Then I screw up to close the flange and start the chamber. The required vacuum pressure for the Au deposition was approximately 10^{-7} Torr. So, I waited for 4-6 days to meet the required vacuum condition for the deposition.

Preparation for Au deposition

The Au deposition on the TiO₂ (320) substrate was conducted by following the steps given below.

- i) First, I ensured the water supply running around outside the wall of the chamber to reduce the generation of high temperature that can damage the chamber.
- ii) After that, I installed the Au source cable and clips to the chamber as shown in Fig. 3.1.3.4.
- iii) Then the thickness monitor cable was connected with the chamber to monitor the deposited film thickness and started the deposition controller (INFICON- XTC/2).
- iv) The Au deposition parameters were fixed such as density=19.30 g/cm³ and Z-ratio=0.381.
- v) After that, the voltage was raised slowly and the inside current and temperature were automatically increased along with the voltage. The voltage control zone is shown by the following Fig. 3.1.3.5.
- vi) During the operation, I increased the voltage slowly until the temperature up to 850°C for Au deposition. The temperature is measured by a thermocouple attached to the crucible.
- vii) I kept the shutter of Au source closed until 850°C.
- viii) Before opening the shutter, I placed the thickness monitor just below the TiO₂ (320) substrate in order to control the exact film thickness by the measurement of deposition rate.

- ix) After that, I kept exposed the surface of the TiO₂ (320) substrate to deposit Au until the achievement of desired thickness of the film.
- x) I approximately deposited 2 nm thickness of Au film on the TiO₂ (320) substrate with a deposition rate of 0.1 nm/minute.
- xi) After the completion of the deposition of the Au film, I closed the shutter immediately and reduced the voltage slowly until it becomes zero.
- xii) After that, the deposition controller, the voltage and current controller were switched off and I disconnected the Au source cable and the thickness monitor cable.
- xiii) Finally, the water supply was stopped after the temperature of the chamber reached below 100°C temperature.

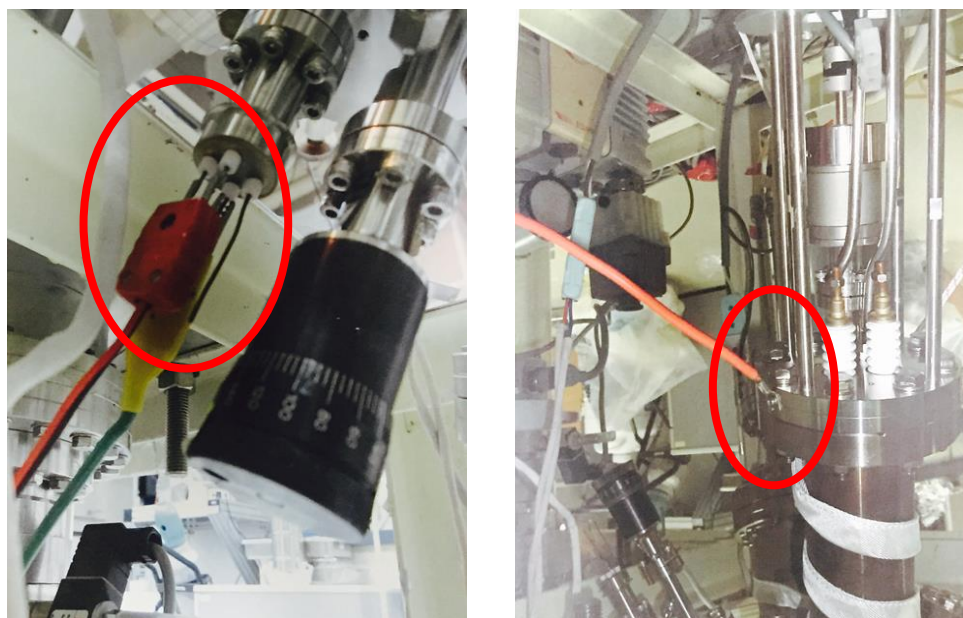


Figure 3.1.3.4. Installation of Au source cable and clip and ground connection to the chamber.

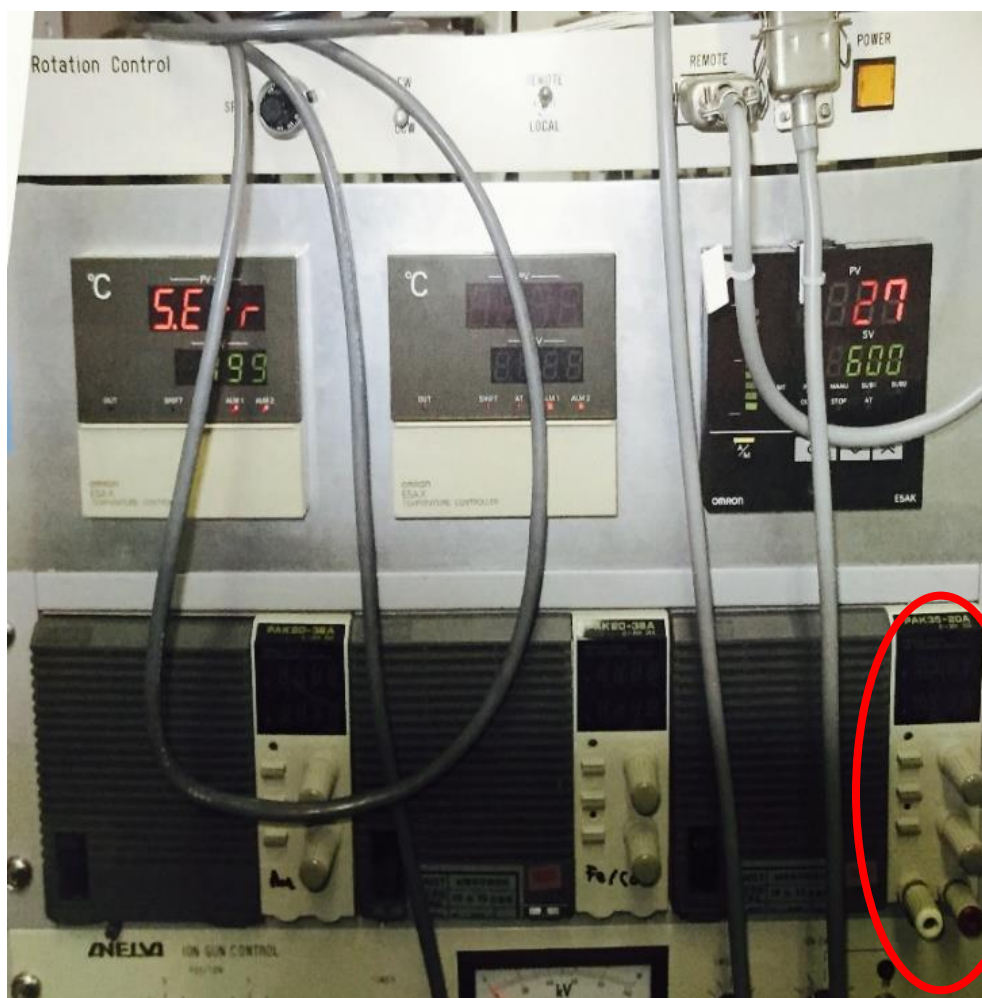


Figure 3.1.3.5. Voltage control zone.

Taking out the Au deposited sample from the chamber

After the Au deposition on the TiO_2 (320) substrate, we took out the sample from the chamber after few days. I opened the 152 CF flange in order to take out the sample manually. After the collection of the Au deposited sample, the sample holder was returned into the chamber and closed the flange. After that, I started pumping the chamber and waited for few days in order to meet the desirable vacuum condition.

3.2 Optical Setup

Now I will describe the optical setup for linear and nonlinear experiment. I will also discuss about the advantage of second harmonic generation (SHG) method.

3.2.1 Linear optical experimental setup

The linear reflectivity spectrum was measured as a function of the wavelength ranging from 250 nm to 1100 nm by a spectrometer equipped with a polarizer accessory, a Xe lamp source, and two photodiode detectors. These two photodiode detectors acted as a reference and main detectors and recorded spectra was the ratio of the output of these two detectors. The two lock-in amplifiers were used to amplify the signals that were obtained from those detectors. During the measurement, the sample was placed at an incident angle of 45° with respect to the surface normal for the reflectivity. The final data were recorded in a computer which is connected with the linear optical setup. I measured the reflectivity spectra from the Au/TiO₂ (320) sample for 0° , 90° , 180° and 270° position with respect to the azimuthal angle at the horizontal and vertical polarization configuration. The linear optical setup is shown in the following Fig. 3.2.1.1.

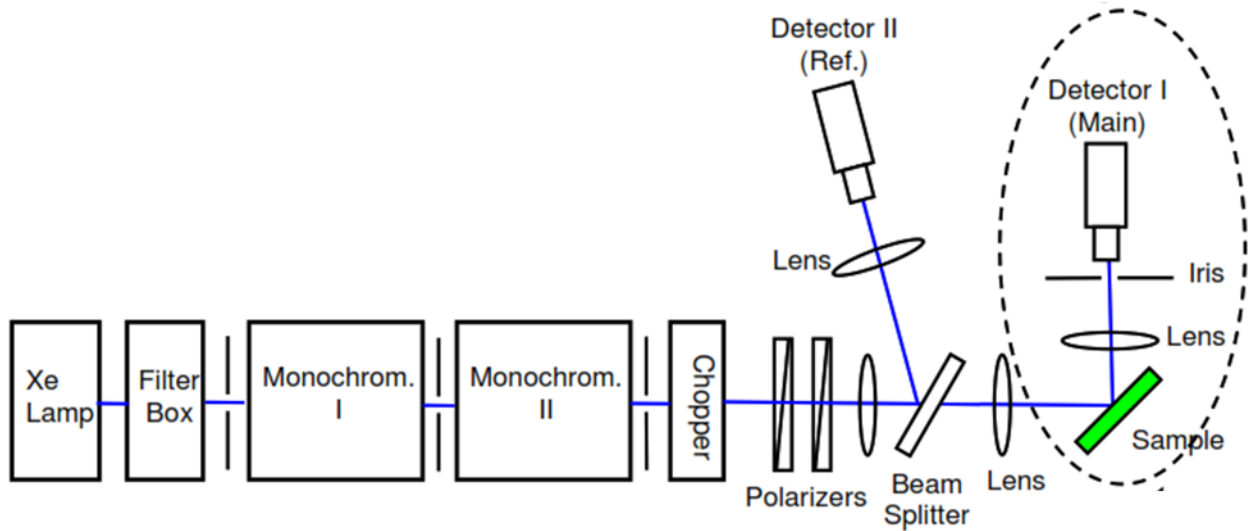


Figure 3.2.1.1. Linear optical setup for the measurement of reflectivity spectra.

3.2.2 Nonlinear optical system for azimuthal angle dependent SHG Experiment

In this part, I will describe the nonlinear optical setup for second harmonic generation (SHG) measurement as a function of azimuthal angle and different input and output polarization combinations. The detailed optical setup for the SHG measurement is shown in Fig. 3.2.2.1. As the excitation source of SHG, a mode-locked Nd^{3+} :YAG picosecond pulsed laser was used. The output pulse width and the repetition rate were 30 picosecond and 10Hz, respectively. For the azimuthal angle and polarization dependent SHG measurement, the sample was mounted on an automatic rotation stage and was rotated around its surface normal. The incident polarized light at the photon energy of 1.17 eV or 2.33 eV corresponding to 1064 nm or 532 nm wavelength, respectively, illuminated the Au deposited TiO_2 (320) or bare TiO_2 (320) sample at an incident angle of 45° with respect to the surface normal, after passing through a prism, a mirror, a half-

3.2.3 Advantage of SHG spectroscopic measurement

Second harmonic generation (SHG) involved in the conversion of the two photons of the same frequency ω into a single photon of frequency 2ω and half wavelength of the incident probe [4]. The energy level diagram for SHG process is shown in the following Figs. 3.2.3.1.

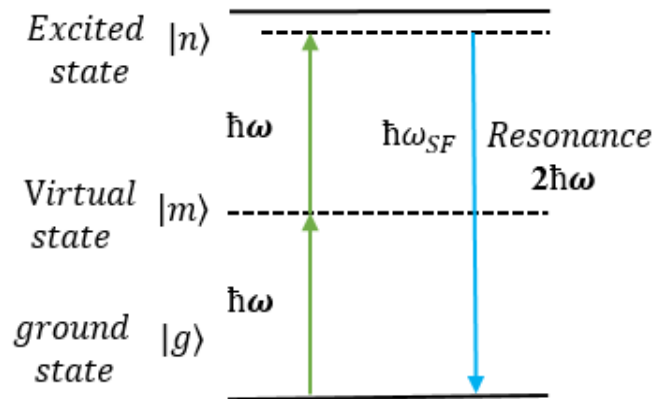


Figure 3.2.3.1. Energy level diagram of second harmonic generation (SHG) process.

It is well established that SHG is very sensitive to the surface and interface for centrosymmetric media with submonolayer sensitivity. Particularly, the SHG technique exhibits very high surface specificity [5]. According to the selection rule of SHG, it is only allowed from the surface or interface where the symmetry is broken or having no inversion symmetry. On the contrary, the SHG is forbidden in the bulk of medium having inversion symmetry [5]. It is obvious that, the breaking of symmetry occurs automatically at junctions between two different materials due to the strong materials gradient, although they are centrosymmetric in nature individually. The other attractive features of SHG are that the SHG is non-invasive and contactless technique that can be applied “in situ” and in “real-time” application with a good time resolution [6]. These outstanding characteristics make the SHG more promising diagnostic to study the surface, interface and thin

film [6]. One of the key quantity, second-order nonlinear susceptibility tensor that is directly related to the macroscopic structure of the materials can be determined accurately using SHG technique [7]. One can deduce atomic level information such as electronic structure, molecular orientation from the precise determination of the susceptibility tensor [7]. As the SHG is a surface specific technique, it is a powerful tool to extract the electronic level information from the interface of Au/TiO₂ since the symmetry is broken.

References

- [1] H. Takahashi, Doctoral Thesis, Japan Advanced Institute of Science and Technology, School of Materials Science (2012).
- [2] H. Takahashi, R. Watanabe and G. Mizutani; Surf. Interface Anal. 42, 1659-1662, 2010.
- [3] Ekspla Optical Parametric Generator PG401VIR/SH, Technical Description and User's Manual. 4-2 and 4-3; Vilnius 2000.
- [4] R. M. Corn and D. A. Higgins, Chem. Rev., 94, 107-125, 1994.
- [5] L. Marrucci, D. Paparo, G. Cerrone, C. de Lisio, E. Santamato, S. Solimeno, S. Ardizzone and P. Quagliotto; Optics and Lasers in Engineering, 37, 601-610, 2002.
- [6] J. J. H. Gielis, P. M. Gevers, I. M. P. Aarts, M. C. M. Van de Sanden and W. M. M. Kessels; J. Vac. Technol. A 26, 6, 2008.
- [7] S. Cattaneo, E. Vuorimaa, H. Lemmetyinen and M. Kauranen; J. Chem. Phys. Vol. 120, No. 19, 2004.

Chapter 4: Results and Discussion

4.1 Morphological study of Au/TiO₂ (320) interface by AFM and SEM with EDX

4.2 SHG intensity measurement as a function of azimuthal angle and polarization

4.2.1 Experimental results

4.2.2 Theoretical investigation of the origin of rotational anisotropic response

4.3 Summary of this chapter

References

Results and Discussion

In this chapter, I would like to discuss the experimental results in detail and briefly discuss them including the morphological study by AFM and SEM with EDX. I will also discuss the SHG results and the origin of the anisotropic SHG response that includes the tensorial analysis of specific contribution of step and terrace of Au/TiO₂ (320) interface in order to determine the electronic states. I will also discuss the results of linear measurement such as linear optical reflectivity with their influence on the anisotropic SHG response.

4.1 Morphological study of the Au/TiO₂ (320) interface by AFM and SEM with EDX

I studied the surface structure of bare TiO₂ (320) single crystal after annealing by AFM. Fig. 4.1.1 (a) show some stripe patterns and does not show regulated steps. Indeed, the steps are random on the bare TiO₂ (320) surface. So, it is difficult to figure out the actual terrace length. Even if the steps were found random on the surface, the main purpose of this research was not distracted. The separation of the step and terrace contribution was successfully done in this research. In our published article [1], the AFM image of bare TiO₂ (320) surface and its interpretation should be replaced to one of this thesis. In addition, I could not observe the step bunching on the surface may be due to the insufficient annealing temperature or time. Therefore, the adatoms could not disperse by the supplied energy during the heat treatment operation.

Then I deposited 2 nm Au thin film on the bare TiO₂ (320) single crystal and checked the surface structure by using AFM. From this observation, island structures were observed on the

Au surface with the maximum length and height of the islands about 400 nm and 200 nm, respectively, as shown in Fig. 4.1.1 (b). Therefore, the deposited thin Au film on the bare TiO_2 (320) surface is not uniform and smooth. The Au nanoparticles are randomly distributed on the surface of TiO_2 (320) single crystal.

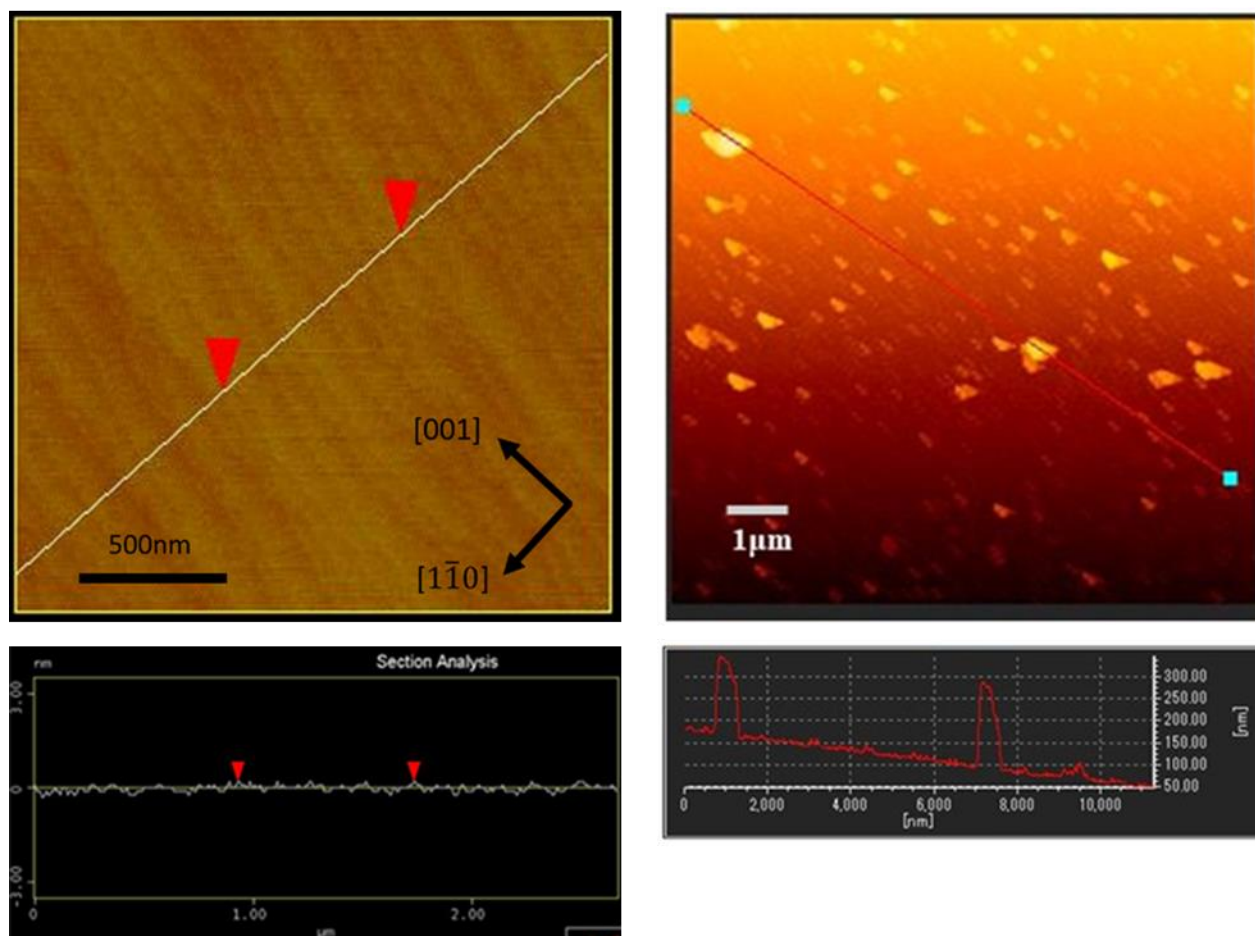


Figure 4.1.1. AFM image and profile of (a) bare TiO_2 (320) single crystal and (b) Au/TiO_2 (320) sample.

In order to confirm the distribution of Au on the surface of bare TiO₂ (320), I used SEM with EDX. SEM image of Au deposited TiO₂ (320) surface is shown in Fig. 4.1.2. From this image, it is clearly shown that the film of Au is very smooth in some places and also has some island structures in other places on the surface. Probably the bright spot on the SEM image is an island structure of Au nanoparticles. I observed the EDX spectrum from the two different areas on the Au deposited TiO₂ (320) surface. Figs. 4.1.3, 4.1.4 and 4.1.5 show the EDX spectra of the average surface area including both bright and smooth film area, bright area (pointed spectrum 18) and smooth film area (pointed spectrum 19), respectively, as shown in the SEM image (Fig. 4.1.2). Fig. 4.1.3 represents the EDX analysis of average atomic percentage of different elements existing on the scanned area in Fig. 4.1.3. The average atomic percentage of Au was found as 0.13%. Figs. 4.1.4 and 4.1.5 show that the atomic percentage of Au were found as 0.23% and 0.15% from the bright area and smooth film area, respectively. The atomic percentage of Au was found higher from the bright area compared to the other smooth area. Therefore, there are some island structure of Au nanoparticles on the surface and it is consistent to the AFM observation. Considering the 2.5 μm area on the AFM image and SEM image shown in the Figs. 4.1.1 (a), (b) and 4.1.3, respectively, the number of Au islands were clearly visible on the AFM image while they were not clear on the SEM image. As I mentioned above, according to the SEM image only one bright area was observed and I consider it as an island structure due to higher atomic percentage of Au nanoparticles compared to the other scanned area. This happened may be due to the difference of spatial resolution between the AFM and SEM machine that I used to analyse this surface. The spatial resolution of SEM and AFM were approximately 100 nm and several nanometers, respectively.

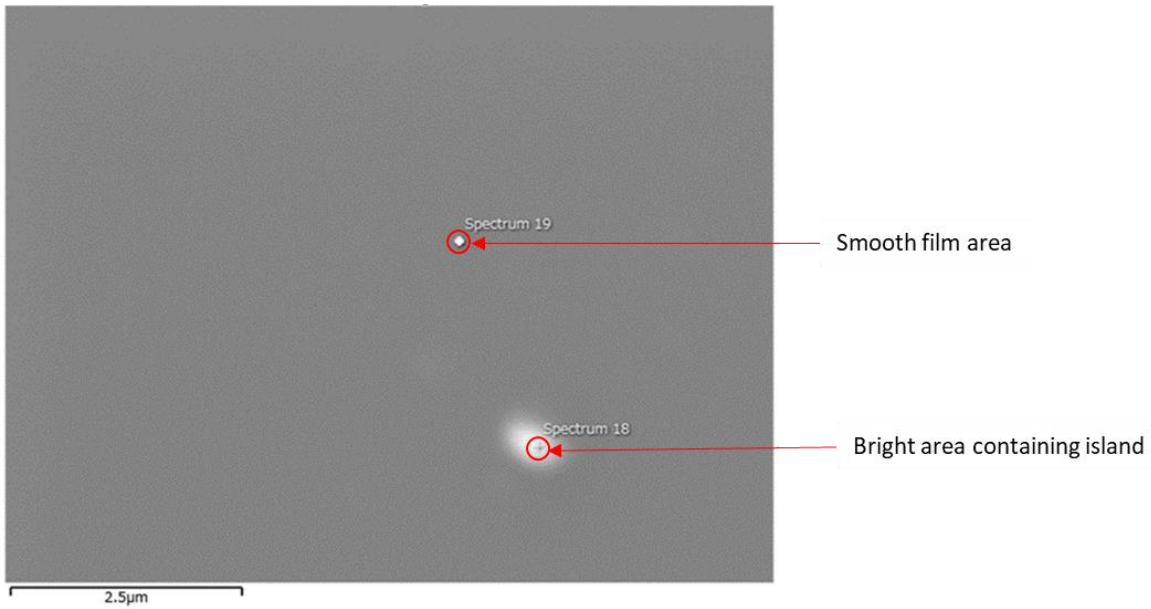


Figure 4.1.2. SEM image of Au deposited TiO₂ (320) surface.

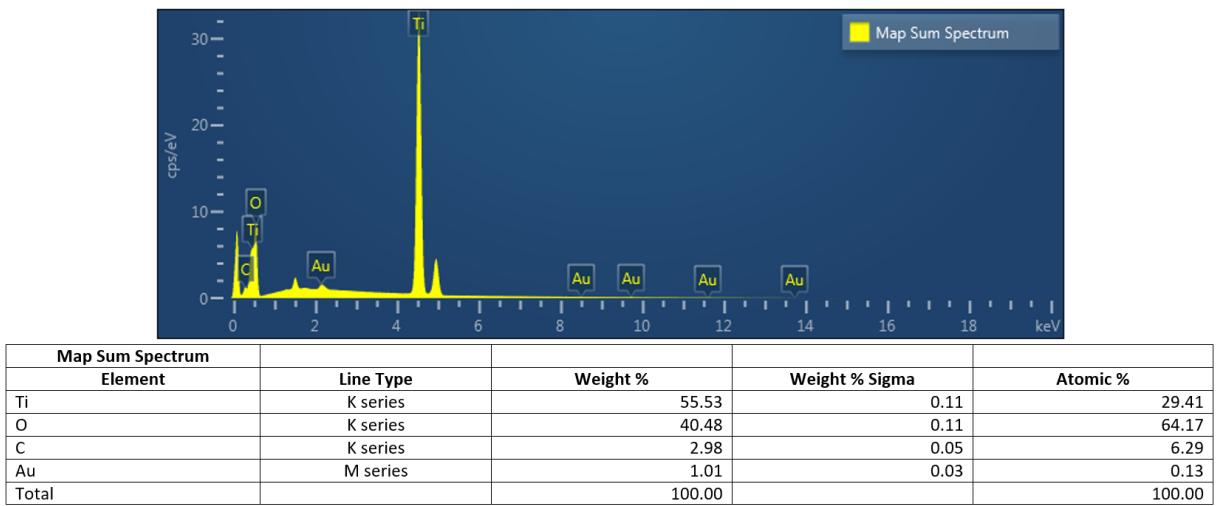
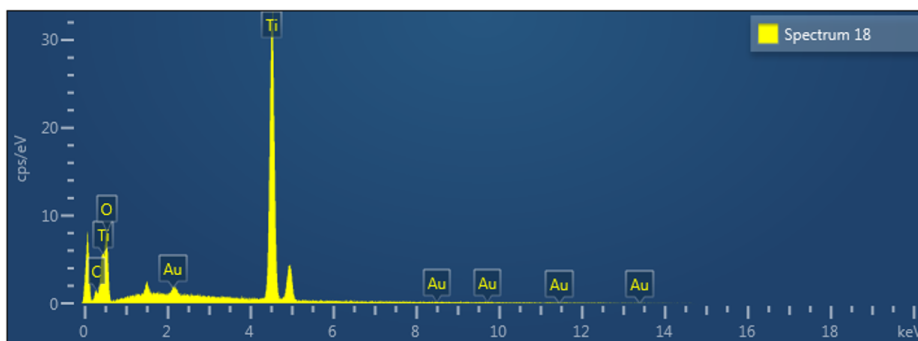
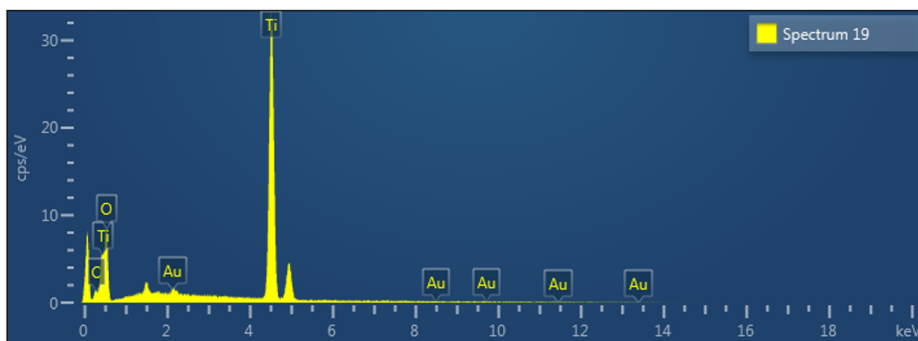


Figure 4.1.3. Sum EDX spectrum of different elements existing on the surface of Au/TiO₂ (320).



Spectrum 18				
Element	Line Type	Weight %	Weight % Sigma	Atomic %
Ti	K series	55.42	0.68	29.56
O	K series	39.41	0.71	62.94
C	K series	3.42	0.34	7.28
Au	M series	1.74	0.22	0.23
Total		100.00		100.00

Figure 4.1.4. EDX spectrum of different elements obtained from an island of Au existing on the surface of bare TiO₂ (320).



Spectrum 19				
Element	Line Type	Weight %	Weight % Sigma	Atomic %
Ti	K series	55.13	0.67	29.08
O	K series	40.40	0.69	63.80
C	K series	3.32	0.33	6.97
Au	M series	1.15	0.21	0.15
Total		100.00		100.00

Figure 4.1.5. EDX spectrum of different elements obtained from a smooth area of Au film existing on the surface of bare TiO₂ (320).

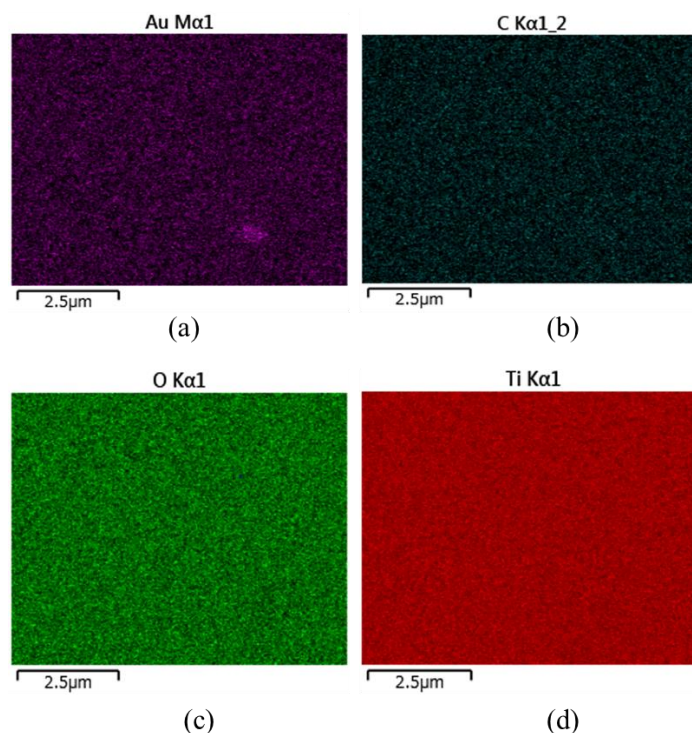


Figure 4.1.6. EDX mapping on the same SEM image shown in Fig. 4.1.2. for individual elemental distribution on the Au deposited bare TiO_2 (320) surface. (a) Au distribution, (b) carbon distribution, (c) oxygen distribution, and (d) titanium distribution.

Figure 4.1.6 exhibits the EDX mapping on the SEM image (shown in Fig. 4.1.2) for the observation of individual elemental distribution on the Au deposited TiO_2 (320) surface. Fig. 4.1.6 (a), (b), (c) and (d) correspond to the distribution of Au, C, O and Ti, respectively. Fig. 4.1.6 (a) shows that the Au nanoparticles are distributed on the whole surface of the bare TiO_2 (320). A bright spot is also visible on the Au distribution map and there the atomic percentage of Au is higher than the other smooth film area on the surface and probably it is the island of Au clearly seen in Fig. 4.1.2. From Fig. 4.1.6 (b), (c) and (d), it is shown that other elements such as Ti, O and C are almost uniformly distributed on the Au deposited TiO_2 (320) surface. The same evidence

was also found from the value of atomic percentage of different elements existing on the surface shown in the Figs. 4.1.3, 4.1.4 and 4.1.5.

In order to remove the ambiguity regarding the detection limit of Au nanoparticle deposited on the TiO₂ (320) by using EDX shown in Figs. 4.1.3, 4.1.4 and 4.1.5, I checked the SEM image along with EDX spectrum of bare TiO₂ (320) by using the same machine and operated at the same condition. The EDX spectrum is shown by the following Fig. 4.1.7. According to the EDX spectrum, I could not observe the Au peak and the atomic percentage of Au is 0.00%. Therefore, this observations are helpful to remove the ambiguity regarding the detection limit of Au nanoparticle deposited on the TiO₂ (320) surface.

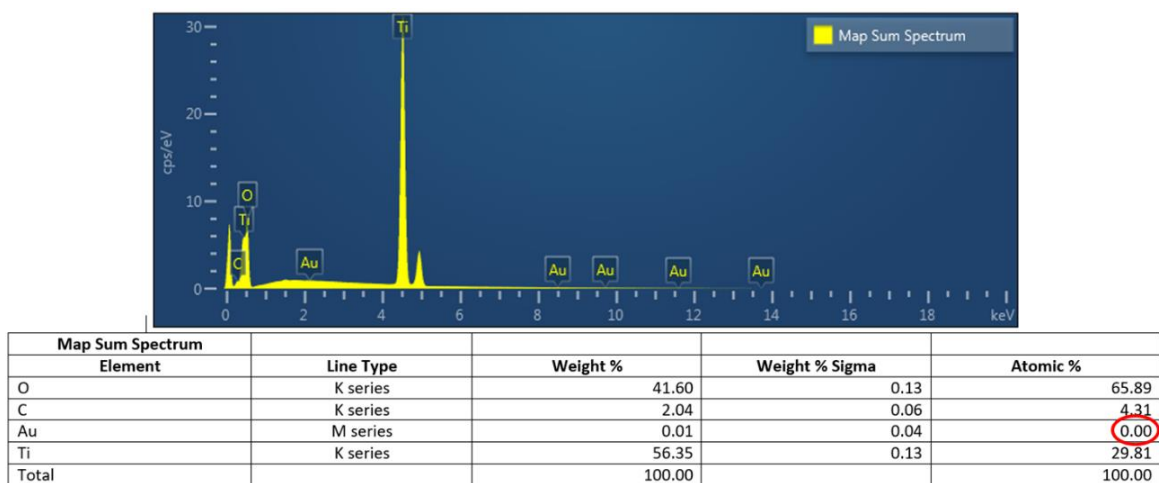


Figure 4.1.7. EDX spectra of different elements existing on the surface of bare TiO₂ (320).

From these microscopic observations, it can be concluded that gold nanoparticles which are embedded in a thin continuous gold film covering the entire surface of the TiO₂ (320) single crystal including the steps. Therefore, I observed the SHG signal from both the island structure and the other smooth areas covered by gold.

4.2 SHG intensity measurement as a function of azimuthal angle and different polarization

The study of electronic states of the Au/TiO₂ interface is very important for the development of the catalyst field. I have fabricated an Au thin film with the thickness of 2 nm on the TiO₂ (320) substrate in a vacuum chamber at the pressure of 2×10^{-7} Torr and observed the second harmonic response from the Au/TiO₂ (320) interface and bare TiO₂ (320) as a function of the rotation angle rotated around the surface normal (azimuthal angle) and different types of polarization combinations. There are four polarization combinations adopted during the experiment such as Pin/Pout, Pin/Sout, Sin/Pout and Sin/Sout. The Pin or Sin indicates the input polarization state and Pout or Sout indicates the output polarization state. I used the incident photon energies of 1.17 eV and 2.33 eV of the pulsed Nd²⁺:YAG laser in order to observe the SHG response from the both samples.

4.2.1 Experimental results

Before starting the discussion about my experimental results, I would like to define the azimuthal angle $\varphi = 0^\circ$ of the bare TiO₂ (320) single crystal in order to clarify the exact crystallographic direction. I can define the azimuthal angle of $\varphi = 0^\circ$ by the following schematic diagram of the TiO₂ (320) sample which is shown in Fig. 4.2.1.1. The azimuthal angle φ is the angle between X and the axis 1. The angle φ equals to zero when X and the axis 1 are on the same direction. In other words, the azimuthal angle φ is defined as the rotation angle around the surface normal of the sample. The zero degree of φ corresponds to the configuration when the plane of

incidence includes the $[\bar{2}30]$ direction. The mirror plane of the surface structure is the 2-3 plane. In a more specific way, direction 2 is parallel to surface that lies in the mirror plane of TiO_2 and perpendicular to the step edges where the symmetry is broken and direction 3 is perpendicular to the surface of the stepped TiO_2 sample. At $\varphi = 0^\circ$, direction 2 corresponds to the step up direction and it is the same direction with laboratory coordinate Y.

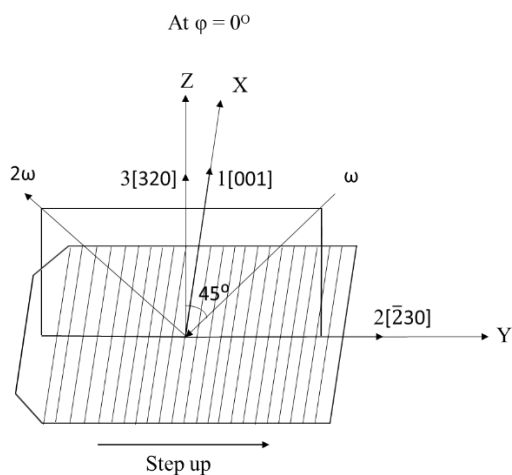


Figure 4.2.1.1. Schematic diagram of the stepped TiO_2 (320) substrate with the incidence plane. Here the coordinate symbols are (X,Y,Z)=Laboratory Coordinates and (1,2,3) \equiv Sample Coordinate. The sample coordinates are indicated by 1[001], 2 $[\bar{2}30]$ and 3[320] directions.

Now I will discuss the azimuthal angle dependent SHG intensity patterns with four different input and output polarization combinations such as Pin/Pout, Pin/Sout, Sin/Pout and Sin/Sout from the Au/ TiO_2 (320) interface and the bare TiO_2 (320) surface with the incident photon energy 1.17 eV shown in the following Figs. 4.2.1.2 and 4.2.1.3, respectively. The red and black dots are representing the experimental and calculated data, respectively. The results are rather isotropic in nature for both the samples by the excitation of 1.17 eV photon energy.

I also measured the SHG response of the same samples at the incident photon energy of 2.33 eV. Fig. 4.2.1.4 and 4.2.1.5 show the azimuthal angle dependent SHG intensity patterns with four different input and output polarization combinations such as Pin/Pout, Pin/Sout, Sin/Pout and Sin/Sout from the Au/TiO₂ (320) interface and the bare TiO₂ (320) surface. The red and black dots are representing the experimental and calculated data, respectively. I found anisotropic response from both the samples when I used the photon energy of 2.33 eV as excitation.

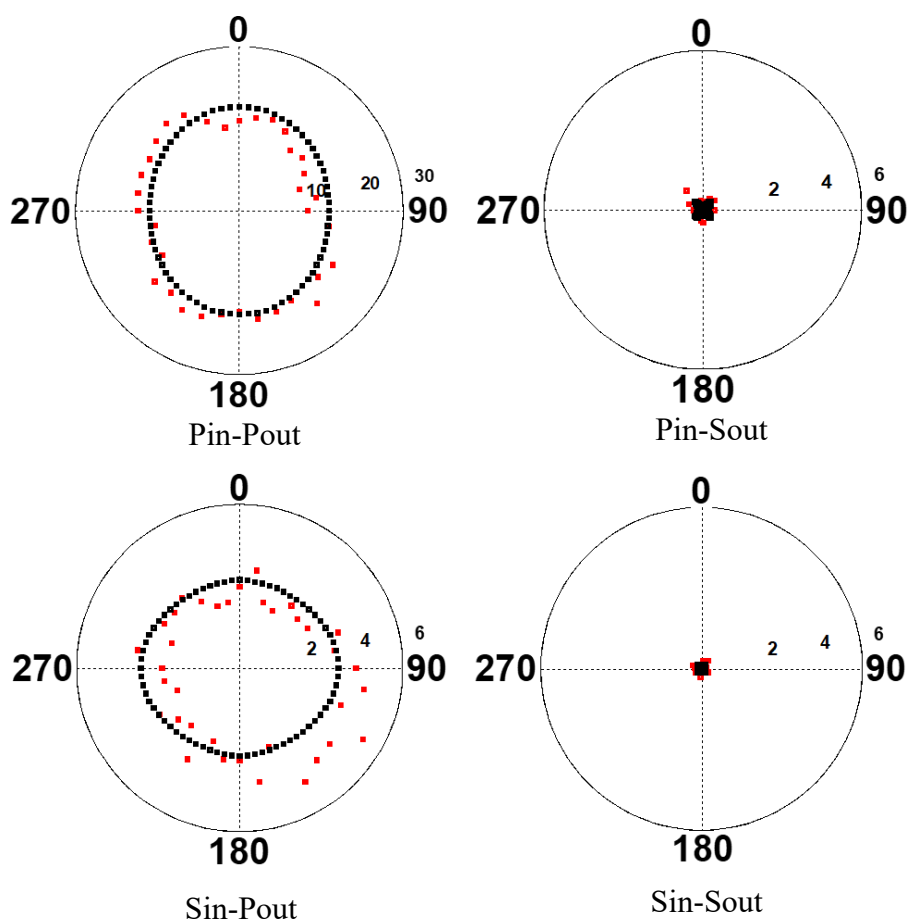


Figure 4.2.1.2. SHG intensity patterns as a function of the azimuthal angle ϕ for the four different input and output polarization combinations from the Au/TiO₂ (320) interface with excitation photon energy $\hbar\omega=1.17\text{eV}$. The SHG intensity was plotted in the radial direction in an arbitrary

but common unit. The input and the output polarizations were shown at the bottom, such as Pin/Sout for P-polarized input and S-polarized output. The incidence angle was set at 45° . The red and black dots represent the experimental and calculated data, respectively.

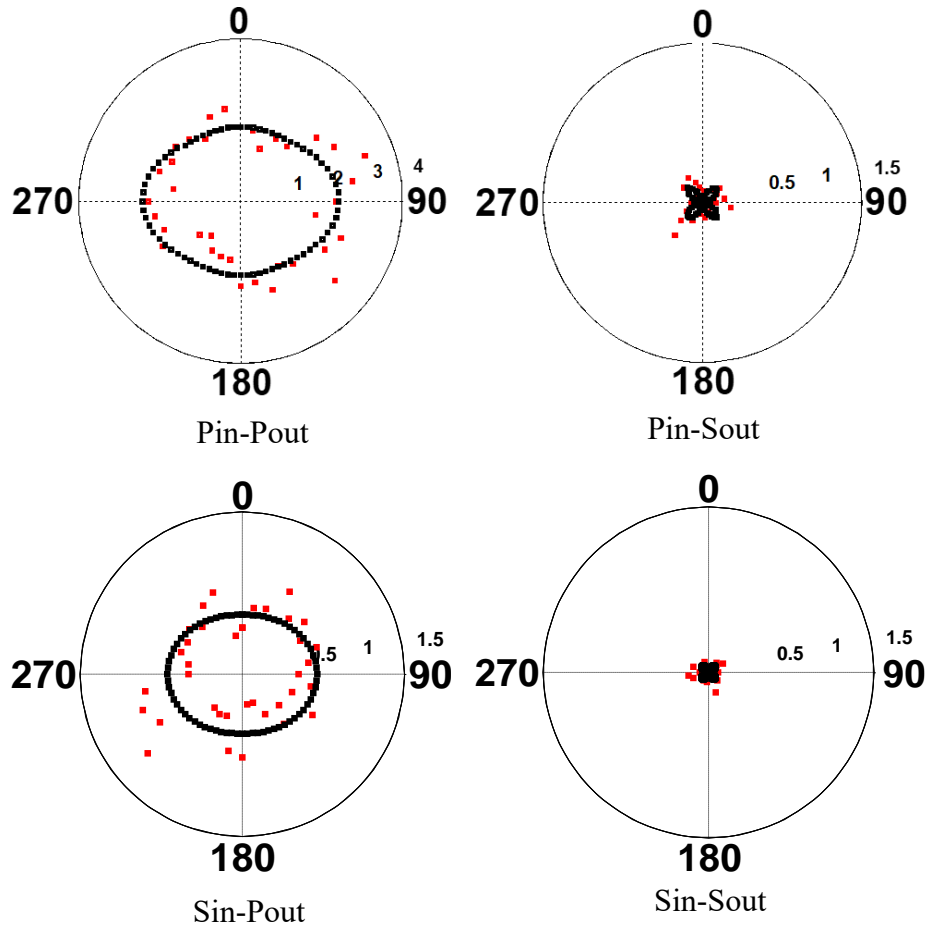


Figure 4.2.1.3. SHG intensity patterns as a function of the azimuthal angle ϕ for the four different input and output polarization combinations from the bare TiO_2 (320) surface with excitation photon energy $\hbar\omega=1.17\text{eV}$. The SHG intensity was plotted in the radial direction in an arbitrary but common unit. The input and the output polarizations were shown at the bottom, such as Pin/Sout for P-polarized input and S-polarized output. The incidence angle was set at 45° . The red and black dots represent the experimental and calculated data, respectively.

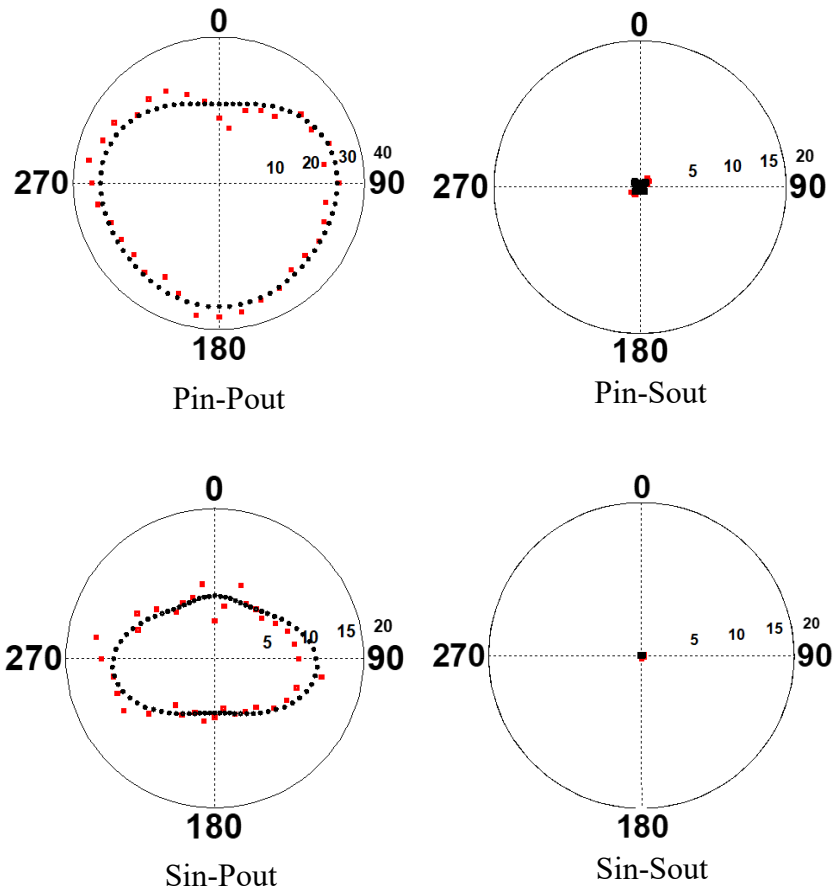


Figure 4.2.1.4. SHG intensity patterns as a function of the azimuthal angle ϕ for the four different input and output polarization combinations from the Au/TiO₂ (320) interface with excitation photon energy $\hbar\omega=2.33\text{eV}$. The SHG intensity was plotted in the radial direction in an arbitrary but common unit. The input and the output polarizations were shown at the bottom, such as Pin/Sout for P-polarized input and S-polarized output. The incidence angle was set at 45° . The red and black dots represent the experimental and calculated data, respectively.

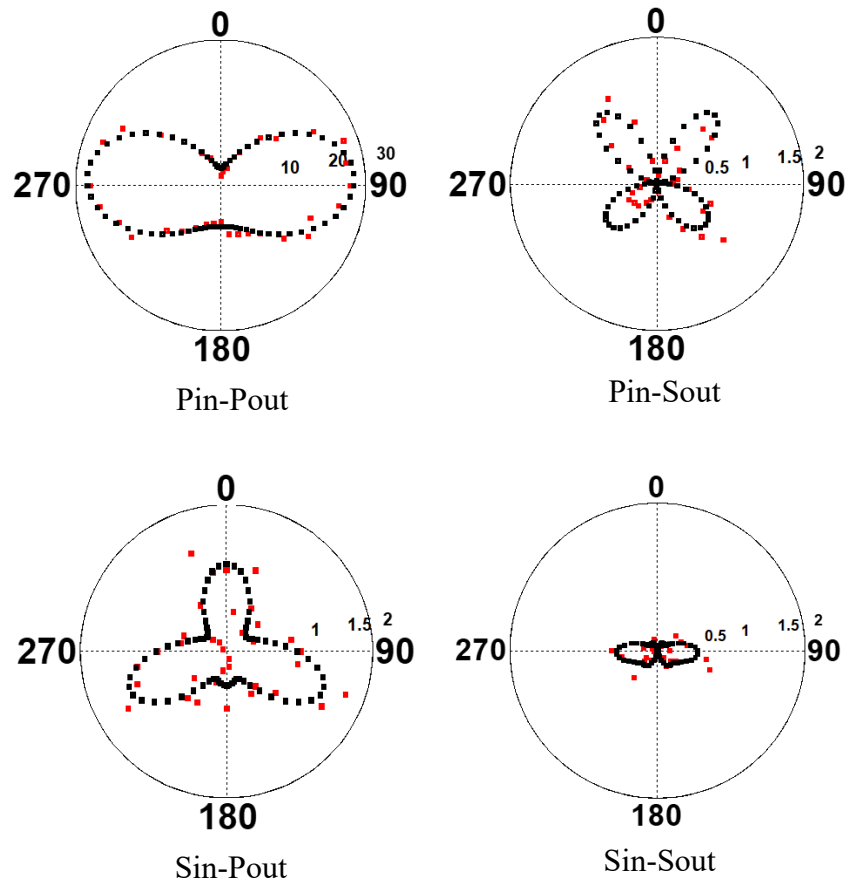


Figure 4.2.1.5. SHG intensity patterns as a function of the azimuthal angle ϕ for the four different input and output polarization combinations from the bare TiO_2 (320) surface with excitation photon energy $\hbar\omega=2.33$ eV. The SHG intensity was plotted in the radial direction in an arbitrary but common unit. The input and the output polarizations were shown at the bottom, such as Pin/Sout for P-polarized input and S-polarized output. The incidence angle was set at 45° . The red and black dots represent the experimental and calculated data, respectively.

4.2.2 Theoretical investigation of the origin of rotational anisotropic response

In general, when the energy of two photons excitation is larger than the band gap of TiO₂ an electronic resonance will be observed. In Figs. 4.2.1.2 and 4.2.1.3, the two photon energy of 2.34 eV of 1064 nm excitation is smaller than the bandgap of TiO₂ (3.1eV) so that the electronic resonance did not occur. This is the reason for the isotropic SHG response from both Au/TiO₂ (320) and bare TiO₂ (320) samples. In Figs. 4.2.1.4 and 4.2.1.5, the two photon energy of 4.66 eV of 532 nm excitation is larger than the bandgap of TiO₂ and hence the anisotropic responses were observed. After getting the experimental SHG intensity patterns, I theoretically drew the fitting patterns by using a least square fitting algorithm. I conducted the phenomenological analysis of the SHG intensity patterns using nonlinear optical susceptibility [2].

In order to study the origin of the anisotropic SHG response from both Au/TiO₂ (320) and bare TiO₂ (320) samples, we considered to study their symmetric properties particularly the dominant nonlinear optical susceptibility ($\chi_{ijk}^{(2)}$) elements. The $\chi_{ijk}^{(2)}$ is a second rank tensor describing the second-order nonlinear optical susceptibility elements and it includes 27 elements. The inherent property of the material decides the symmetry and therefore the number of $\chi_{ijk}^{(2)}$ elements [2]. For the particular metallic nanostructures, we can estimate the surface symmetry based on their shape and greatly reduce the number of $\chi_{ijk}^{(2)}$ elements. It is well known that, Au/TiO₂ (320) and bare TiO₂ (320) samples have *Cs* symmetry system.

For centrosymmetric media, at least the two opposite directions should be the same and therefore, the value of $\chi_{ijk}^{(2)}$ for two opposing directions should be the same as, [3].

$$\chi_{ijk}^{(2)} = \chi_{-i-j-k}^{(2)} \text{-----(1)}$$

Furthermore, from the physical point of view, as the coordinates are reversed, the physical phenomenon must also change the sign or,

$$\chi_{ijk}^{(2)} = \chi_{-i-j-k}^{(2)} = -\chi_{i-j-k}^{(2)} = \chi_{ij-k}^{(2)} = -\chi_{ijk}^{(2)} \text{-----(2)}$$

Hence, $\chi_{ijk}^{(2)} = 0$ should hold.

The result shows that SHG is forbidden in the centrosymmetric medium. However, at the surface or interface, the broken symmetry exists and therefore SHG is active. In order to obtain the number of nonlinear susceptibility elements, one can examine the symmetry of the nanostructure material lying on planar surfaces. TiO₂ (320) substrate contains C_s symmetry system. With C_s symmetry, we have “2≠-2” and “3≠-3” but “1=-1”. I can apply the eq. (2) to evaluate the number of nonzero nonlinear susceptibility elements. The result is shown in Table 1.

Table 1. Assignment of the number of $\chi_{ijk}^{(2)}$ element in the case of C _s symmetry.		
$\chi_{ijk}^{(2)}$	Apply to equation (2)	Contribution
$\chi_{222}^{(2)}$	no effect	Yes
$\chi_{221}^{(2)}$	$\chi_{221}^{(2)} = \chi_{22-1}^{(2)} = -\chi_{221}^{(2)}$	No
$\chi_{223}^{(2)}$	no effect	Yes
$\chi_{212}^{(2)}$	$\chi_{212}^{(2)} = \chi_{2-12}^{(2)} = -\chi_{212}^{(2)}$	No
$\chi_{211}^{(2)}$	$\chi_{211}^{(2)} = \chi_{2-1-1}^{(2)} = \chi_{211}^{(2)}$	Yes
$\chi_{213}^{(2)}$	$\chi_{213}^{(2)} = \chi_{2-13}^{(2)} = -\chi_{213}^{(2)}$	No
$\chi_{232}^{(2)}$	no effect	Yes

$\chi_{231}^{(2)}$	$\chi_{231}^{(2)} = \chi_{23-1}^{(2)} = -\chi_{231}^{(2)}$	No
$\chi_{233}^{(2)}$	no effect	Yes
$\chi_{122}^{(2)}$	$\chi_{122}^{(2)} = \chi_{-122}^{(2)} = -\chi_{122}^{(2)}$	No
$\chi_{121}^{(2)}$	$\chi_{121}^{(2)} = \chi_{-12-1}^{(2)} = \chi_{121}^{(2)}$	Yes
$\chi_{123}^{(2)}$	$\chi_{123}^{(2)} = \chi_{-123}^{(2)} = -\chi_{123}^{(2)}$	No
$\chi_{112}^{(2)}$	$\chi_{112}^{(2)} = \chi_{-1-12}^{(2)} = \chi_{112}^{(2)}$	Yes
$\chi_{111}^{(2)}$	$\chi_{111}^{(2)} = \chi_{-1-1-1}^{(2)} = -\chi_{111}^{(2)}$	No
$\chi_{113}^{(2)}$	$\chi_{113}^{(2)} = \chi_{-1-13}^{(2)} = \chi_{113}^{(2)}$	Yes
$\chi_{132}^{(2)}$	$\chi_{132}^{(2)} = \chi_{-132}^{(2)} = -\chi_{132}^{(2)}$	No
$\chi_{131}^{(2)}$	$\chi_{131}^{(2)} = \chi_{-13-1}^{(2)} = \chi_{131}^{(2)}$	Yes
$\chi_{133}^{(2)}$	$\chi_{133}^{(2)} = \chi_{-133}^{(2)} = -\chi_{133}^{(2)}$	No
$\chi_{322}^{(2)}$	no effect	Yes
$\chi_{321}^{(2)}$	$\chi_{321}^{(2)} = \chi_{32-1}^{(2)} = -\chi_{321}^{(2)}$	No
$\chi_{323}^{(2)}$	no effect	Yes
$\chi_{312}^{(2)}$	$\chi_{312}^{(2)} = \chi_{3-12}^{(2)} = -\chi_{312}^{(2)}$	No
$\chi_{311}^{(2)}$	$\chi_{311}^{(2)} = \chi_{3-1-1}^{(2)} = \chi_{311}^{(2)}$	Yes
$\chi_{313}^{(2)}$	$\chi_{313}^{(2)} = \chi_{3-13}^{(2)} = -\chi_{313}^{(2)}$	No
$\chi_{332}^{(2)}$	no effect	Yes
$\chi_{331}^{(2)}$	$\chi_{331}^{(2)} = \chi_{33-1}^{(2)} = -\chi_{331}^{(2)}$	No
$\chi_{333}^{(2)}$	no effect	Yes

Moreover, the intrinsic permutation symmetry of $\chi_{ijk}^{(2)}$ makes the $\chi_{ijk}^{(2)} = \chi_{ikj}^{(2)}$, because the response of the medium cannot “recognize” the mathematical ordering of the fields. Thus we

have ten independent nonlinear susceptibility elements, $\chi_{223}^{(2)} = \chi_{232}^{(2)}$, $\chi_{113}^{(2)} = \chi_{131}^{(2)}$, $\chi_{112}^{(2)} = \chi_{121}^{(2)}$, $\chi_{211}^{(2)}$, $\chi_{222}^{(2)}$, $\chi_{233}^{(2)}$, $\chi_{323}^{(2)} = \chi_{332}^{(2)}$, $\chi_{311}^{(2)}$, $\chi_{322}^{(2)}$, and $\chi_{333}^{(2)}$ considering my symmetry structure. Here, 1, 2, and 3 represent the [001], $[\bar{2}30]$, and [320] directions on the stepped TiO₂ (320) surface, respectively, and their axes are fixed to the sample as shown in Fig. 4.2.1.1. The mirror plane of the surface structure is the 2-3 plane. In the directions 2 and 3 there are broken symmetries caused by the surface steps and the terrace surface, respectively. Hence the nonlinear susceptibility elements $\chi_{121}^{(2)}$, $\chi_{211}^{(2)}$, $\chi_{222}^{(2)}$, $\chi_{233}^{(2)}$, and $\chi_{323}^{(2)}$ with odd number of suffixes 2 originate from the step contribution. The other five susceptibilities $\chi_{113}^{(2)}$, $\chi_{223}^{(2)}$, $\chi_{311}^{(2)}$, $\chi_{322}^{(2)}$, and $\chi_{333}^{(2)}$ with odd numbers of suffixes 3 originate from the terrace contribution. I choose odd number of suffixes 2 as step contribution because they have nonzero contribution when I considered $2 \neq -2$, due to having the broken symmetry at the direction 2 and it originates from the interface of Au/step region of TiO₂ (320). The evaluation of nonzero $\chi_{ijk}^{(2)}$ elements that are responsible for the step contribution are mentioned below:

$$P_i = \epsilon_0 \chi_{ijk}^{(2)} E_j E_k$$

	$\chi_{121}^{(2)}$	$\rightarrow P_1 = \epsilon_0 \chi_{121}^{(2)} E_2 E_1 \rightarrow (-P_1) = \epsilon_0 \chi_{121}^{(2)} E_2 (-E_1) \rightarrow P_1 = P_1$	They are nonzero and originates from direction 2
	$\chi_{211}^{(2)}$	$\rightarrow P_2 = \epsilon_0 \chi_{211}^{(2)} E_1 E_1 \rightarrow (P_2) = \epsilon_0 \chi_{211}^{(2)} (-E_1) (-E_1) \rightarrow P_2 = P_2$	
	$\chi_{233}^{(2)}$	$\rightarrow P_2 = \epsilon_0 \chi_{233}^{(2)} E_3 E_3 \rightarrow (P_2) = \epsilon_0 \chi_{233}^{(2)} (-E_3) (-E_3) \rightarrow P_2 = P_2$	
	$\chi_{222}^{(2)}$	$\rightarrow P_2 = \epsilon_0 \chi_{222}^{(2)} E_2 E_2 \rightarrow (P_2) = \epsilon_0 \chi_{222}^{(2)} (E_2) (E_2) \rightarrow P_2 = P_2$	
	$\chi_{323}^{(2)}$	$\rightarrow P_3 = \epsilon_0 \chi_{323}^{(2)} E_2 E_3 \rightarrow (-P_3) = \epsilon_0 \chi_{323}^{(2)} (E_2) (-E_3) \rightarrow P_3 = P_3$	
	$\chi_{223}^{(2)}$	$\rightarrow P_2 = \epsilon_0 \chi_{223}^{(2)} E_2 E_3 \rightarrow (P_2) = \epsilon_0 \chi_{223}^{(2)} (E_2) (-E_3) \rightarrow P_2 = -P_2$	
	$\chi_{113}^{(2)}$	$\rightarrow P_1 = \epsilon_0 \chi_{113}^{(2)} E_1 E_3 \rightarrow$ Here no odd or even number of suffixes 2	They are not nonzero
	$\chi_{311}^{(2)}$	$\rightarrow P_3 = \epsilon_0 \chi_{311}^{(2)} E_1 E_1 \rightarrow$ Here no odd or even number of suffixes 2	
	$\chi_{322}^{(2)}$	$\rightarrow P_3 = \epsilon_0 \chi_{322}^{(2)} E_2 E_2 \rightarrow (-P_3) = \epsilon_0 \chi_{322}^{(2)} (E_2) (E_2) \rightarrow P_3 = -P_3$	
	$\chi_{333}^{(2)}$	$\rightarrow P_3 = \epsilon_0 \chi_{333}^{(2)} E_3 E_3 \rightarrow$ Here no odd or even number of suffixes 2	

Similarly, I choose odd number of suffixes 3 as terrace contribution because they have nonzero contribution when $3 \neq 3$ was considered due to having the broken symmetry also at the direction 3 and it originates from the interface of Au/terrace region of TiO_2 (320). The evaluation of nonzero $\chi_{ijk}^{(2)}$ elements that are responsible for the terrace contribution are mentioned below:

$$P_i = \epsilon_0 \chi_{ijk}^{(2)} E_j E_k$$

	$\chi_{121}^{(2)}$	\rightarrow	$P_1 = \epsilon_0 \chi_{121}^{(2)} E_2 E_1$	\rightarrow	Here no odd or even number of suffixes 3	They are not nonzero
	$\chi_{211}^{(2)}$	\rightarrow	$P_2 = \epsilon_0 \chi_{211}^{(2)} E_1 E_1$	\rightarrow	Here no odd or even number of suffixes 3	
	$\chi_{233}^{(2)}$	\rightarrow	$P_2 = \epsilon_0 \chi_{233}^{(2)} E_3 E_3$	\rightarrow	$(-P_2) = \epsilon_0 \chi_{233}^{(2)} (E_3)(E_3) \rightarrow -P_2 = P_2$	
	$\chi_{222}^{(2)}$	\rightarrow	$P_2 = \epsilon_0 \chi_{222}^{(2)} E_2 E_2$	\rightarrow	Here no odd or even number of suffixes 3	
	$\chi_{323}^{(2)}$	\rightarrow	$P_3 = \epsilon_0 \chi_{323}^{(2)} E_2 E_3$	\rightarrow	$(P_3) = \epsilon_0 \chi_{323}^{(2)} (-E_2)(E_3) \rightarrow P_3 = -P_3$	They are nonzero and originates from direction 3
	$\chi_{223}^{(2)}$	\rightarrow	$P_2 = \epsilon_0 \chi_{223}^{(2)} E_2 E_3$	\rightarrow	$(-P_2) = \epsilon_0 \chi_{223}^{(2)} (-E_2)(E_3) \rightarrow P_2 = P_2$	
	$\chi_{113}^{(2)}$	\rightarrow	$P_1 = \epsilon_0 \chi_{113}^{(2)} E_1 E_3$	\rightarrow	$(-P_1) = \epsilon_0 \chi_{113}^{(2)} (-E_1)(E_3) \rightarrow P_1 = P_1$	
	$\chi_{311}^{(2)}$	\rightarrow	$P_3 = \epsilon_0 \chi_{311}^{(2)} E_1 E_1$	\rightarrow	$(P_3) = \epsilon_0 \chi_{311}^{(2)} (-E_1)(-E_1) \rightarrow P_3 = P_3$	
	$\chi_{322}^{(2)}$	\rightarrow	$P_3 = \epsilon_0 \chi_{322}^{(2)} E_2 E_2$	\rightarrow	$(P_3) = \epsilon_0 \chi_{322}^{(2)} (-E_2)(-E_2) \rightarrow P_3 = P_3$	
	$\chi_{333}^{(2)}$	\rightarrow	$P_3 = \epsilon_0 \chi_{333}^{(2)} E_3 E_3$	\rightarrow	$(P_3) = \epsilon_0 \chi_{333}^{(2)} (E_3)(E_3) \rightarrow P_3 = P_3$	

In order to evaluate the nonlinear susceptibility $\chi_{ijk}^{(2)}$ elements for both the samples, I compared the SHG intensity patterns obtained in the experiments (represented by the red dots in Figs. 4.2.1.2, 4.2.1.3, 4.2.1.4 and 4.2.1.5) with those obtained by the calculation (represented by the black dots in Figs. 4.2.1.2, 4.2.1.3, 4.2.1.4 and 4.2.1.5) using the least square fitting algorithm with $\chi_{ijk}^{(2)}$ elements as fitting parameters.

I used dielectric constant of TiO_2 , $\epsilon_{//} (2.33\text{eV}) = 8.821$ and $\epsilon_{//} (4.66\text{eV}) = -7.409 + i13.24$ for the electric fields parallel to the (001) crystal axis, and $\epsilon_{\perp} (2.33\text{eV}) = 7.129$ and $\epsilon_{\perp} (4.66\text{eV}) = 3.165 + i8.15$ for the electric fields perpendicular to the (001) axis [4].

I assumed the dielectric constant of TiO₂ for the phenomenological analysis of Au/TiO₂ (320) interface because the calculation of the surface nonlinear susceptibility $\chi_{Sijk}^{(2)}$ elements are not dependent on the value of dielectric constant and the thickness of the surface layer due to the existence of very thin Au film on TiO₂ substrate. More precisely, according to the theory of Guyot-Sionnest *et al.*, I could define the surface nonlinear susceptibility $\chi_{Sijk}^{(2)}$ using three-layered model [5]. $\chi_{Sijk}^{(2)}$ was calculated by integrating $\chi_{ijk}^{(2)}$ over the surface layer as a function of depth. When some of the suffixes of the susceptibility include the coordinate 3, the integrand is divided by the dielectric function for the electric field in direction 3 on the surface layer at the frequency of the corresponding photons [6]. Here, coordinate 3 indicates the direction perpendicular to the surface plane. When I have a uniform linear and nonlinear dielectric response in the surface layer, I will have [6],

$$\chi_{S333}^{(2)} \equiv \frac{\chi_{333}^{(2)} d}{\varepsilon_{33}(2\omega)[\varepsilon_{33}(\omega)]^2} \text{-----(3)}$$

$$\chi_{S3ij}^{(2)} \equiv \frac{\chi_{3ij}^{(2)} d}{\varepsilon_{33}(2\omega)} \quad (i,j=1,2) \text{-----(4)}$$

$$\chi_{Sij3}^{(2)} \equiv \frac{\chi_{ij3}^{(2)} d}{\varepsilon_{33}(\omega)} \quad (i,j=1,2) \text{-----(5)}$$

$$\chi_{Sijk}^{(2)} \equiv \chi_{ijk}^{(2)} d \quad (i,j,k=1,2) \text{-----(6)}$$

Coordinates 1 and 2 refer to the directions within the surface plane as shown in Fig. 4.2.1.1. Here, $\chi_{ijk}^{(2)}$ is the bulk nonlinear susceptibility, d is the thickness of the surface layer. For $\chi_{Sijk}^{(2)}$ calculation, the thickness and dielectric constant of the surface layer are uniform. So, the value of the $\chi_{Sijk}^{(2)}$ is

not dependent on the thickness and dielectric constant of the surface layer of three layer model, the value of the $\chi_{Sijk}^{(2)}$ is only depended on the bulk $\chi_{ijk}^{(2)}$. As the Au film thickness is very low only 2 nm, so the value of $\chi_{Sijk}^{(2)}$ depends on the bulk $\chi_{ijk}^{(2)}$. For this reason, I assumed the dielectric constant of TiO₂ for the phenomenological analysis of Au/TiO₂ (320) interface. Then, by using the obtained ten evaluated $\chi_{ijk}^{(2)}$ elements, I separated the theoretical SHG intensity patterns into those of the terrace and step contributions.

The calculated SHG intensity patterns for both Au/TiO₂ (320) and bare TiO₂ (320) samples were shown in Table 4.2.2.1 at the excitation photon energy 1.17 eV. In Table 4.2.2.1, the contributions from the terrace group of $\chi_{ijk}^{(2)}$ elements are shown. The SHG intensity from the step contribution of the Au/TiO₂ (320) surface was 0.2 and 0.15 for Pin/Pout and Sin/Pout polarization combinations, respectively. They were smaller than the noise amplitude and are not shown. For the same reason, the fitting of the experimental data in Figs. 4.2.1.2 and 4.2.1.3 were conducted by considering only the terrace group of $\chi_{ijk}^{(2)}$ elements. Similarly, for the step contribution of the bare TiO₂ (320) surface, the SHG intensity was 0.1 and 0.2 for the Pin/Pout and Sin/Pout polarization combinations, respectively. They were much smaller than the terrace contribution shown on the bottom row of Table 4.2.2.1 and were below the noise level, and so they were not shown. The simulated SHG intensity patterns for Pin/Sout and Sin/Sout for both the Au/TiO₂ (320) and bare TiO₂ (320) were very weak. Their contributions are negligible and the corresponding intensity patterns were not shown in Table 4.2.2.1.

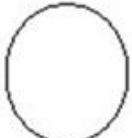
Sample	$\chi_{ijk}^{(2)}$	Pin - Pout	Pin - Sout	Sin - Pout	Sin - Sout
Au/TiO ₂ (320) (1064 nm)	Au/TiO ₂ terrace contribution	 17		 3.4	
Bare TiO ₂ (320) (1064 nm)	Bare TiO ₂ terrace contribution	 2.35		 0.62	

Table 4.2.2.1. The calculated SHG intensity patterns for both Au/TiO₂ (320) and bare TiO₂ (320) based on the terrace contribution with photon excitation energies of 1.17 eV. The SHG intensity was plotted in the radial direction in an arbitrary but common unit.

The calculated SHG intensity patterns for both Au/TiO₂ (320) and bare TiO₂ (320) samples were shown in Table 4.2.2.2 at the excitation photon energy 2.33 eV. In Table 4.2.2.2, the contributions from both the terrace and step groups of $\chi_{ijk}^{(2)}$ elements were shown. The simulated SHG intensity patterns for Pin/Sout and Sin/Sout for the Au/TiO₂ (320) were very weak. The terrace contribution for Sin/Sout for the bare TiO₂ (320) was weak. Their contributions were negligible and the corresponding intensity patterns were not shown in Table 4.2.2.2.

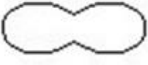
Sample	$\chi_{ijk}^{(2)}$	Pin - Pout	Pin - Sout	Sin - Pout	Sin - Sout
Au/TiO ₂ (320) (532 nm)	Au/TiO ₂ terrace contribution	 33		 12.5	
	Au/TiO ₂ step contribution	 10		 0.2	
Bare TiO ₂ (320) (532 nm)	TiO ₂ terrace contribution	 24	 0.5	 1	
	TiO ₂ step contribution	 0.6	 0.5	 0.6	 0.5

Table 4.2.2.2. The calculated SHG intensity patterns for Au/TiO₂ (320) and bare TiO₂ (320) based from the terrace and step contributions fitted to the experimental results with photon excitation energies of 2.33 eV. The SHG intensity is plotted in the radial direction in an arbitrary but common unit.

From the above simulation results of the step and terrace groups of $\chi_{ijk}^{(2)}$ elements, one can see that the step contribution of the Au/TiO₂ (320) is different from that of the bare TiO₂ (320) sample for the Pin/Pout polarization combination, as we can see it in Table 4.2.2.2. Also for the Sin/Sout polarization combination in Fig. 4.2.1.5, the bare surface shows a finite intensity, while

the Au/TiO₂ (320) gives a negligible signal for Sin/Sout polarization combination as in Fig. 4.2.1.4. In order to discuss the possible reasons for this difference, I considered the following four candidates of the origins of the step contribution to the signal of the Au/TiO₂ (320) interface. This four candidates are given as follows:

- (a) Enhancement of the incident electric field by surface defects
- (b) Electronic resonance of Au/TiO₂ interface step
- (c) Surface plasmon effect on SHG enhancement
- (d) Fresnel factor effect on SHG enhancement

Now I will discuss elaborately about the effect and influence of these four candidates in the following,

(a) Enhancement of the incident electric field by surface defects:

Surface defects such as crystal imperfections, island structures, steps and kinks are considered as a candidate origin for the electric field enhancement. The defects on the surface/interface may act as the “hot spot” and the local field can be concentrated and coupling may occur strongly. These couplings can be the origin of the enhancement of the incident electric field [7]. C. K. Chen *et al.* observed a large enhancement of SHG signal from the roughened silver surface compared to a smooth surface due to the enhancement of the electric field by the roughness [8]. From the AFM and SEM with EDX measurement, I found that Au deposited TiO₂ (320) surface contains island structure and these islands might act as “hot spot” and make the SHG intensity stronger.

However, this effect should have an isotropic nature with respect to the rotation of the sample around its normal because these islands are randomly distributed. The effect would be similar if I consider the enhancement occurring due to the random steps on the surface. This is not the case when I see the SHG pattern for Pin/Pout polarization combination shown in Fig. 4.2.1.4, and so this candidate is eliminated.

(b) Electronic resonance of Au/TiO₂ interface step:

An electronic resonance may occur at the step region of the Au/TiO₂ interface. J. R. Power *et al.* observed an enhancement of SHG signal from a stepped Si (001) surface due to the strong electronic resonance [9]. T. F. Heinz *et al.* observed SHG and SFG spectra due to the electronic resonance from the CaF₂/Si (111) interface. This electronic resonance occurred due to the interband electronic transition at the interface by the excitation by one photon [10]. In our study we observed the enhanced SHG signal (shown in Table 4.2.2.2) correlated with the existence of the Au/TiO₂ (320) interface steps. Hence the interface step electronic state being the origin of our signal is a credible candidate.

(c) Surface plasmon effect on SHG enhancement:

The collective oscillations of the free electrons may occur in metal surface such as silver, gold or copper induced by the interacting electromagnetic field and they are known as surface plasmons [11]. In the case of a thin gold film deposited on pre-patterned TiO₂ substrate, local field enhancement may result from the surface plasmon resonance (SPR). Then the SHG intensity is non-linearly dependent on the local field enhancement factors [12]. In order to check the influence of SPR and Fresnel factor effect (it will be discussed as a next candidate) on the enhancement of

the anisotropic SHG signal, I measured the linear reflectivity of my sample at $\varphi = 0^\circ$ and 180° as shown in Fig. 4.2.2.3. I choose $\varphi = 0^\circ$ and 180° for the linear optical reflectivity measurement because I observed the anisotropic response from the Au/TiO₂ (320) interface towards the $[\bar{2}30]$ direction for Pin/Pout polarization combination at incident photon energy 2.33 eV. The enhancement of the SHG signal for $\varphi = 0^\circ$ and 180° is different as shown in Fig 4.2.1.4. That is why I choose $\varphi = 0^\circ$ and 180° for the linear optical reflectivity measurement in order to confirm whether there is any influence of the SPR or Fresnel factor for the enhancement of the anisotropic SHG response.

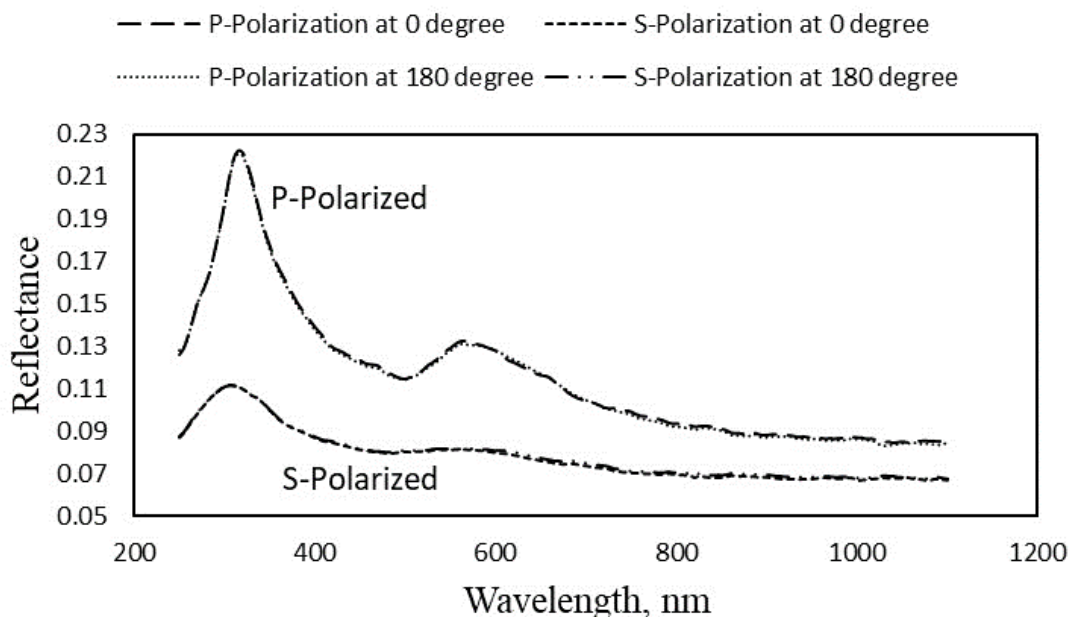


Figure 4.2.2.3. Linear reflectivity curves of Au/TiO₂ (320) sample for both P- and S- polarized light at $\varphi = 0^\circ$ and 180° as a function of wavelength.

In Fig. 4.2.2.3, the decrease of reflectivity for the p-polarization above 600 nm might be due to the contribution of SPR. Nevertheless, the reflectance at $\varphi = 0^\circ$ and 180° were found to

be approximately the same as each other for both P- and S- polarized excitation light. Although the enhancement of the excitation light field at ω can occur at the step edge by the enhancement of incident electric field but this enhancement should be identical for $\varphi = 0^\circ$ and 180° . More precisely, the step edge behavior to the incoming incident light having the same electric field of frequencies will be the same for these two φ 's. Even if the intensity of the incident field increased, the pattern of the reflectivity curve will remain the same for $\varphi = 0^\circ$ and 180° . Thus the incident field of frequency ω makes approximately the same local field in the sample at $\varphi = 0^\circ$ and 180° . So the different enhancement of SHG signal between $\varphi = 0^\circ$ and 180° should not occur owing to SPR.

(d) Fresnel factor effect on the SHG enhancement:

The intensity of the surface second harmonic signal per laser pulse $I(2\omega, l, \varphi)$ is given by the following equation [13],

$$I(2\omega, l, \varphi) \propto |L(2\omega, l, \varphi) \chi^{(2)}(l, \varphi) L(\omega, l, \varphi)|^2 I^2(\omega) \quad \text{-----(7)}$$

Here, $L(\omega, l, \varphi)$ and $L(2\omega, l, \varphi)$ are the Fresnel factors at frequencies of ω and 2ω respectively, and $I(\omega)$ is the intensity of the incident laser pulses. The parameter l indicates the polarization of the light wave and is either s or p. The parameter φ indicates the sample rotation angle. The Fresnel factor $L(\omega, l, \varphi)$ indicates how much light field at frequency ω is generated inside the nonlinear medium by the incident light by the linear optical process [3]. From our linear measurement, we confirmed that the linear reflectivity spectra are the same between the rotation angles $\varphi = 0^\circ$ and 180° as shown in Fig. 7. The fact that the reflectivity spectra are exactly the same means that the Fresnel factors are the same between the rotation angles $\varphi = 0^\circ$ and 180° . Hence the enhancement

of the SHG signal should only be due to the φ -dependence of the $\chi^{(2)}(l, \varphi)$ term in Eq. (2). So, the influence of the Fresnel factors on the enhancement of SHG signal can be eliminated.

From the above discussion of four candidates, it seems that only candidate (b) is feasibly responsible for the enhancement of the SHG. In this case, the electronic resonance at the Au/TiO₂ (320) interface step may have caused the enhancement of the SHG signal.

Although it is difficult to conclude the exact origin of the enhancement of the SHG intensity considering the step contributions of Au/TiO₂ (320) compared to the bare TiO₂ (320) sample, I have succeeded in decomposing theoretically the nonlinear susceptibility elements of anisotropic and isotropic symmetry from the experimental data. The SHG pattern of Pin/Pout shown in Fig. 4.2.1.4 is the combination of the two groups of $\chi_{ijk}^{(2)}$ elements shown in Fig. 4.2.2.2. These two components of the two groups of $\chi_{ijk}^{(2)}$ elements give positive interference at $\varphi=180^\circ$ and negative interference at $\varphi=0^\circ$ as I show it in Fig. 4.2.2.4.

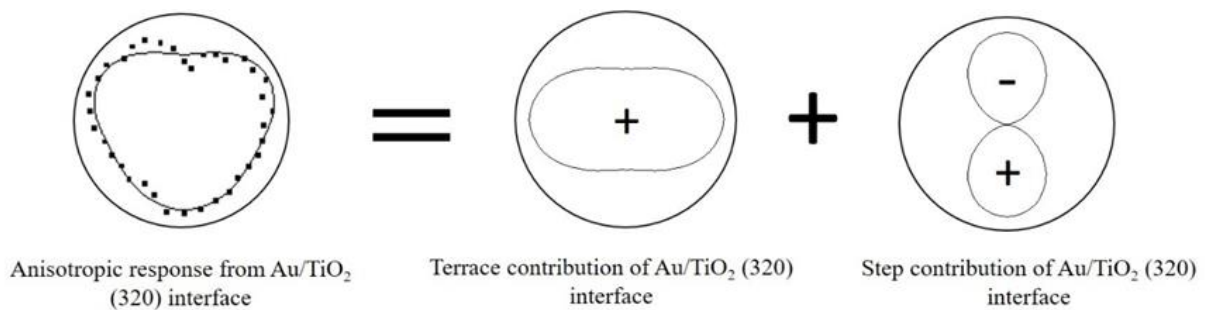


Figure 4.2.2.4. The anisotropic response for Pin/Pout polarization combination from the Au/TiO₂ (320) interface at excitation light with photon energy 2.33 eV separated into the step and terrace contributions.

The same physical phenomena happened for the SHG intensity patterns of Sin/Pout for Au/TiO₂ (320) and SHG intensity patterns of Pin/Pout for bare TiO₂ (320), as shown in Fig. 4.2.1.4 and 4.2.1.5, respectively. However, the SHG intensity pattern of Sin/Pout for bare TiO₂ (320) shown in Fig. 4.2.1.5 was reproduced by the contribution of two groups of $\chi_{ijk}^{(2)}$ elements giving positive interference at $\varphi=0^\circ$ and negative interference at $\varphi=180^\circ$. Similar physical phenomena occurred for the Pin/Sout and Sin/Sout polarization combinations shown in Fig. 4.2.1.5. Negative and positive interference can occur due to the change of the incident plane with respect to the direction of $\chi_{step}^{(2)}$ with the rotation from $\varphi=0^\circ$ to $\varphi=180^\circ$ as a function of $(\beta_{ijk}, \varphi, l)$. Here, β_{ijk} is the hyperpolarizability, φ is the azimuthal angle and l is the polarization direction (s/p-polarization.) Therefore, the induced nonlinear polarization direction can be changed from negative to positive interference with the rotation of the sample $\varphi=0^\circ$ to $\varphi=180^\circ$.

Let's discuss the reason for occurrence of positive and negative interference with a diagram considering the rotation of the electric field direction in order to make understanding more clear. Fig. 4.2.2.5 shows, the interaction between the sample (fixed) and the incident polarized light and φ denotes the direction of the incident k-vector.

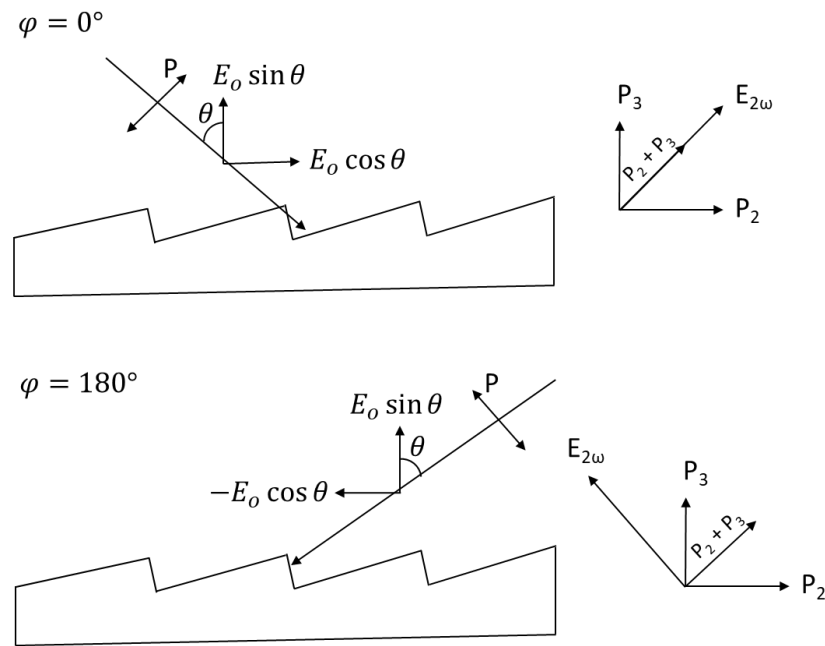


Figure 4.2.2.5. The interaction between the sample in a fixed position and the changing electric field direction from $\varphi=0^\circ$ to $\varphi=180^\circ$.

As I described earlier in this chapter by the Fig. 4.2.1.1, direction 2 and 3 correspond to step and terrace direction, respectively. Now if I consider the main contribution of $\chi_{ijk}^{(2)}$ considering the terrace and step contribution at the direction 3 and direction 2, respectively, I can write the following equations,

$$P_3 = \chi_{333}^{(2)} E_3 E_3 = \begin{cases} \chi_{333}^{(2)} (E_o \sin \theta)^2 & \text{At, } \varphi = 0^\circ \\ \chi_{333}^{(2)} (E_o \sin \theta)^2 & \text{At, } \varphi = 180^\circ \end{cases} \text{-----(8)}$$

$$P_2 = \chi_{222}^{(2)} E_2 E_2 = \begin{cases} \chi_{222}^{(2)} (E_o \cos \theta)^2 & \text{At, } \varphi = 0^\circ \\ \chi_{222}^{(2)} (-E_o \cos \theta)^2 & \text{At, } \varphi = 180^\circ \end{cases} \text{-----(9)}$$

The equation (8) and (9) express the induced nonlinear polarization at the terrace and step respectively. The induced nonlinear polarization occurred similarly for $\varphi = 0^\circ$ to $\varphi = 180^\circ$ according to the equation (8). That means, when I consider terrace contribution for $\chi_{333}^{(2)}$ the SHG was generated in exactly the same way for both $\varphi = 0^\circ$ and $\varphi = 180^\circ$, when I consider terrace contribution for $\chi_{333}^{(2)}$. However, the phase of SHG electric field is opposite for $\varphi = 0^\circ$ and $\varphi = 180^\circ$ according to equation (9). This is because considering the main contribution of step, i.e. $\chi_{222}^{(2)}$, the induced polarization P_2 at the step direction is in the same direction as the k-vector for $\varphi = 0^\circ$ and in the opposite direction to the k-vector for $\varphi = 180^\circ$, as seen in Fig. 4.2.2.5. Therefore, the positive interference occurred when the direction of the incident electric field was $\varphi = 0^\circ$, and the negative interference occurred when the direction of the incident electric field was $\varphi = 180^\circ$.

As the next step it is important to perform the photon energy dependence of the SHG response. At that step, the separation of the SHG response as in Table 4.2.2.2 is necessary to discuss the terrace and step contribution.

4.3 Summary of this Chapter

I obtained SHG intensity patterns from the Au/TiO₂ (320) and bare TiO₂ (320) samples as a function of the polarization combinations and azimuthal angle. The isotropic response was observed from both samples with the excitation photon energy of 1.17eV. On the other hand, at excitation photon energy 2.33 eV, anisotropic SHG signal was detected from both the Au/TiO₂ (320) and bare TiO₂ (320) samples. Then I made ($\chi_{ijk}^{(2)}$) analysis and divide them into two groups to obtain the specific contribution of steps in order to investigate the electronic states of the Au/TiO₂ (320) interface. I also observed the surface morphology by AFM before and after the Au deposition on the TiO₂ (320) single crystal in order to check the probability of the existence of the Au island. I found the island structure and it was confirmed by the SEM analysis too. I also checked the distribution of Au thin film by EDX analysis. I observed that the whole TiO₂ (320) surface was covered by the Au film. I measured the linear optical reflectivity in order to confirm the influence of surface plasmon resonance or Fresnel factor for the enhancement of the anisotropic SHG signal obtained from the Au/TiO₂ (320) interface. From the reflectivity data of the Au/TiO₂ (320) interface, it was observed that the reflectivity for P- and S- polarized light are almost the same at the azimuthal angle, $\varphi = 0^\circ$ and 180° . This result indicates that the linear optical process at frequency ω occurs almost in the same way at $\varphi = 0^\circ$ and 180° and it means that even if there is any SPR occurred there is no effect on the enhanced SHG signal due to the different response from the $\varphi = 0^\circ$ and 180° . This discussion is also true for the Fresnel factors. Therefore, there is no influence of Fresnel factors on the enhancement of SHG signal. I can conclude that, after eliminating other candidate mechanisms discussed in this chapter, an electronic resonance at the Au/TiO₂ (320) interface step is the major contributor to the relevant $\chi_{ijk}^{(2)}$ elements.

References

- [1] Md Ehasanul Haque, Daiki Kobayashi, Yuki Tomatsu, Khuat Thi Thu Hien, Goro Mizutani, Mohammad Mizanur Rahman and Harvey N. Rutt, *AIP Advances* 7, 125011 (2017).
- [2] E. Kobayashi, G. Mizutani, and S. Ushioda, *Jpn. J. Appl. Phys.* 36, 7250, (1997).
- [3] A. G. Lambert, P. B. Davies, and D. J. Neivandt, *Appl. Spectrosc. Rev.* 40, 103, (2005).
- [4] M. W. Ribarsky, *Hand Book of Optical Constants of Solids* ed E D Palik (San Diego, CA: Academic) 795, (1985).
- [5] P. Guyot-Sionnest, W. Chen and Y. R. Shen, *Phys. Rev. B* 33, 8254, (1986).
- [6] M. Omote, H. Kitaoka, E. Kobayashi, O. Suzuki, K. Aratake, H. Sano, G. Mizutani, W. Wolf, and R. Podloucky, *Journal of Physics: Condensed Matter.* 17, 8, S175-S200, (2005).
- [7] D. L. Mills, *Nonlinear Optics Basic Concepts*, 2nd edition, Springer, 173-174, (1998).
- [8] C. K. Chen, A. R. B. de Castro, and Y. R. Shen, *Phys. Rev. Lett.* 46, 145, (1981).
- [9] J. R. Power, J. D. O'Mahony, S. Chandola, and J. F. McGilp, *Phys. Rev. Lett.* 75, 1138-1141, (1995).
- [10] T. F. Heinz, F. J. Himpsel, and E. Palange, *Phy. Rev. Lett.* 63, 6, (1989).
- [11] A. Lesuffleur, P. Gogol, P. Beauvillain, B. Guizal, D. Van Labeke, and P. Georges, *J. Appl. Phys.* 104, 124310, (2008).
- [12] C. Hubert, L. Billot, P. –M. Adam, R. Bachelot, P. Royer J, Grand D. Gindre, K. D. Dorkenoo, and A. Fort, *Appl. Phys. Lett.* 90, 181105, (2007).
- [13] P. J. Campagnola, M. Wei, A. Lewis, and L. M. Loew, *Biophysical Journal.* 77, 3341-3349, (1999).

Chapter 5: General Conclusion

In this research work, I investigated the electronic states of stepped Au/TiO₂ (320) interface through the nonlinear optical tensor analysis. The interface of Au/TiO₂ acts as an active site for many catalytic reactions such as reduction of nitrogen oxides, partial oxidation of hydrocarbons, hydrogenation of unsaturated hydrocarbons, oxidation of carbon monoxides and so on. Therefore, I observed the electronic state of Au/TiO₂ (320) interface by second harmonic generation (SHG) to contribute for the development of the catalyst field. In this regard, I have fabricated gold thin film with thickness of 2 nm on the stepped TiO₂ (320) substrate in a vacuum chamber at 2×10^{-7} Torr. SHG is forbidden in the bulk of a medium having inversion symmetry within the electric dipole approximation, while SHG is allowed at the surface or interface where inversion symmetry is broken. Therefore, SHG has a big advantage to investigate a stepped Au/TiO₂ interface with high selectivity. I have observed the azimuthal angle and polarization dependent SHG intensities from the Au/TiO₂ (320) interface and bare TiO₂ (320) using the excitation photon energy of 1.17 eV for 1064 nm and 2.33 eV for 532 nm wavelength of pulsed laser light. The source of the photon energy excitation is the pulsed Nd³⁺:YAG laser. In case of excitation photon energy of 1.17 eV, isotropic responses were observed from both samples. In contrast, the anisotropic response from both Au /TiO₂ (320) and bare TiO₂ (320) were observed when the excitation photon energy of 2.33 eV was used as the incident probe. Interestingly, an anisotropic structure was observed to the $[\bar{2}30]$ direction for Pin/Pout polarization combination. From the experimental data, I decomposed theoretically the ten nonzero nonlinear susceptibility elements ($\chi_{ijk}^{(2)}$) such as $\chi_{223}^{(2)} = \chi_{232}^{(2)}$, $\chi_{113}^{(2)} = \chi_{131}^{(2)}$, $\chi_{112}^{(2)} = \chi_{121}^{(2)}$, $\chi_{211}^{(2)}$, $\chi_{222}^{(2)}$, $\chi_{233}^{(2)}$, $\chi_{323}^{(2)} = \chi_{332}^{(2)}$, $\chi_{311}^{(2)}$, $\chi_{322}^{(2)}$, and $\chi_{333}^{(2)}$. Here, 1, 2, and 3 represent the [001], $[\bar{2}30]$, and [320] directions on the stepped TiO₂ (320) surface, respectively, and their axes are fixed to the sample. After that, I divided them into two groups such as step

and terrace contribution groups. Here, $\chi_{121}^{(2)}$, $\chi_{211}^{(2)}$, $\chi_{222}^{(2)}$, $\chi_{233}^{(2)}$, and $\chi_{323}^{(2)}$ with odd number of suffices 2 originate from the step contribution and the other five susceptibilities $\chi_{113}^{(2)}$, $\chi_{223}^{(2)}$, $\chi_{311}^{(2)}$, $\chi_{322}^{(2)}$, and $\chi_{333}^{(2)}$ with odd numbers of suffices 3 originate from the terrace contribution. Direction 2 is parallel to surface lying in the mirror plane of TiO₂ and perpendicular to step edge. Direction 3 is perpendicular to the optical plane of stepped bare TiO₂ (320) single crystal. I have calculated SHG intensity patterns for Au/TiO₂ (320) and bare TiO₂ (320) based from the terrace and step contributions fitted to the experimental results with photon excitation energies of 2.33 eV. The anisotropic responses were observed due to the contributions of both the step and terrace groups of $\chi_{ijk}^{(2)}$ elements. From the calculated results of the step and terrace groups of $\chi_{ijk}^{(2)}$ elements, it was observed that the step contribution of the Au/TiO₂ (320) is different from that of the bare TiO₂ (320) sample for the Pin/Pout polarization combination. In order to discuss the possible reasons for this difference, I considered the four possible mechanism candidates as an origin of the signal enhancement from the Au/TiO₂ (320) interface. The four candidates are (a) Enhancement of the incident electric field by surface defects (b) Electronic resonance of Au/TiO₂ interface step (c) Surface plasmon effect on SHG enhancement (d) Fresnel factor effect on SHG enhancement.

I found that Au deposited TiO₂ (320) surface contains island structure by the observation of AFM and SEM with EDX and these islands might act as “hot spot” and make the SHG intensity stronger and I considered this kind of surface defects as one of the mechanism candidates. However, this effect should have an isotropic nature with respect to the rotation of the sample around its normal because these islands are randomly distributed. The effect would be similar if we consider the enhancement occurring due to the random steps on the surface. This is not the case when I see the SHG pattern for Pin/Pout polarization

combination. So, this candidate should be eliminated. In order to explain the second mechanism candidate, I considered an electronic resonance at the step region of the Au/TiO₂ (320) interface. I observed the enhanced SHG signal correlated with the existence of the Au/TiO₂ (320) interface steps. Hence this is a credible candidate that the origin of the enhanced signal is the interface step electronic state. In the case of a thin gold film deposited on pre-patterned TiO₂ substrate, local field enhancement may result from the surface plasmon resonance (SPR) which I considered as the third mechanism candidate. I measured the linear optical reflectivity in order to confirm whether there is any influence of surface plasmon resonance or the effect of Fresnel factor (considered as the fourth mechanism candidate) for the enhancement of the anisotropic SHG signal obtained from both the Au/TiO₂ (320) interface. From the reflectivity data of the Au/TiO₂ (320) interface, it was observed that the reflectivity for P- and S- polarized light are almost the same at the azimuthal angle, $\varphi = 0^\circ$ and 180° . This result indicates that the linear optical process at frequency ω occurs almost in the same way at $\varphi = 0^\circ$ and 180° and it means that even if there is any SPR occurring there is no effect on the anisotropic enhancement of the SHG signal due to the different nonlinear response from the interface between $\varphi = 0^\circ$ and 180° . This discussion is also true for the Fresnel factors. Therefore, there is no influence of Fresnel factors on the enhancement of SHG signal.

This analysis suggests that, an electronic resonance at the step of the Au/TiO₂ (320) interface is the major contributor to the relevant $\chi_{ijk}^{(2)}$ elements. This separation of step and terrace contributions to the nonlinear susceptibility elements from the stepped Au/TiO₂ (320) interface is the most significant point of this research. As it is well known, the steps and kinks can act as active sites for catalysis. Except SHG, other surface tools are not so sensitive to the steps because the number density of steps are normally lower than the terrace atoms and only

SHG can pick up step contribution separately for the step structures. This analysis provides important information for the future SHG spectroscopy of the electronic states of the Au/TiO₂ (320) interface as a function of the incident photon energy. The spectrum would be closely related to the catalytic activity of this interface for many chemical reactions.

Appendix – I

Synopsis of Minor Research

Carbon nanotubes (CNTs) have been recognized originally by Sumio Iijima in 1991 [1]. CNTs are made of carbon atom by rolling up a graphene sheet with tubular nanostructure. CNTs have large variety of physical properties due to having different individual graphene layer which is rolled up in to a tube. The wide variety of electronic structures in combination with a mechanically strong nanoscale lattice and outstanding optical properties are among the main reasons for the large interest in using CNTs in future electric and optical applications [2]. Due to having many interesting features and applications in the field of electronics and optics, it needs quality characterization methods that are fast, precise and cost-effective to determine the nonlinear optical property. In this regard, I intended to investigate the nonlinear second order response from the CNT/PEP interface. The main purposes of our work was to measure SHG intensity for checking the immobilization of peptide molecules on CNT surface and make a significant improvement of bio-sensing materials field. As the SHG method is new to apply for investigating the peptide molecules, it is our great interest to observe the SHG response from CNT/PEP interface.

Nonlinear techniques are interesting because nanomaterials can have remarkably large nonlinear optical responses that can provide complementary information [3]. Second harmonic generation (SHG) is very promising nonlinear technique to explore electronic information from the nanomaterials. SHG methods are very sensitive to symmetry and are forbidden in centrosymmetric materials with in the electric-dipole approximation of the light-matter interaction

[4]. When the incident light of frequency ω comes to the asymmetry medium, the light of frequency 2ω will be generated. This phenomenon is SHG. In addition, when incident light of frequency ω comes to the symmetry medium, the light of frequency 2ω will not be generated in electric dipole approximation. Therefore, SHG spectroscopy is sensitive to surface and interface where the spatial symmetry is broken. In case of our growing CNT, it is randomly grown on the substrate and also the peptide molecules are also randomly distributed as irregular film on the CNT surface. So the surface is noncentrosymmetric which can generate SHG due to having the chiral structure in the long chain molecule of peptides.

I observed the SHG intensity from the peptide molecules absorbed carbon nanotube surface grown on the Si/SiO₂/Co substrate. We dropped different concentrations of peptide molecules such as 100nM, 1 μ M and 10 μ M on the three Si/SiO₂/Co/CNT substrate individually. The SHG intensity was measured from the CNT/PEP interface by using 1.17 eV pulsed laser light. The results show that, the SHG intensity increased with increasing the peptide concentrations. In order to confirm whether the SHG signal was really detected or the collected signal is a noise from the CNT/PEP interface, I prepared the three different Si/SiO₂ substrate and dropped similar concentrations of peptide molecule having no CNT layer individually. In this case, similar results were observed as I found from the CNT/PEP interface. In this case, the SHG intensity also increased with increasing the concentrations of peptide molecules on the surface. Therefore, it can be concluded that, the peptide molecules can generate SHG due to having a long chain structure that may consist of chirality. These chiral characteristics are mainly responsible for generating SHG signal.

References

- [1] S. Iijima, Helical microtubes of graphitic carbon. *Nature*, 354, 56-58 (1991).
- [2] P. Avouris, Z. Chen, and V. Perebeinos, *Nature Nanotech*, 2, 605-615 (2007).
- [3] M. C. Harsam, *Nature Nanotech*, 3, 387-394 (2008).
- [4] Y. R. Shen, *Nature*, 337, 519-525 (1989).

Appendix - II

Phenomenological analysis of the SHG intensity patterns

We used the Maxwell's equations with a nonlinear source term to calculate the amplitude of the electric field radiated by the nonlinear polarization. The equation is as follows-

$$\vec{\nabla} \times (\vec{\nabla} \times \vec{E}) + \epsilon_o \mu_o \frac{\partial^2 \vec{\epsilon}}{\partial t^2} \vec{E} = -\mu_o \frac{\partial^2 \vec{P}_{NL}}{\partial t^2} \quad (1)$$

Where, ϵ_o is the permittivity in vacuum, μ_o is the vacuum permeability, \vec{E} is the electric field of the SHG light, $\vec{\epsilon}$ is the dielectric tensor and \vec{P}_{NL} is the nonlinear polarization. The nonlinear polarization on the right hand side of equation (1) acts as the source term and generates the electric field of frequency 2ω on the left hand side.

The amplitude of a second harmonic wave can be calculated by a three-layered dielectric model shown in Fig. 1. In this model, layer 1 is a vacuum layer, layer 2 is the surface layer with second order nonlinearity, and layer 3 is the bulk layer with out optical nonlinearity. The origin of the second order nonlinearity in layer 2 is the breaking of symmetry in the direction normal to the surface and also direction parallel to the surface that lies in the mirror plane of TiO₂ and perpendicular to step edge. We assumed that layer 2 is a thin layer with a uniform linear and nonlinear optical response. In fact the dielectric structure of the real surface layer is not so simple. In such a case the radiation from nonlinear polarizations can be regarded as that from one homogeneous dipole sheet. In this model, the c-axis in layer 3 lies in direction

1. The co-ordinates shown here are the laboratory co-ordinates and not the crystal co-ordinates.

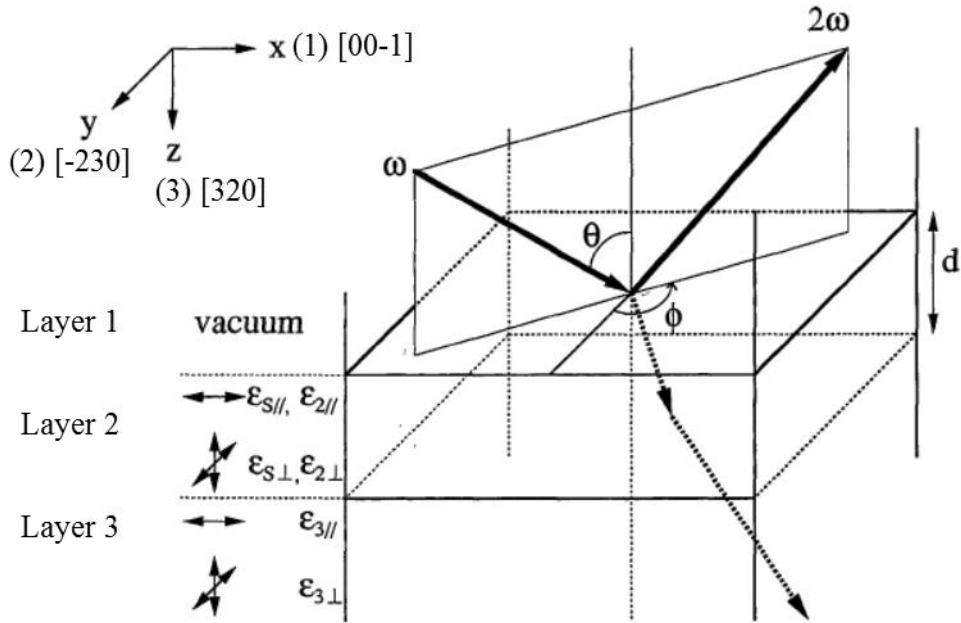


Figure. 1. Dielectric model of a thin-layer system used in the phenomenological analysis. The dielectric constants for the electric fields in the directions indicated by arrows are shown for the above model. Here, θ is the incident angle and ϕ is the between the y-axis and the incident plane. On the left hand side, the dielectric constants of the second and third layers are defined at frequencies ω ($\epsilon_{s||}$, $\epsilon_{s\perp}$) and 2ω ($\epsilon_{2||}$, $\epsilon_{2\perp}$, $\epsilon_{3||}$, $\epsilon_{3\perp}$). The suffixes $||$ and \perp denote directions parallel and perpendicular to the c-axis of the crystal.

The surface second order nonlinear polarization in layer 2 is defined as,

$$P_{s,i}^{(2)}(2\omega) = \sum_{ijk} \chi_{ijk}^{(2)} E_j E_k \dots (2)$$

Here,

$P_s^{(2)}$ = Surface nonlinear optical polarization

ϵ_0 = Dielectric constant in a vacuum

$\chi_s^{(2)}$ = Second order nonlinear susceptibility at surface

E = Incident electric field

In order to calculate the SHG intensity, the electric field amplitude of the incident laser beam in layers 2 and 3 is calculated first using Maxwell's equations which is shown below. The nonlinear polarization exists only in the second layer. A similar treatment was shown by Kumagai *et al.* [1] for a medium anisotropic in the incident plane. So, I only mention the equations that is used to calculate the electric field amplitude. The solution of the Maxwell's electromagnetic wave equation consists of homogeneous and inhomogeneous parts,

$$E(2\omega) = E_H + E_{IH} \dots\dots(3)$$

The homogeneous solution E_H is a free plane wave at frequency 2ω obtained by solving equation (1) with the right hand side set equal to zero. The inhomogeneous solution in the second layer $E_{IH} = E_{IH}^0 \exp[i(k_s \cdot r - 2\omega t)]$ with k_s being the wave vector of the SHG source polarization which is obtained by solving equation (1) [1].

(1) Linear reflection and refraction in an isotropic medium:

First we show the equation for the internal field of the excitation beam in a dielectric structure shown in Fig. 1.

$$\begin{pmatrix}
 -\sin\phi & -\cos\theta\cos\phi & -e_{2o\downarrow x}^\omega & -e_{2e\downarrow x}^\omega & -e_{2o\uparrow x}^\omega & -e_{2e\uparrow x}^\omega & 0 & 0 \\
 \cos\phi & -\cos\theta\sin\phi & -e_{2o\downarrow y}^\omega & -e_{2e\downarrow y}^\omega & -e_{2o\uparrow y}^\omega & -e_{2e\uparrow y}^\omega & 0 & 0 \\
 \cos\theta\cos\phi & -\sin\phi & -a_{2o\downarrow x}^\omega & -a_{2e\downarrow x}^\omega & -a_{2o\uparrow x}^\omega & -a_{2e\uparrow x}^\omega & 0 & 0 \\
 \cos\theta\sin\phi & \cos\phi & -a_{2o\downarrow y}^\omega & -a_{2e\downarrow y}^\omega & -a_{2o\uparrow y}^\omega & -a_{2e\uparrow y}^\omega & 0 & 0 \\
 0 & 0 & e_{2o\downarrow x}^\omega e^{i\alpha_{2o}^\omega} & e_{2e\downarrow x}^\omega e^{i\alpha_{2e}^\omega} & e_{2o\uparrow x}^\omega e^{-i\alpha_{2o}^\omega} & e_{2e\uparrow x}^\omega e^{-i\alpha_{2e}^\omega} & -e_{3o\downarrow x}^\omega e^{i\alpha_{3o}^\omega} & -e_{3e\downarrow x}^\omega e^{i\alpha_{3e}^\omega} \\
 0 & 0 & e_{2o\downarrow y}^\omega e^{i\alpha_{2o}^\omega} & e_{2e\downarrow y}^\omega e^{i\alpha_{2e}^\omega} & e_{2o\uparrow y}^\omega e^{-i\alpha_{2o}^\omega} & e_{2e\uparrow y}^\omega e^{-i\alpha_{2e}^\omega} & -e_{3o\downarrow y}^\omega e^{i\alpha_{3o}^\omega} & -e_{3e\downarrow y}^\omega e^{i\alpha_{3e}^\omega} \\
 0 & 0 & a_{2o\downarrow x}^\omega e^{i\alpha_{2o}^\omega} & a_{2e\downarrow x}^\omega e^{i\alpha_{2e}^\omega} & a_{2o\uparrow x}^\omega e^{-i\alpha_{2o}^\omega} & a_{2e\uparrow x}^\omega e^{-i\alpha_{2e}^\omega} & -a_{3o\downarrow x}^\omega e^{i\alpha_{3o}^\omega} & -a_{3e\downarrow x}^\omega e^{i\alpha_{3e}^\omega} \\
 0 & 0 & a_{2o\downarrow y}^\omega e^{i\alpha_{2o}^\omega} & a_{2e\downarrow y}^\omega e^{i\alpha_{2e}^\omega} & a_{2o\uparrow y}^\omega e^{-i\alpha_{2o}^\omega} & a_{2e\uparrow y}^\omega e^{-i\alpha_{2e}^\omega} & -a_{3o\downarrow y}^\omega e^{i\alpha_{3o}^\omega} & -a_{3e\downarrow y}^\omega e^{i\alpha_{3e}^\omega}
 \end{pmatrix}
 \begin{pmatrix}
 E_{rs0}^\omega \\
 E_{rp0}^\omega \\
 E_{2o\downarrow 0}^\omega \\
 E_{2e\downarrow 0}^\omega \\
 E_{2o\uparrow 0}^\omega \\
 E_{2e\uparrow 0}^\omega \\
 E_{3o\downarrow 0}^\omega \\
 E_{3e\downarrow 0}^\omega
 \end{pmatrix}$$

$$= \begin{pmatrix}
 -\cos\theta\cos\phi E_{inp0}^\omega + \sin\phi E_{ins0}^\omega \\
 -\cos\theta\sin\phi E_{inp0}^\omega - \cos\phi E_{ins0}^\omega \\
 \sin\phi E_{inp0}^\omega + \cos\theta\cos\phi E_{ins0}^\omega \\
 -\cos\phi E_{inp0}^\omega + \cos\theta\sin\phi E_{ins0}^\omega \\
 0 \\
 0 \\
 0 \\
 0
 \end{pmatrix} \dots\dots\dots(4)$$

Here E_{ri0}^ω ($i=s,p$) is the electric field amplitude of the reflected light of i -polarization in layer 1. It is defined by

$$\vec{E}_{rs}^\omega = E_{rs0}^\omega \begin{pmatrix} -\sin\phi \\ \cos\phi \\ 0 \end{pmatrix} e^{\frac{i\omega}{c}(\sin\theta\cos\phi x + \sin\theta\sin\phi y - \cos\theta z) - i\omega t} \dots\dots\dots(5)$$

$$\vec{E}_{rp}^\omega = E_{rp0}^\omega \begin{pmatrix} -\cos\theta\cos\phi \\ -\cos\theta\sin\phi \\ -\sin\theta \end{pmatrix} e^{\frac{i\omega}{c}(\sin\theta\cos\phi x + \sin\theta\sin\phi y - \cos\theta z) - i\omega t} \dots\dots\dots(6)$$

Here, \vec{E}_{rs}^ω and \vec{E}_{rp}^ω are the s- and p-polarized reflected electric fields, respectively. E_{ijk}^ω ($i = 2,3; j = e, o; k = \downarrow, \uparrow$) is the electric field in the i -th layer and is defined

by,

$$\vec{E}_{ijk}^{\omega} = E_{ijk0}^{\omega} \vec{e}_{ijk}^{\omega} e^{i\vec{k}_{ijk}^{\omega} \cdot \vec{r} - i\omega t} \quad \text{.....(7)}$$

The suffices e and o denote the extraordinary and ordinary electromagnetic waves, respectively. The suffices ↓ and ↑ denote the downward and upward propagating waves, respectively.

The \vec{e}_{ik}^{ω} vector is the unit polarization vector of the electric field and can be written as,

$$e_{io{k}^{\omega} = \frac{1}{\sqrt{\epsilon_{i\perp}^{\omega} - \sin^2 \theta \cos^2 \phi}} \begin{pmatrix} 0 \\ -\sqrt{\epsilon_{i\perp}^{\omega} - \sin^2 \theta} \\ \pm \sin \theta \sin \phi \end{pmatrix} \quad \text{.....(8)}$$

(+ and - signs for k = ↓ and ↑ , respectively)

$$e_{iek}^{\omega} = \frac{1}{\sqrt{\epsilon_{i\parallel}^{\omega} + \left(\frac{\epsilon_{i\parallel}^{\omega}}{\epsilon_{i\perp}^{\omega}}\right) \sin^2 \theta \cos^2 \phi \left(\frac{\epsilon_{i\parallel}^{\omega}}{\epsilon_{i\perp}^{\omega}} - 1\right)}}$$

$$\times \begin{pmatrix} \frac{\sqrt{\epsilon_{i\parallel}^{\omega} \left(1 - \frac{1}{\epsilon_{i\perp}^{\omega}} \sin^2 \theta \cos^2 \phi\right)}}{\epsilon_{i\parallel}^{\omega} \sin^2 \theta \cos \phi \sin \phi} \\ - \frac{\epsilon_{i\perp}^{\omega} \sqrt{\epsilon_{i\parallel}^{\omega} \left(1 - \frac{1}{\epsilon_{i\perp}^{\omega}} \sin^2 \theta \cos^2 \phi\right)}}{\epsilon_{i\perp}^{\omega} \sqrt{\epsilon_{i\parallel}^{\omega} \left(1 - \frac{1}{\epsilon_{i\perp}^{\omega}} \sin^2 \theta \cos^2 \phi\right)}} \\ \frac{\epsilon_{i\parallel}^{\omega} \sin \theta \cos \phi}{\epsilon_{i\perp}^{\omega} \sqrt{\epsilon_{i\parallel}^{\omega} \left(1 - \frac{1}{\epsilon_{i\perp}^{\omega}} \sin^2 \theta \cos^2 \phi\right)}} \sqrt{\epsilon_{i\parallel}^{\omega} - \sin^2 \theta \sin^2 \phi - \frac{\epsilon_{i\parallel}^{\omega}}{\epsilon_{i\perp}^{\omega}} \sin^2 \theta \cos^2 \phi} \end{pmatrix} \quad \text{.....(9)}$$

(- and + signs for k = ↓ and ↑ , respectively)

and \vec{k}_{ijk}^ω in equation (7) is defined by,

$$\vec{k}_{iok}^\omega = \frac{\omega}{c} \begin{pmatrix} \sin\theta \cos\phi \\ \sin\theta \sin\phi \\ \pm \sqrt{\epsilon_{i\perp}^\omega - \sin^2\theta} \end{pmatrix} \quad \dots\dots(10)$$

$$\vec{k}_{iek}^\omega = \frac{\omega}{c} \begin{pmatrix} \sin\theta \cos\phi \\ \sin\theta \sin\phi \\ \pm \sqrt{\epsilon_{i//}^\omega - \sin^2\theta \sin^2\phi - \frac{\epsilon_{i//}^\omega}{\epsilon_{i\perp}^\omega} \sin^2\theta \cos^2\phi} \end{pmatrix} \quad \dots\dots(11)$$

(+ and - signs for $k = \downarrow$ and \uparrow , respectively)

α_{ijkx}^ω and $\alpha_{ijk_y}^\omega$ in the matrix elements in equation (4) are defined by,

$$a_{ijkx}^\omega = \frac{c}{\omega} (k_{ijk_y}^\omega e_{ijkz}^\omega - k_{ijkz}^\omega e_{ijk_y}^\omega) \quad \dots\dots(12)$$

$$a_{ijk_y}^\omega = \frac{c}{\omega} (k_{ijkz}^\omega e_{ijkx}^\omega - k_{ijkx}^\omega e_{ijkz}^\omega) \quad \dots\dots(13)$$

and α_{ij}^ω is defined by,

$$\alpha_{ij}^\omega = k_{ij\downarrow z}^\omega d \quad (i = 2,3; j = e, o) \quad \dots\dots(14)$$

(2) SHG electric field radiated from an anisotropic medium:

The inhomogeneous solution in the second layer $E_{IH} = E_{IH}^0 \exp[i(k_s \cdot r - 2\omega t)]$ with k_s being the wave vector of the SHG source polarization, is obtained by solving the following matrix equation,

$$\begin{pmatrix} (k_{S_y}^2 + k_{S_z}^2) - \frac{4\omega^2}{c^2} \epsilon_{2\parallel} & -k_{S_x} k_{S_y} & -k_{S_x} k_{S_z} \\ -k_{S_x} k_{S_y} & (k_{S_x}^2 + k_{S_z}^2) - \frac{4\omega^2}{c^2} \epsilon_{2\perp} & -k_{S_y} k_{S_z} \\ -k_{S_x} k_{S_z} & -k_{S_y} k_{S_z} & (k_{S_x}^2 + k_{S_y}^2) - \frac{4\omega^2}{c^2} \epsilon_{2\perp} \end{pmatrix} \begin{pmatrix} E_{IHx}^0 \\ E_{IHy}^0 \\ E_{IHx}^0 \end{pmatrix} = \frac{16\pi\omega^2}{c^2} \begin{pmatrix} P_x^{NLO} \\ P_y^{NLO} \\ P_z^{NLO} \end{pmatrix}$$

.....(15)

In equation (15) the SHG source polarization $P^{NL} = P^{NLO} \exp[i(k_s \cdot r - 2\omega t)] \cdot \epsilon_s$ are defined in Fig. 1.

The homogeneous solution E_H in eq. (3) is determined by the Maxwell boundary conditions. For the geometry of Fig. 6 the boundary conditions can be written in the form

$$\begin{pmatrix} -\sin \phi & \cos \theta \cos \phi & -e_{2o\downarrow x} & -e_{2e\downarrow x} & -e_{2o\uparrow x} & -e_{2e\uparrow x} & 0 & 0 \\ \cos \phi & \cos \theta \sin \phi & -e_{2o\downarrow y} & -e_{2e\downarrow y} & -e_{2o\uparrow y} & -e_{2e\uparrow y} & 0 & 0 \\ \cos \theta \cos \phi & \sin \phi & -a_{2o\downarrow x} & -a_{2e\downarrow x} & -a_{2o\uparrow x} & -a_{2e\uparrow x} & 0 & 0 \\ \cos \theta \sin \phi & -\cos \phi & -a_{2o\downarrow y} & -a_{2e\downarrow y} & -a_{2o\uparrow y} & -a_{2e\uparrow y} & 0 & 0 \\ 0 & 0 & e_{2o\downarrow x} e^{i\alpha_{2o}} & e_{2e\downarrow x} e^{i\alpha_{2e}} & e_{2o\uparrow x} e^{-i\alpha_{2o}} & e_{2e\uparrow x} e^{-i\alpha_{2e}} & -e_{3o\downarrow x} e^{i\alpha_{3o}} & -e_{3e\downarrow x} e^{i\alpha_{3e}} \\ 0 & 0 & e_{2o\downarrow y} e^{i\alpha_{2o}} & e_{2e\downarrow y} e^{i\alpha_{2e}} & e_{2o\uparrow y} e^{-i\alpha_{2o}} & e_{2e\uparrow y} e^{-i\alpha_{2e}} & -e_{3o\downarrow y} e^{i\alpha_{3o}} & -e_{2e\downarrow y} e^{i\alpha_{3e}} \\ 0 & 0 & a_{2o\downarrow x} e^{i\alpha_{2o}} & a_{2e\downarrow x} e^{i\alpha_{2e}} & a_{2o\uparrow x} e^{-i\alpha_{2o}} & a_{2e\uparrow x} e^{-i\alpha_{2e}} & -a_{3o\downarrow x} e^{i\alpha_{3o}} & -a_{3e\downarrow x} e^{i\alpha_{3e}} \\ 0 & 0 & a_{2o\downarrow y} e^{i\alpha_{2o}} & a_{2e\downarrow y} e^{i\alpha_{2e}} & a_{2o\uparrow y} e^{-i\alpha_{2o}} & a_{2e\uparrow y} e^{-i\alpha_{2e}} & -a_{3o\downarrow y} e^{i\alpha_{3o}} & -a_{3e\downarrow y} e^{i\alpha_{3e}} \end{pmatrix} \begin{pmatrix} E_{rs0} \\ E_{rp0} \\ E_{2o\downarrow 0} \\ E_{2e\downarrow 0} \\ E_{2o\uparrow 0} \\ E_{2e\uparrow 0} \\ E_{3o\downarrow 0} \\ E_{3e\downarrow 0} \end{pmatrix}$$

$$= \begin{pmatrix} E_{IH0x} \\ E_{IH0y} \\ \frac{c}{2\omega}(k_{Sy}E_{IH0z} - k_{Sz}E_{IH0y}) \\ \frac{c}{2\omega}(k_{Sz}E_{IH0x} - k_{Sx}E_{IH0z}) \\ -e^{i\alpha_{IH}} E_{IH0x} \\ -e^{i\alpha_{IH}} E_{IH0y} \\ -\frac{c}{2\omega}(k_{Sy}E_{IH0z} - k_{Sz}E_{IH0y})e^{i\alpha_{IH}} \\ -\frac{c}{2\omega}(k_{Sz}E_{IH0x} - k_{Sx}E_{IH0z})e^{i\alpha_{IH}} \end{pmatrix} \dots\dots(16)$$

Where, E_{rio} ($i = s, p$) is the electric field amplitude of the reflected SHG light of i -polarization radiated into the first layer. It is defined by,

$$\mathbf{E}_{rs} = E_{rs0} \begin{pmatrix} -\sin \phi \\ \cos \phi \\ 0 \end{pmatrix} e^{i\frac{2\omega}{c}(\sin \theta \cos \phi x + \sin \theta \sin \phi y - \cos \theta z) - i2\omega t} \dots\dots(17)$$

$$\mathbf{E}_{rp} = E_{rp0} \begin{pmatrix} \cos \theta \cos \phi \\ \cos \theta \sin \phi \\ \sin \theta \end{pmatrix} e^{i\frac{2\omega}{c}(\sin \theta \cos \phi x + \sin \theta \sin \phi y - \cos \theta z) - i2\omega t} \dots\dots(18)$$

Where E_{rs} and E_{rp} are the electric fields of s- and p-polarized reflected second harmonic waves, respectively. E_{ijk} ($i = 2, 3; j = e, o; k = \downarrow, \uparrow$) is the second harmonic electric field in the i -th layer and is defined by

$$\mathbf{E}_{ijk} = E_{ijk0} \mathbf{e}_{ijk} e^{i\mathbf{k}_{ijk} \cdot \mathbf{r} - i2\omega t} \dots\dots(19)$$

The suffices e and o denote the extraordinary and ordinary electromagnetic waves respectively [2]. The suffices \downarrow and \uparrow denote the downward and upward propagating waves,

respectively. The vector e_{ijk} is the unit polarization vector of the electric field and can be written as,

$$e_{iok} = \frac{1}{\sqrt{\epsilon_{i\perp} - \sin^2 \theta \cos^2 \phi}} \begin{pmatrix} 0 \\ -\sqrt{\epsilon_{i\perp} - \sin^2 \theta} \\ \pm \sin \theta \sin \phi \end{pmatrix} \quad \dots\dots(20)$$

(+ and - signs for $k = \downarrow$ and \uparrow , respectively)

$$e_{iek} = \frac{1}{\sqrt{\epsilon_{i\parallel} + \left(\frac{\epsilon_{i\parallel}}{\epsilon_{i\perp}}\right) \sin^2 \theta \cos^2 \phi \left(\frac{\epsilon_{i\parallel}}{\epsilon_{i\perp}} - 1\right)}} \times \begin{pmatrix} \frac{\sqrt{\epsilon_{i\parallel} \left(1 - \frac{1}{\epsilon_{i\perp}} \sin^2 \theta \cos^2 \phi\right)}}{\epsilon_{i\parallel} \sin^2 \theta \cos \phi \sin \phi} \\ \frac{\epsilon_{i\perp} \sqrt{\epsilon_{i\parallel} \left(1 - \frac{1}{\epsilon_2} \sin^2 \theta \cos^2 \phi\right)}}{\mp \frac{\epsilon_1 \sin \theta \cos \phi}{\epsilon_2 \sqrt{\epsilon_1 \left(1 - \frac{1}{\epsilon_2} \sin^2 \theta \cos^2 \phi\right)}} \sqrt{\epsilon_1 - \sin^2 \theta \sin^2 \phi - \frac{\epsilon_1}{\epsilon_2} \sin^2 \theta \cos^2 \phi}} \end{pmatrix}$$

.....(21)

(- and + signs for $k = \downarrow$ and \uparrow , respectively)

and the k_{ijk} in equation (19) is defined by,

$$k_{iok} = \frac{\omega}{c} \begin{pmatrix} \sin \theta \cos \phi \\ \sin \theta \sin \phi \\ \pm \sqrt{\epsilon_{i\perp} - \sin^2 \theta} \end{pmatrix} \quad \dots\dots(22)$$

.....(23)

$$k_{iek} = \frac{\omega}{c} \left(\begin{array}{c} \sin \theta \cos \phi \\ \sin \theta \sin \phi \\ \pm \sqrt{\epsilon_{i//} - \sin^2 \theta \sin^2 \phi - \frac{\epsilon_{i//}}{\epsilon_{i\perp}} \sin^2 \theta \cos^2 \phi} \end{array} \right)$$

(+ and - signs for $k = \downarrow$ and \uparrow , respectively)

The matrix elements α_{ijkx} and α_{ijkz} in equation (16) are defined by,

$$a_{ijkx} = \frac{c}{2\omega} (k_{ijkz} e_{ijkz} - k_{ijkz} e_{ijkz}) \dots\dots(24)$$

$$a_{ijkz} = \frac{c}{2\omega} (k_{ijkx} e_{ijkx} - k_{ijkx} e_{ijkz}) \dots\dots(25)$$

α_{IH} and α_{ij} are defined by,

$$\begin{aligned} \alpha_{IH} &= k_{IHSz} d \\ \alpha_{2o} &= k_{2o\downarrow z} d = -k_{2o\uparrow z} d \\ \alpha_{3o} &= k_{3o\downarrow z} d = -k_{3o\uparrow z} d \quad \dots\dots(26) \\ \alpha_{2e} &= k_{2e\downarrow z} d = -k_{2e\uparrow z} d \\ \alpha_{3e} &= k_{3e\downarrow z} d = -k_{3e\uparrow z} d \end{aligned}$$

Where, d is the thickness of the second layer. The homogeneous solution E_H in equation (15) corresponds to E_{2jk} ($j = o, e; k = \downarrow, \uparrow$). θ and ϕ are the incidence angle and the azimuthal angle of the excitation beam, respectively. On the other hand, The SHG intensity from the surface electric dipole can be calculated from the equation (2). Here, the thickness d of the second layer should equal to one monolayer.

From equation (2) we have,

$$P_{S,i}^{(2)}(2\omega) = \sum_{ijk} \chi_{sijk}^{(2)} E_j E_k \dots(2)$$

Here, $\chi^{(2)}_{sijk}$ is the surface nonlinear susceptibility. It is defined by the following equation,

$$\chi^{(2)}_{sijk} = \frac{\chi^{(2)}_{ijk}}{\epsilon} d \quad \dots\dots(27)$$

Where, ϵ and d is the dielectric constant of the material and thickness of the second layer, respectively.

From equation (27) we can also calculate the $\chi^{(2)}_{ijk}$ elements. There are ten independent surface nonlinear susceptibility elements $\chi^{(2)}_{113}$, $\chi^{(2)}_{223}$, $\chi^{(2)}_{311}$, $\chi^{(2)}_{322}$, $\chi^{(2)}_{333}$, $\chi^{(2)}_{121}$, $\chi^{(2)}_{211}$, $\chi^{(2)}_{222}$, $\chi^{(2)}_{233}$, $\chi^{(2)}_{323}$ under the surface symmetry Cs of TiO₂(320). The numbers 1, 2, and 3 represent the [001], $[\bar{2}30]$, and [320] directions on the TiO₂ (320) surface, respectively.

In order to determine which element of the susceptibility $\chi^{(2)}_{ijk}$ is dominant for Au/TiO₂(320) and bare TiO₂(320), we must compare the SHG intensity patterns obtained from the experiments with those obtained by the calculation by using least square fitting algorithm. We calculated the SHG intensity patterns for all the independent nonlinear susceptibility elements. For calculating the SHG intensity patterns for nonlinear susceptibility elements, we also calculated the internal electric field strength and nonlinear polarization in the surface layer using Maxwell's equations under the appropriate boundary conditions which is shown above. The calculated SHG intensity patterns of ten independent nonlinear susceptibility elements for both Au/TiO₂(320) and bare TiO₂(320) sample at wavelength of 532 nm that are shown in the following table 1.

532 nm	Au/TiO ₂ (320)				Bare TiO ₂ (320)			
$\chi_{ijk}^{(2)}$	Pin/Pout	Pin/Sout	Sin/Pout	Sin/Sout	Pin/Pout	Pin/Sout	Sin/Pout	Sin/Sout
113	 4.40	 0.67			 39.00	 6.00	 0.0015	 0.0018
223	 4.40	 0.80			 20.00	 3.40	 0.0011	 0.0012
311	 4.40	 0.02	 6.80	 0.013	 10.00	 0.016	 5.00	 0.009
322	 14.00	 0.026	 12.00	 0.018	 11.00	 0.022	 10.00	 0.016
333	 3.20	 0.012			 62.50	 0.21		
112	 0.023	 0.016	 0.015	 0.01	 0.90	 0.60	 0.58	 0.38
211	 0.035	 0.17	 0.13	 0.014	 1.10	 5.15	 4.20	 0.41
222	 0.35	 0.035	 0.032	 0.17	 12.50	 1.20	 1.25	 6.00
233	 0.69	 0.58			 3.40	 2.90		
323	 10.50	 0.032	 0.0016		 13.50	 0.04	 0.002	

Table 1. The calculated SHG intensity patterns of ten independent nonlinear susceptibility elements for both Au/TiO₂ (320) and bare TiO₂ (320) sample at wavelength of 532 nm.

After decomposing the ten independent optical nonlinear susceptibility elements $\chi_{ijk}^{(2)}$ theoretically and then I divide them into Au/TiO₂ (step), Au/TiO₂ (terrace), bare TiO₂ (step) and bare TiO₂ (terrace) group at wavelength 532 nm but we consider only terrace group analysis for the experimental results obtained from the applied wavelength of 1064 nm shown in table 3 and 2, respectively. Here, i, j and k denote the axis direction. We have two anisotropic direction. The mirror plane of the surface structure is the 2-3 plane. In a more specific way, direction 2 is parallel to surface that lies in the mirror plane of TiO₂ and

perpendicular to step edge where the symmetry is broken and direction 3 is perpendicular to the surface of the stepped TiO₂ sample shown in Fig. 2. The azimuthal angle ϕ is the angle between X and the axis 1. The angle ϕ equals to zero when X and the axis 1 are on the same direction as illustrated above. At $\phi = 0^\circ$, direction 2 corresponds to the step up direction and it is same direction with laboratory coordinate Y.

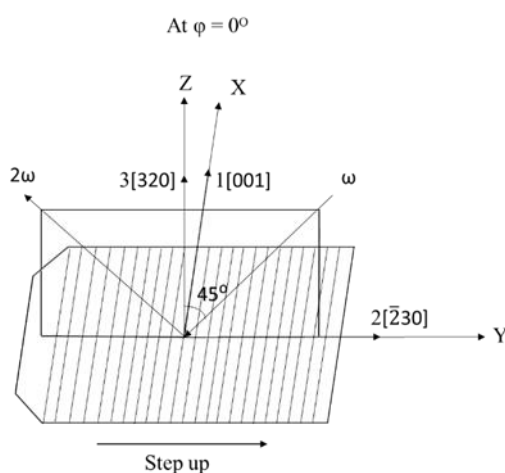


Figure 2. Schematic diagram of the stepped TiO₂ (320) substrate with the incidence plane. Here the coordinate symbols are (X,Y,Z)=Laboratory Coordinates and (1,2,3)≡Sample Coordinate.

The sample coordinates are indicated by 1[001], 2[$\bar{2}$ 30] and 3[320] directions.

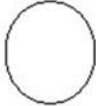
Sample	$\chi_{ijk}^{(2)}$	Pin - Pout	Pin - Sout	Sin - Pout	Sin - Sout
Au/TiO ₂ (320) (1064 nm)	Au/TiO ₂ terrace contribution	 17		 3.4	
Bare TiO ₂ (320) (1064 nm)	Bare TiO ₂ terrace contribution	 2.35		 0.62	

Table 2. The calculated SHG intensity patterns for both Au/TiO₂ (320) and bare TiO₂ (320)

based on the terrace contribution with photon excitation energies of 1.17 eV. The SHG intensity is plotted in the radial direction in an arbitrary but common unit.

Sample	$\chi_{ijk}^{(2)}$	Pin - Pout	Pin - Sout	Sin - Pout	Sin - Sout
Au/TiO ₂ (320) (532 nm)	Au/TiO ₂ terrace contribution	 33		 12.5	
	Au/TiO ₂ step contribution	 10		 0.2	
Bare TiO ₂ (320) (532 nm)	TiO ₂ terrace contribution	 24	 0.5	 1	
	TiO ₂ step contribution	 0.6	 0.5	 0.6	 0.5

Table 3. The calculated SHG intensity patterns for Au/TiO₂ (320) and bare TiO₂ (320) based from the terrace and step contributions fitted to the experimental results with photon excitation energies of 2.33 eV. The SHG intensity is plotted in the radial direction in an arbitrary but common unit.

Table 1, 2 and 3 show the calculated SHG patterns and peak intensities from the model dielectric structure shown in Fig.1 for TiO₂ (320) face, when one of the ten surface nonlinear susceptibility elements $\chi_{Sijk}^{(2)(320)}$ is set equal to a common value and the other elements are set equal to zero. Here, $\chi_{Sijk}^{(2)(320)}$ is defined as the surface nonlinear susceptibility

for the (320) index. We used dielectric constant of TiO₂, $\epsilon_{//}$ (2.33eV) = 8.821 and $\epsilon_{//}$ (4.66eV) = -7.409 + i13.24 for the electric fields parallel to the (001) crystal axis, and ϵ_{\perp} (2.33eV) = 7.129 and ϵ_{\perp} (4.66eV) = 3.165 + i8.15 for the electric fields perpendicular to the (001) axis [3]. The patterns were calculated for all four combinations of the p- and s-polarized incidence and output. Table-1, 2 and 3 show the calculated SHG intensity patterns and peak intensities from the model dielectric structure. In this case, for the measurement of each $\chi_{Sijk}^{(2)(320)}$ element is set equal to 1 and the other elements are set equal to zero.

By this way the fitting was done of our experimental values shown in Figs. 4.2.1.2, 4.2.1.3, 4.2.1.4 and 4.2.1.5 for both Au/TiO₂ (320) and bare TiO₂ (320) at wavelength of 1064 nm and 532 nm. We calculated the linear combinations of the patterns in table 1, 2 and 3 in the complex plane with each pattern multiplied by the relevant nonlinear susceptibility element $\chi_{Sijk}^{(2)(320)}$ and then vary the nonlinear susceptibility elements as adjustable parameters. Generally, in fortunate cases, we can determine the nonlinear susceptibility elements from the best fit results of this fitting. However, since there are susceptibility elements giving similar patterns as seen in tables 1, 2 and 3, we cannot determine the unique set of susceptibility elements. There is a considerable amount of arbitrariness in the determination of the set of the nonlinear susceptibility elements for TiO₂ (320) face.

So I divided all the ten independent susceptibility elements into two groups to observe their step and terrace contributions from the calculated SHG intensity patterns. Each group consists of five $\chi_{Sijk}^{(2)(320)}$ elements. In case of our sample, direction 2 is the anisotropic direction which is parallel to the surface that lies in the mirror plane of TiO₂(320) and perpendicular to the step edge. So considering the content of odd number of 2, the nonlinear susceptibility elements such as $\chi_{121}^{(2)}$, $\chi_{211}^{(2)}$, $\chi_{222}^{(2)}$, $\chi_{233}^{(2)}$, $\chi_{323}^{(2)}$ elements are kept in the same group showing step contributions. The other five susceptibility such as $\chi_{113}^{(2)}$, $\chi_{223}^{(2)}$, $\chi_{311}^{(2)}$, $\chi_{322}^{(2)}$, $\chi_{333}^{(2)}$ elements are kept in another group having terrace contributions. Indeed, the anisotropic response was observed due to having contributions of these two groups of nonlinear susceptibility elements. Table 2 and 3 are showing the SHG intensity patterns provided by the two groups of $\chi_{Sijk}^{(2)(320)}$ elements for both Au/TiO₂ (320) and bare TiO₂ (320) at wavelength of 532 nm and 1064 nm.

References:

1. K. Kumagai, G. Mizutani, H. Tsukioka, T. Yamauchi and S. Ushioda; Phys. Rev. B 48 (1993) 14488.
2. M. Born and E. Wolf; Principles of Optics (Pergamon Press, New York, 1974).
3. M. W. Ribarsky; Hand Book of Optical Costants of Solids ed E D Palik (San Diego, CA: Academic) p. 795, 1985.

Appendix - III**Report on how to irradiate the incident laser beam on to the center of a sample.**

Step-1:

At first, I will attach a piece of graph paper on the sample holder using tape. The shape and size of the graph paper will be similar with the sample holder. So that I can mark the points on it perfectly for each 90° rotation. For the beam height estimation, I will measure the height from the experimental table surface to the center of the monocromator slit vertically by using meter scale. After that, I will irradiate the laser beam on the sample holder and also will check the beam height in the same way. But the height of the beam should be same. This is a rough estimation. I will irradiate the laser beam on the sample holder for each 90° rotation like 0° , 90° , 180° and 270° . I will mark the four points and diagonally connect them to find the suitable center position [Fig.1.]. The purpose of finding the center position is to irradiate the laser beam at the same point. Because the rotation axis will pass through the same point for each rotation. But the path direction will be little deviated from each other due to having tilt on the sample holder [Fig.2.]. Then I will rotate the rotation stage to the little left side because I intend to irradiate the reflected beam on a white board when I will attach the sample at the estimated center point on the sample holder. The white board placed far away from the sample near the UHV chamber in the first floor picosecond laser room. Now I will irradiate the laser beam to the diagonally connected center on the sample holder.

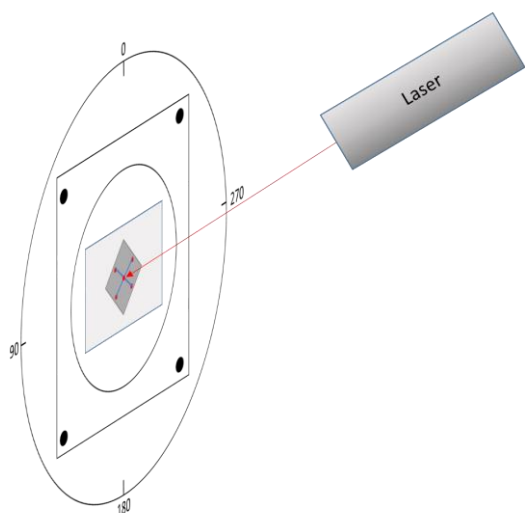


Figure 1. Finding the center on the sample holder by irradiating incident laser beam.

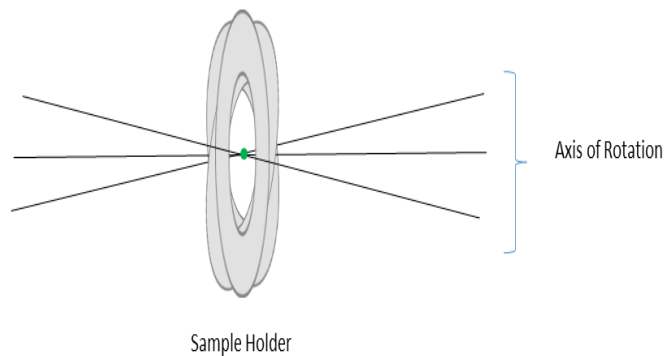


Figure 2. Rotation axis pass through the same point although the sample holder is tilted either side.

Step-2:

In this step, at first I will stack the sample on the center by using double sided tape which is obtained in the first step. The main purpose of this step is to find the axis of rotation. Now the question is what is axis of rotation? The axis of rotation is the straight line through all fixed points of a rotating rigid body around which all other points of the body move in circles. That means this line always pass through the center of the body along with the normal. This line must create 90° angle with respect to the surface plane [Fig.3]. For finding the rotation axis, I will set a white board far away from the sample which is located near the UHV chamber in the 1st floor picosecond laser room. Then I will attach a graph paper on the

board by tape. Then I will irradiate the laser beam on the sample surface again. The beam will be reflected from the sample surface and will reach on to the graph paper. Then I will rotate the sample holder each 90° and will get four points on the graph paper. Then I will connect them diagonally and find the center. In this case, may be the reflected light will be weak. So, I can increase the laser power but it should be little. In case of GaAs sample I can increase the laser power up to $\sim 30 \mu\text{J}/\text{pulse}$. Because the high laser power may damage the sample surface. When the diameter of the reflected beam is too large, then I will use iris in between the sample and the white board to reduce the beam diameter. I will allow the reflected beam to pass through the center of the iris and by using adjustable knob I can control the beam diameter. Which will help me to mark the points of the reflected beam accurately on the graph paper attached on the white board. Fig.4. shows the sample holder is tilted either side. That's why I will get four points on the white board for each 90° rotation. So the rotation axis will be different for having tilt of the sample holder. In this case, the rotation axis direction will be changed for each 90° rotation due to the change of the position of reflected beam on the board which is clearly shown in Fig.5.

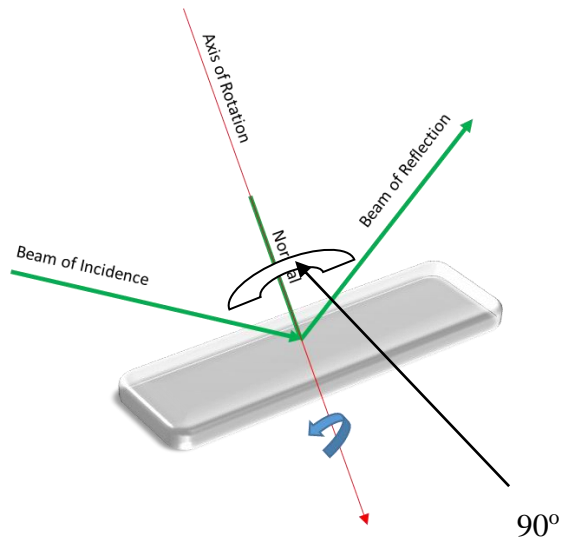


Figure 3. Rotation of axis.

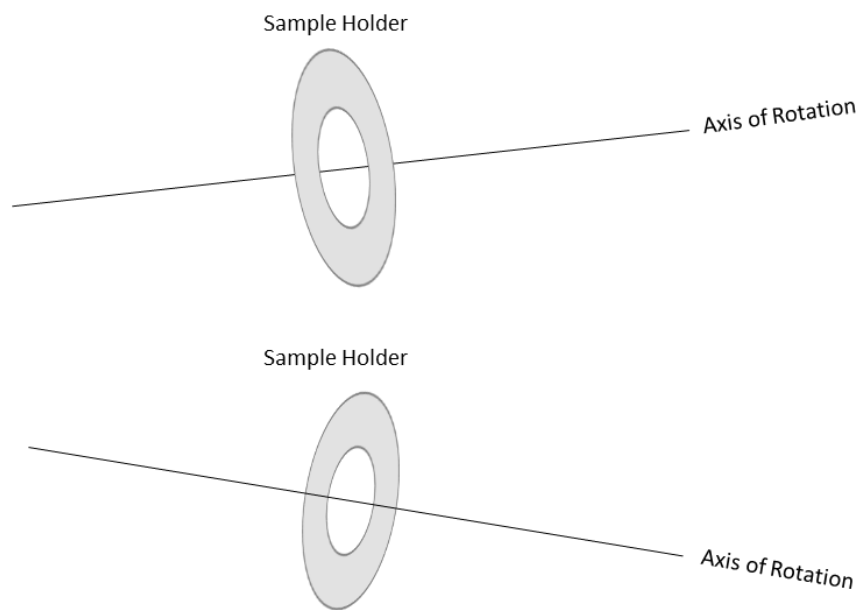


Figure 4. Position of rotation axis which is changing with tilt direction.

After getting the center, I will irradiate the reflected beam just on the center by using tilt adjustable knob. But in this case, I need the help of Tomatsu San or any other lab members. Because I will adjust the tilt and he will watch the position of the reflected beam on the graph paper attached on the white board and let me know continuously about the position of the reflected beam for irradiating just on the exact position (center). If the beam exist on the same center for each 90° rotation then hopefully the rotation axis will be same for each rotation [Fig.5.]. So, step-2 is remarkably important to find the exact rotation axis.

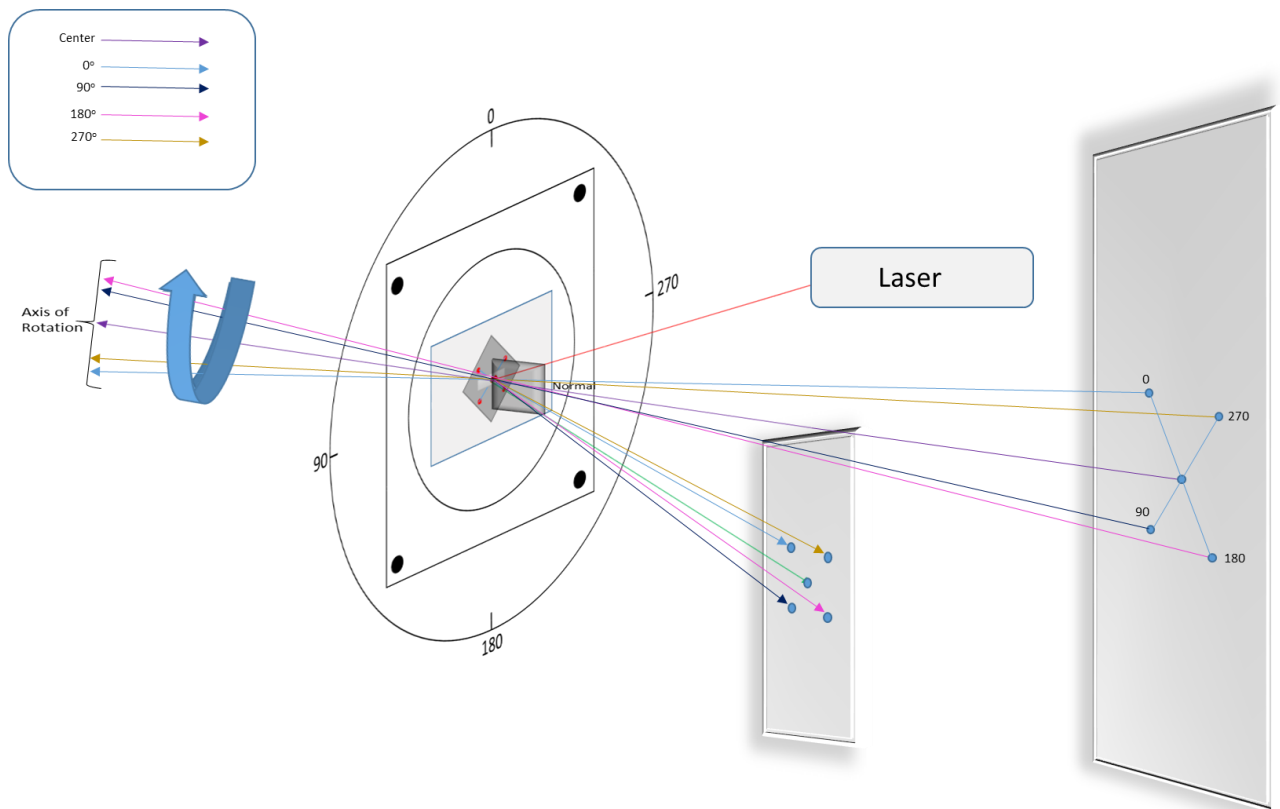


Figure 5. Rotation of axis for each 90° rotation of the sample and also the rotation of axis for the center which is exactly lies on the normal of place of incidence.

Step-3:

In this step, I want to irradiate the reflected beam into the monochromator slit. But it is important to remember that, the incident beam should irradiate the center point which is obtained in the first step. For this reason, I will attach a small size graph paper just like the shape of sample holder surface on the sample by tape which is easily removable. Then mark the position of incident beam on the graph paper actually this position is the center that I obtained in the first step and make a pinhole on that position of the graph paper. After that, the rotation stage will be moved back to the previously marked position (which is done in the step-1). Now I will irradiate the laser beam at the pinhole point and also I will identify the position of the reflected beam [Fig.6.]. In some cases, the reflected beam is unable to irradiate the center of the monochromator slit. Because the rotation stage along with the sample holder may not be exactly parallel with the vertical plane. So the reflected beam position may be changed from the center of the monochromator slit. I must correct this one, so I will insert one or two paper under the magnet as shown in Fig.7 to make the rotation stage parallel to the vertical plane. Now the incident and reflected beam height will be same and the reflected beam will correctly reach to the monochromator slit. Then I will rotate the sample each 10° to check the reflected beam position. This process will take long time for tuning the laser beam and to find the exact rotation axis. So, it is possible to conduct the angle dependent SHG experiments almost accurately.

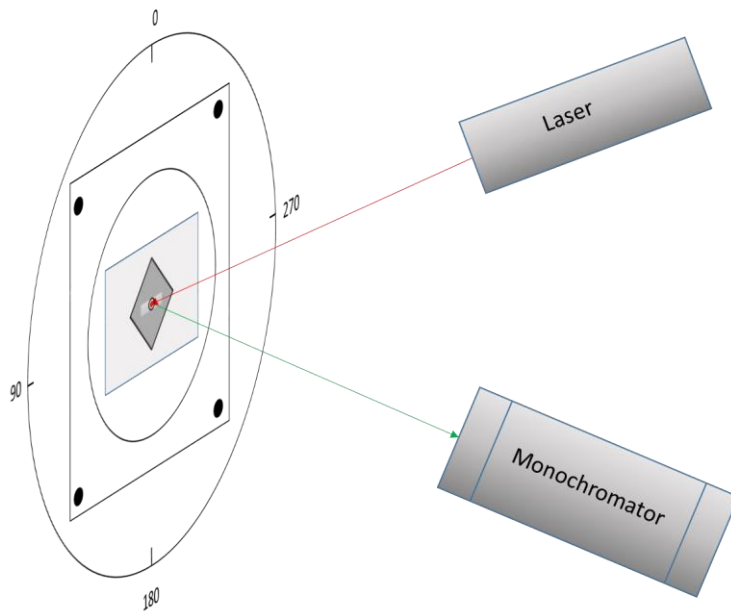


Figure 6. Reflected beam is irradiating on to the slit of monochromator.

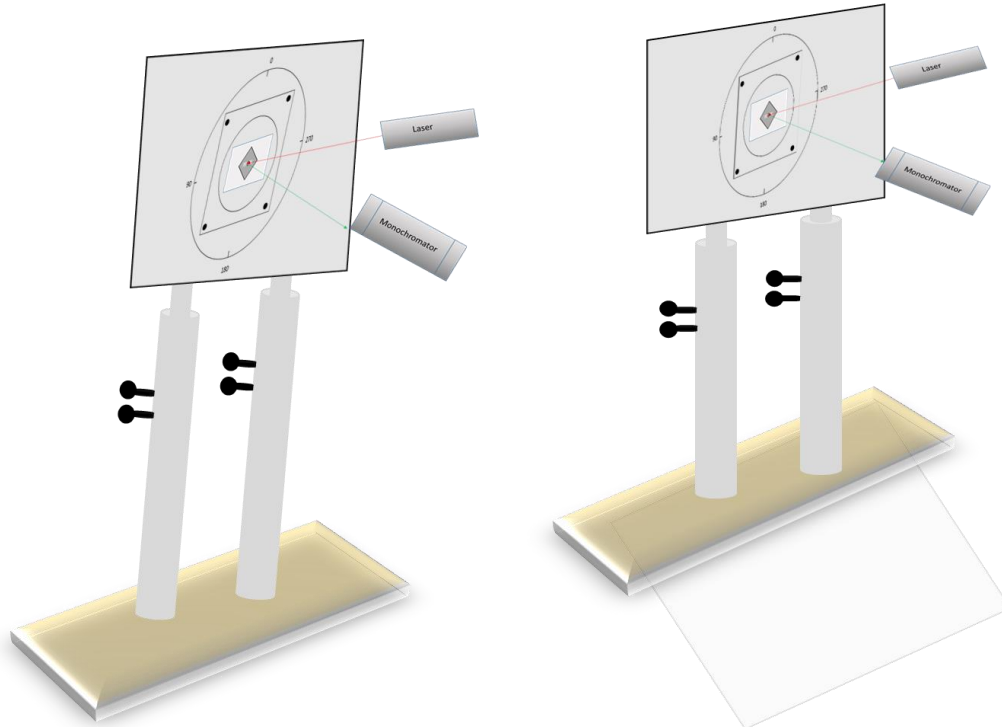


Figure 7. Correction of the reflected beam height by inserting paper under the magnet.

Appendix - IV

Report on Observation of Monochromator Sensitivity Based on Horizontal and Vertical Polarizations

Due to calibration our experimental data of wavelength 532 nm, we checked the monochromator sensitivity in terms of SHG intensity and both horizontal and vertical output polarization. For this purpose, we kept our experimental setup according to the following Fig.

1.

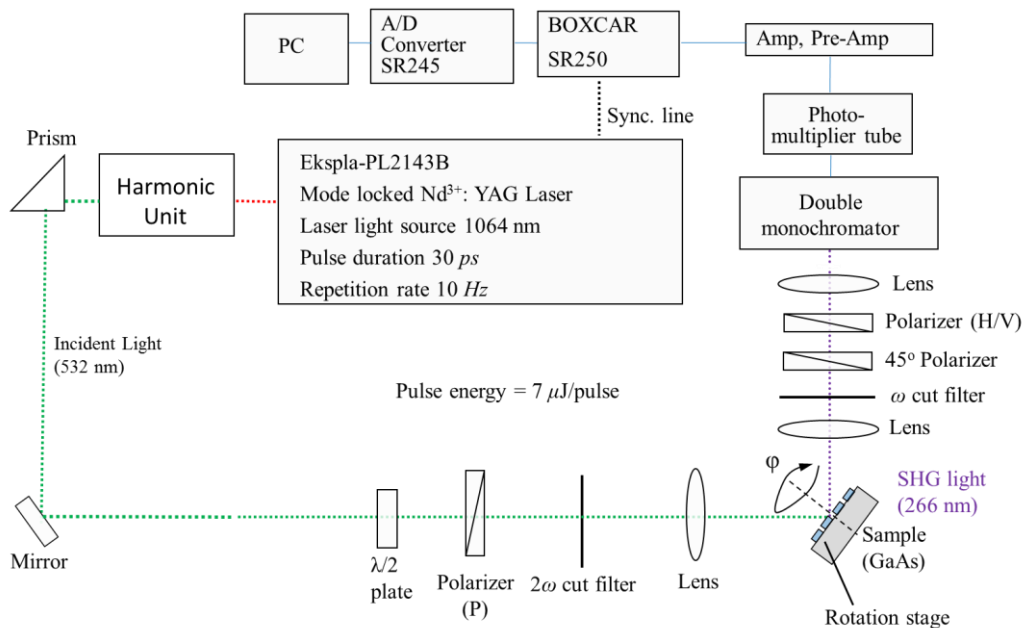


Figure 1. Optical setup for monochromator sensitivity check.

Fig. 1. shows that the incident light of wavelength 532 nm was irradiated on the GaAs (100) sample. The reflected light was passed through lens, ω -cut filter, 45° polarizer, horizontal or vertical polarizer to obtain the SHG signal due to compare the SHG intensity

difference for horizontal and vertical output polarization in order to check the sensitivity of monochromator.

Fig. 2. Exhibits the normalized SHG intensity in terms of horizontal and vertical polarization of GaAs (100) sample. In case of horizontal polarization, the SHG intensity is little lower compared to the SHG intensity of vertical polarization. The normalized sensitivity ratio of horizontal and vertical polarization is 0.855 : 1. Therefore, the monochromator is more sensitive to the vertical polarization.

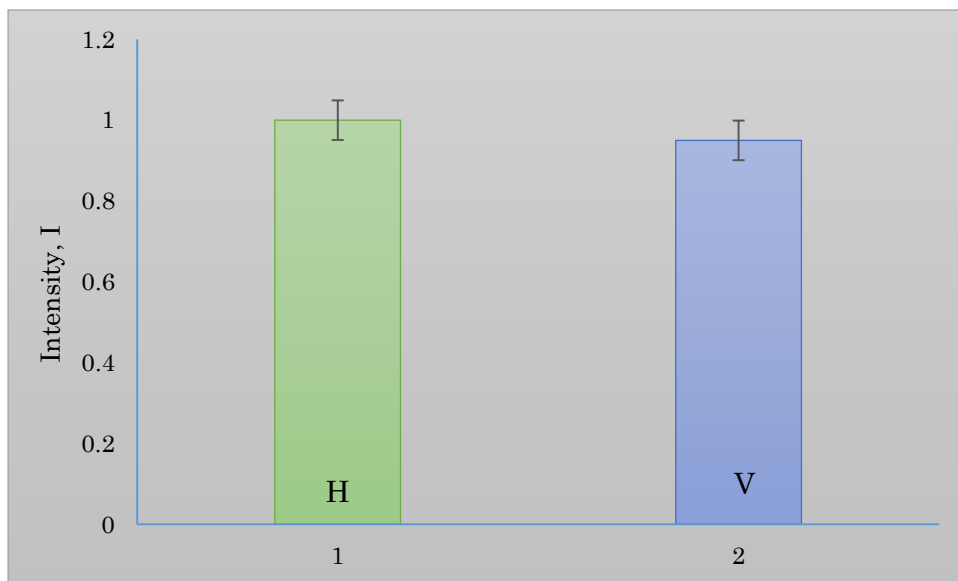


Figure 2. Bar chart showing the normalized value of sensitivity of monochromator in terms of SHG Intensity of GaAs (100) sample. (1) Horizontal (2) Vertical sensitivity.

Calculations for calibrating SHG intensity for Pout and Sout of both Au deposited TiO₂ (320) and bare TiO₂ (320) with respect to the horizontal and vertical SHG intensity of GaAs (100):

According to the normalized value of the horizontal and vertical sensitivity for GaAs (100) sample, we calculate the Pout and Sout value for both Au deposited TiO₂ (320) and bare TiO₂ (320) sample. In case of calibrating the P-out data of both sample, the SHG intensity value of both sample for 0° to 360° is divided by 0.855. Because the normalized horizontal sensitivity of monochromator is 0.855 for GaAs (100) sample. Similarly, In case of calibrating the S-out data of both sample, the SHG intensity value for 0° to 360° is divided by 1. Because the normalized vertical sensitivity of monochromator is 1 for GaAs (100) sample. After that we plot all the P-out and S-out sensitivity curve for both the sample at wavelength 532 nm. In this report we only show the calibration calculation and bar chart from both Au deposited TiO₂ (320) and bare TiO₂ (320) sample at 0° position.

The bar charts for Pout and Sout from the Au deposited TiO₂ sample in terms of SHG Intensity at 0° position are shown in the following Figs. 3 and 4.

For Pout and Sout of Au deposited TiO₂ (320),

<u>SHG Intensity at 0° position for Au deposited TiO₂ (320) (Pout)</u>	=	<u>17.97664</u>
SHG intensity at 0° position for GaAs (100) (Horizontal)	=	0.855
	=	21.025
..... up to 360°		
<u>SHG Intensity at 0° position for Au deposited TiO₂ (320) (Sout)</u>	=	<u>0.305667</u>
SHG intensity at 0° position for GaAs (100) (Vertical)	=	1
	=	0.305667
..... up to 360°		

For Pout and Sout of bare TiO₂ (320),

<u>SHG Intensity at 0° position for bare TiO₂ (320) (Pout)</u>	=	<u>35.786</u>
SHG intensity at 0° position for GaAs (100) (Horizontal)	=	0.855
	=	41.8549
..... up to 360°		
<u>SHG Intensity at 0° position for bare TiO₂ (320) (Sout)</u>	=	<u>0.564333</u>
SHG intensity at 0° position for GaAs (100) (Vertical)	=	1
	=	0.564333
..... up to 360°		

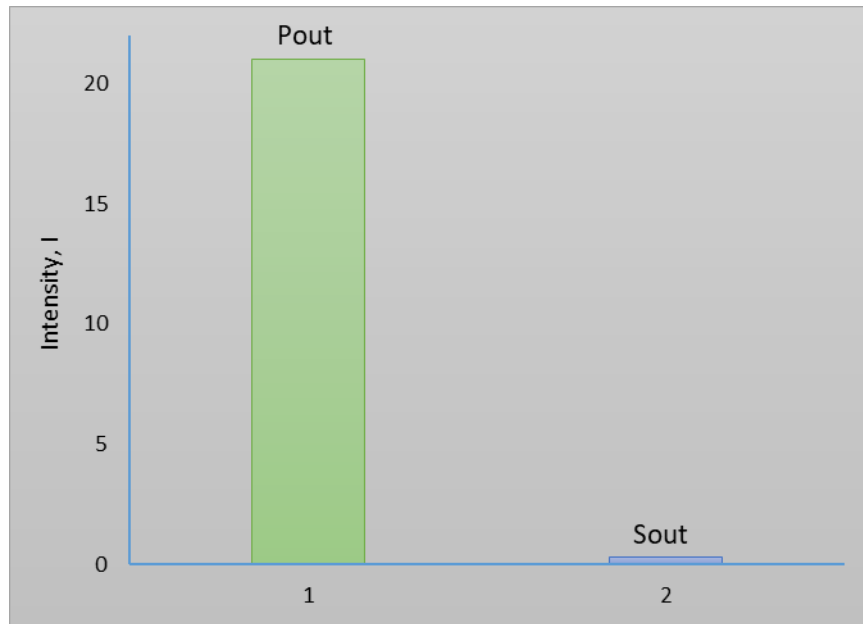


Figure 3. Bar chart showing the Pout and Sout from the Au deposited TiO₂ sample in terms of SHG Intensity at 0° position.

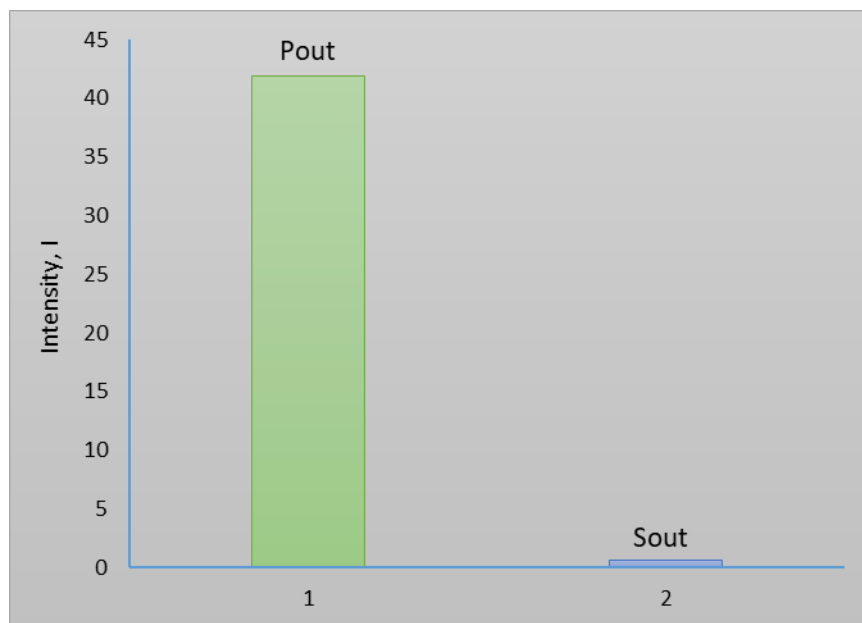
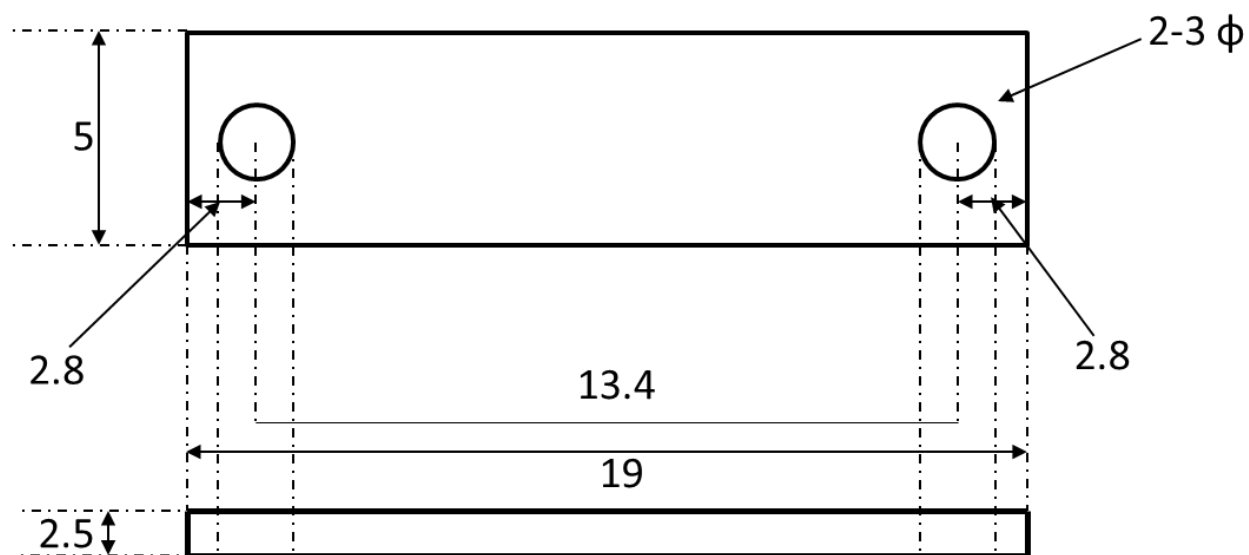


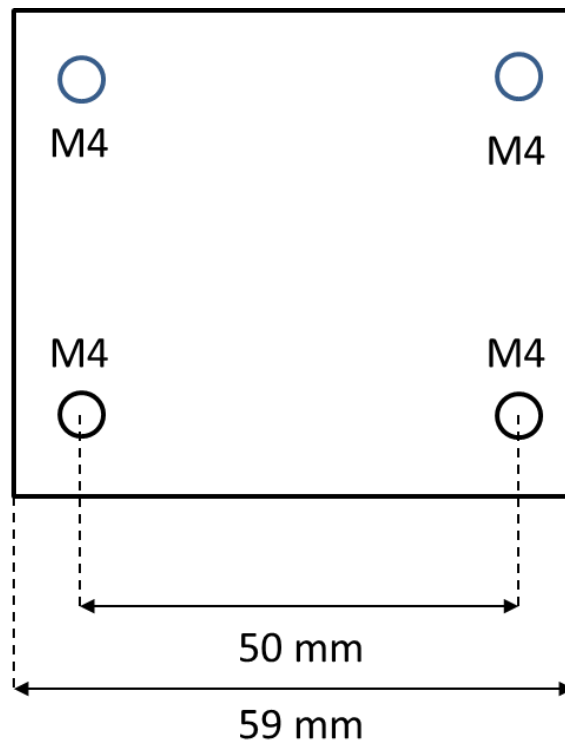
Figure 4. Bar chart showing the Pout and Sout from the bare TiO₂ sample in terms of SHG Intensity at 0° position.

Appendix – V

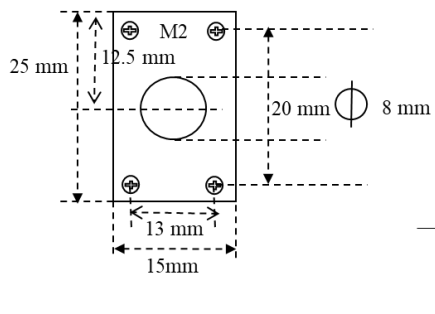
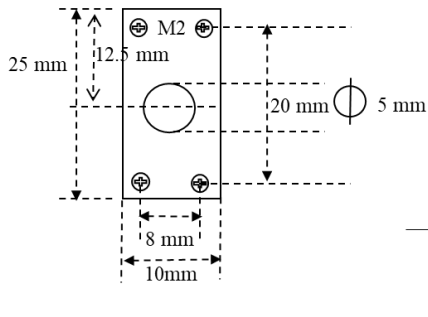
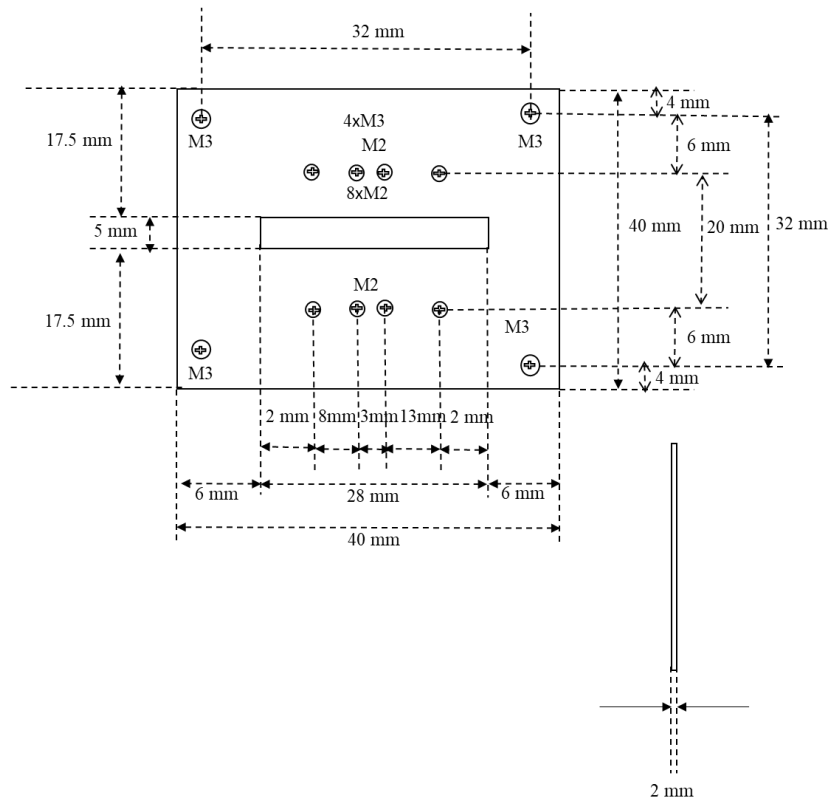
Drawing of some necessary experimental parts that I used during my experiments including the fabrication of Au thin film on the TiO₂ (320) single crystal and SHG measurements.



Name: Haque Mohammad Ehasanul
Student ID: 1540014
Sample: Spacer of sample holder
Quantity: 1
Material: Steel

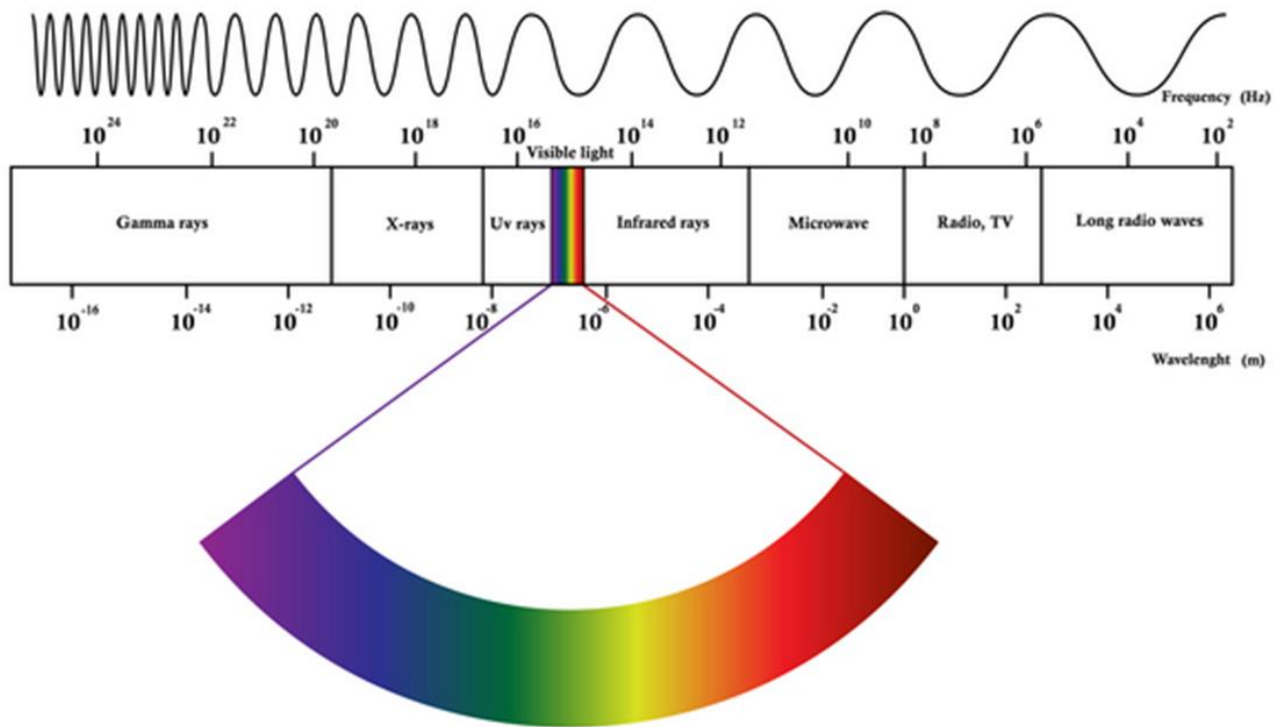


Name: Haque Mohammad Ehasanul
Student ID: 1540014
Sample: Sample holder
Quantity: 1
Material: Aluminum Sheet



Name: Haque Mohammad Ehasanul
 Student ID: 1540014
 Sample: Sample holder
 Quantity: 1
 Material: Aluminum Sheet

Different types of electromagnetic radiation and their range of wavelength in meter (m) and frequency in Hertz (Hz).



Appendix - VI

List of Publications and conference participation

Publication in Journal

1. **Md Ehasanul Haque**, Daiki Kobayshi, Yuki Tomatsu, Khuat Thi Thu Hien, Goro Mizutani, Mohammad Mizanur Rahman and Harvey N. Rutt; “Optical second harmonic generation analysis of the atomically stepped Au/TiO₂ (320) interface” *AIP Advances* 7, 125011 (2017).

Proceedings publication in conferences

1. **Md Ehasanul Haque**, Daiki Kobayshi, Yuki Tomatsu, Khuat Thi Thu Hien, Goro Mizutani and Harvey N. Rutt; “Observation of Second Harmonic Generation of the Stepped Au/TiO₂ (320) Interface” *11th International Symposium on Atomic Level Characterizations for New Materials and Devices '17*; Aqua Kauai Beach Resort, Kauai, Hawaii, USA, December 3 (Sun) – 8 (Fri), 2017.
2. Yuki Tomatsu, **Md Ehasanul Haque**, Khuat Thi Thu Hien, Goro Mizutani, and Harvey N. Rutt; A Study of Optical Second Harmonic Investigation of the Au/TiO₂ (320) interface; *Optical Properties of Solid in 2016*; Kobe University, Kobe, Japan, 2-3 December, 2016.

Attended conferences/Symposium

1. **Md Ehasanul Haque**, Daiki Kobayshi, Yuki Tomatsu, Khuat Thi Thu Hien, Goro Mizutani and Harvey N. Rutt; “Surface Second Harmonic Generation (SHG) on the Au/TiO₂ (320) Interface and Bare TiO₂ (320)” *The 6th International Symposium on Organic and Inorganic Electronic Materials and Related Nanotechnologies (EM-NANO 2017)*; AOSSA Fukui, Japan, June 18-21, 2017.
2. **Md Ehasanul Haque**, Daiki Kobayshi, Yuki Tomatsu, Khuat Thi Thu Hien, Goro Mizutani and Harvey N. Rutt; “Measurement of the Electronic States from Au/TiO₂ (320) Interface Using Optical Second Harmonic Generation” *Annual Meeting of the Physical Society of Japan in 2017*; Osaka University, Osaka, Japan, 17-20 March, 2017.
3. **Md Ehasanul Haque**, Daiki Kobayshi, Yuki Tomatsu, Khuat Thi Thu Hien, Goro Mizutani and Harvey N. Rutt; “The Au/TiO₂ (320) interface study by using optical second harmonic generation technique” *Japan-India Symposium in 2017*; JAIST, Ishikawa, Japan, 6-7 March, 2017.
4. **Md Ehasanul Haque**, Daiki Kobayshi, Yuki Tomatsu, Khuat Thi Thu Hien, Goro Mizutani and Harvey N. Rutt; “Observation of the electronic states from Au/TiO₂ (320) interface as a function of the azimuthal angle and polarization by optical second harmonic generation” *Symposium on Surface Science and Nanotechnology in 2017*; Kyoto, Japan, 24-25 January, 2017.
5. **Md Ehasanul Haque**, Daiki Kobayshi, Yuki Tomatsu, Khuat Thi Thu Hien, Goro Mizutani and Harvey N. Rutt; “Investigation of the Au/TiO₂ (320) Interface by Optical Second Harmonic Generation Technique” *MRS Fall Meeting & Exhibitions in 2016*,

Boston, Massachusetts, USA, 27 November – 2 December 2016.

6. **Md Ehasanul Haque**, Daiki Kobayshi, Yuki Tomatsu, Khuat Thi Thu Hien, Goro Mizutani and Harvey N. Rutt; “Optical Second Harmonic Investigation of the Au/TiO₂ (320) Interface” *Autumn Meeting of the Physical Society of Japan in 2016; Kanazawa University, Ishikawa, Japan, 13-16 September, 2016.*
7. Yuki Tomatsu, **Md Ehasanul Haque**, Khuat Thi Thu Hien, Goro Mizutani and Harvey N. Rutt; “A Study of Optical Second Harmonic Investigation of the Au/TiO₂(320) interface” *Organic and Inorganic Electronics Symposium : O & I Symposium, Kanazawa University, Ishikawa, Japan, 15-16 July, 2015.*
8. Peiyang Gong, **Md Ehasanul Haque**, Khuat Thi Thu Hien and Goro Mizutani; “Electronic states of the Au/TiO₂ photocatalyst interface by tunable SHG spectroscopy” *Annual Meeting of the Physical Society of Japan in 2018; Tokyo University of Science, Tokyo, Japan, 22-25 March, 2018.*
9. **Md. Ehasanul Haque**, Peiyang Gong, Daiki Kobayshi, Yuki Tomatsu, Khuat Thi Thu Hien, Goro Mizutani and Harvey N. Rutt; “Study of electronic states of Au/Stepped TiO₂ (320) interface by SHG as a function of azimuthal angle, polarization and wavelength” *JAIST World Conference 2018; Ishikawa Hitech Center, Nomi, Ishikawa, Japan, 27-28 February, 2018.*
10. **Md. Ehasanul Haque**, Peiyang Gong, Daiki Kobayshi, Yuki Tomatsu, Khuat Thi Thu Hien, Goro Mizutani and Harvey N. Rutt; “Analysis of SHG signal from the interface of TiO₂ (320) decorated by Au thin film as a function of azimuthal angle and wavelength.” *JAIST Japan India Symposium 2018; JAIST, Nomi, Ishikawa, Japan, 5-6 March, 2018.*